TU
VIENNA

Dissertation

Characterization of contaminations on semiconductor surfaces and thin layer systems with Time of Flight - Secondary Ion Mass Spectrometry

ausgeführt zum Zwecke der Erlangung des akademischen Grades eines Doktors der technischen Wissenschaften unter der Leitung von

Univ. Prof. Herbert Hutter

am Institut für chemische Technologien und Analytik AC164

eingereicht an der Technischen Universität Wien
Fakultät für Technischen Physik
von

Dipl.-Ing. Stefan Puchner
Matr.Nr. 0026808
Vorgartenstraße 221/6/35
A-1020 Wien

Wien, im Jänner 2011

_____
Stefan Puchner

"I am among those who think that science has great beauty.

A scientist in his laboratory is not only a technician:

he is also a child placed before natural phenomena which impress him like a fairy tale."

(Marie Curie)

to Martha

KAI Kompetenzzentrum Automobil-
und Industrie-Elektronik GmbH
Europastrasse 8
9524 Villach/ Austria
http:\\www.k-ai.at

Danksagung

Abstract

Controlled surface characteristics are crucial for optimal product performance and device reliability, especially on bond pads: Various contaminations (organic and inorganic) might take influence on bond wire adhesion and reliability behavior. Hence, contamination monitoring − next to failure analysis − is essential to eliminate failures during manufacturing, to determine causes of failure respectively.

Within this work different analytical techniques: Rutherford Backscattering (RBS), Elastic Recoil Detection (ERD), Electron microscopy (SEM), Auger Electron Spectroscopy (AES), Atomic Force Microscopy (AFM), Digital Holography Microscopy, Gas Chromatography− Mass Spectrometry (GC−MS) and Laser Doppler Vibrometry were used to support Time of Flight Secondary Ion Mass Spectrometry (ToF−SIMS) investigations in semiconductor research areas.

The aim of this thesis was to identify contaminations in semiconductor industry and characterize their role on device reliability by means of process splits cooperating with Infineon Technologies Austria in Villach.

One focus was on bond pad contamination, which have been identified and allocated to their sources, another focus on contaminations in thin layer systems. Wafer split experiments were designed to investigate the impact of different contaminations owing to transport, environment or manufacturing steps on sample formation and device reliability: The effect of manufacturing process steps during the back end of line (BEOL) processing on the hydrogen concentration within the gate oxide (GOX) was determinded and the impact of breeded titanium contamination on the wire bond reliability was demonstrated.

Kurzfassung

Kontrollierte Oberflächeneigenschaften sind entscheidend für eine optimale Produktleistung und die Produktzuverlässigkeit, insbesondere auf Bondpads: Verschiedene Verunreinigungen (organisch und anorganisch) können Einfluss auf Bonddraht Haftung und Lebensdauer nehmen. Daher ist eine kontrollierte Probenoberfläche unbedingt notwendig um Fehler während der Herstellung zu vermeiden und um gegebenenfalls Fehlerursachen ermitteln zu können.

Innerhalb dieser Arbeit wurden verschiedene analytische Techniken:

Rutherford− Rückstreu− Spektrometrie (RBS), Elastic Recoil Detection (ERD), Rasterelektronenmikroskopie (REM), Auger− Elektronenspektroskopie (AES), Rasterkraftmikroskopie (AFM), Gaschromatographie− Massenspektrometrie (GC−MS), Laser Doppler Vibrometrie, Sheartests und Flugzeitsekundärionenspektrometrie (ToF−SIMS) verwendet um Kontaminationen in der Halbleiterindustrie zu überwachen und zu charakterisieren.

Das Ziel dieser Arbeit war es, Verunreinigungen zu identifizieren, ihre Ursachen zu erforschen und ihren Einfluss auf die Produktzuverlässigkeit zu untersuchen.

Ein Schwerpunkt lag auf Bondpad Kontamination (d.h. hauptsächlich Oberflächen− kontaminationen), ein weiterer Schwerpunkt auf Verunreinigungen in dünnen Schichten.

Wafersplit−Experimente wurden entwickelt, um die Auswirkungen der durch Umwelt− bzw. Fertigungsschritte hervorgerufenen Verunreinigungen auf folgende Montageprozesse und die Produktlebensdauer zu untersuchen: Die Auswirkung unterschiedlicher Herstellungsschritte während der BEOL Verarbeitung auf dem Wasserstoff−Konzentration innerhalb des Gateoxides wurde charakterisiert und der Effekt auf die Drahtverbindungszuverlässigkeit von bewusst aufgebrachter Titanverunreinigung auf die Bondpadoberfläche wurde untersucht.

Contents

1

Introduction

1.1 The progress of semiconductor industry and surface analytics

(a) Moore's law, describing the number of compo-
nents, which can be placed inexpensively onto an
integrated circuit from the year[2]

(b) Kryder's Law, describing the hard disk storage
cost per unit of information[2]

Figure 1.1: Moore's (right figure) and Kryder's law (left figure), showing the progression
of the semiconductor industry in the last fifty years till now.

In the history of semiconductor industry the transistor has a unique position. Nowadays
the transistor is practically present in nearly all modern electronics. Its influence on society
and global economy cannot be estimated.

The semiconductor history is reviewed in various articles and books [2, 3, 4]. Only a few

---

[2]figures from wikipedia [1]

important milestones of the transistor history are given here.

About sixty years after John Bardeen, Walter Brattain and William Shockley demostrated their first transistor (Nobel prize in 1956) and fifty years after the production of the first silicon transistor (produced by Texas Instruments in 1954) and the first MOS transistor (produced at Bell Labs 1960), the invention of the transitor is considered to be one of the greatest in the twentieth century [5, 6, 7].

In 1965 Gordon E. Moore described in a paper that the number of components, which can be placed inexpensively onto an integrated circuit had doubled every year from its invention in 1958 till 1965 and predicted that this trend will last at least 10 years [8]. His prediction is now common known as *Moore's law* (figure 1.1(a))and has been a guiding principle for research & development in semiconductor industry. Next to Moore's law several other laws − as *Kryder's law* (figure 1.1(b)), which demonstrates the hard disk storage cost per unit of information − show the progress of semiconductor industry.

The progress of semiconductor devices was delayed from time to time due to different problems: e.g. diffculties encountered controlling impurities (sodium at the interface between silicon and silicon oxide) [9]. Although the level of impurities decreased drastically (to less than one part in one billion), contaminations can still cause serious problems and reduce the reliability of semiconductor devices (e.g. in modern cars microsensors have to work reliable during the whole life time of the car [10]).

In order to maintain a high quality standard and continuous manufacturing improvement, contamination monitoring and analysis is necessary. The requirements of the analytical instruments is increasing with the improving materials and processes [11].

The increasing number of transistors per integrated circuit is related with the reduction of a single component. With the shrinkage of semiconductor device size, the importance of contaminations during the production process grew even more. Higher standards for process monitoring, surface and failure analytics were required, due to the progress of semiconductor industry.

It is necessary to control atomic compositions down to concentrations of ppm−ppb. One tool for such sophisticated tasks is **T**ime−**o**f−**f**light **s**econdary−**i**on−**m**ass−**s**pectrometry (ToF−SIMS). Hence, it has always been an important contribution to the development of semiconductor devices and their technological processes. It can address several problems including diffusion, contamination, process monitoring [12].

1.2 Scope and Structure of the Work

In semiconductor industry contamination monitoring is an essential part for optimal product performance as contaminations can influence device reliability.

The scope of this thesis "Characterization of contaminations on semiconductor surfaces and thin layer systems with $\mathbf{T}$ime$-\mathbf{o}$f$-\mathbf{F}$light$-\mathbf{S}$econdary$-\mathbf{I}$on$-\mathbf{M}$ass$-\mathbf{S}$pectrometry" (ToF$-$SIMS) is to locate contaminations and study their impact on device reliability.

After a short description of the basics of the used surface spectrometry method and an overview of the used instrument, the first experiment is described. Within the first experiment $\mathbf{m}$etal $\mathbf{o}$xide $\mathbf{s}$emiconductor $\mathbf{f}$ield $\mathbf{e}$ffect $\mathbf{t}$ransistor (MOSFeT) have been monitored by means of ToF$-$SIMS and $\mathbf{a}$uger $- \mathbf{e}$lectron $- \mathbf{s}$pectrometry (AES) after specific process steps. The found contaminations have been allocated to their sources.

Based on the gained data of the first so$-$called *wafer$-$split$-$experiment* (section 3), further experiments were planned addressing airborne organic contamination resulting from transportation (section 4) and contamination owing to manufacturing processes (section 5 and section 6).

Finally a short summary and a conclusion of the work are given in chapter 7.

Basics

2
Basics

2.1 Secondary Ion Mass Spectrometry − SIMS

Secondary Ion Mass Spectrometry (SIMS) is a sputter based analytical technique to determine the chemical composition of a sample. The first experimental setup was introduced by in the 1940s by Herzog and Viehböck [13]. Since then the technique has been modified and improved. Due to it's outstanding characteristics, it is used in many different fields to analyze the elemental and molecule compositions of samples. It has the possibilities to detect all elements (including hydrogen) with a good lateral and depth resolution as well as a high analytical sensitivity (in the ppm − ppb range).

2.1.1 Principle of SIMS

The concept of secondary ion mass spectrometry is based on the principle that high energy primary ions are able to interact with a bombarded sample surface. The impact of the primary ions on the surface leads to a *collision cascade* (figure 2.1), which is − in simple terms − an energy and momentum transfer from the primary particles to the sample [14].
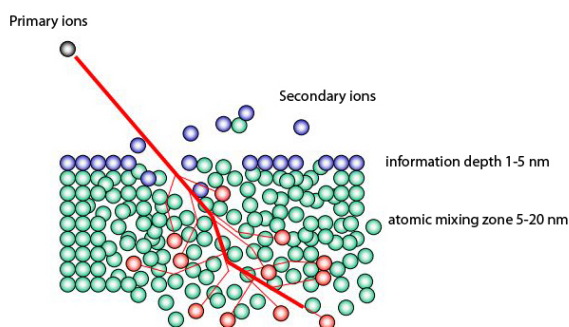
Figure 2.1: Sputter process & collision cascade[1]

The interaction between the primary ions and the bombarded surface modifies the sample surface and leads to the emission of electrons, neutral particles and positive and negative secondary ions. The emitted ions are characteristic for the surface formation of the sample, hence it is possible to analyse the chemical composition of the uppermost layer. As mentioned above the sample surface is modified and therefore destroyed during the measurement. This limitation leads to two main operation modes:

- ***The Static SIMS Mode*** (section 2.1.3)

- ***The Dynamic SIMS Mode*** (section 2.1.4)

After the formation of the secondary ions, the charged particles need to be separated and directed towards an ion detector. This can be done by different types of mass analyzers. Although there exist many separation and detection systems to analyze produced secondary ions, the main commercial available systems are time−of−flight mass analyzers, sector field mass spectrometers and quadrupole instruments (section 2.1.2). During this thesis a $TOF.SIMS^5$ instrument from **IONTOF** (Münster, Germany) was available. Such an instrument has the following analytical characteristics:

- The possiblity to detect all elements (including hydrogen) & molecules, fragments and clusters (mass range up to 10000 mu)

- Isotope sensitivity

- High lateral resolution ($>$ 70 nm to approx. 4 μm measurement mode dependent)

---

[1]figure from company−internal documents of ION−TOF GmbH

- Good depth resolution (small information depth < 1 nm)

- Parallel mass detection

- Low detection limit (ppm−ppb)

- Destructive method (negligible changes in the sample surface composition in the *Static SIMS mode*)

- Quantification is very difficult (due to the complexity of secondary ion formation)

- Quantification only possible using "standards" for calibration (section 2.1.5)

- Sample restrictions (high to ultra high vaccum conditions are necessary)

- high mass resolution (up to 10000)

- Charge compensation possible by means of an electron floodgun

2.1.2 Mass Analyzers

As mentioned before the principle of mass spectrometry is based on generating charged particles and analyzing them via a mass analyzer. There are several ways to separate the ions by their mass−to−charge ratio.
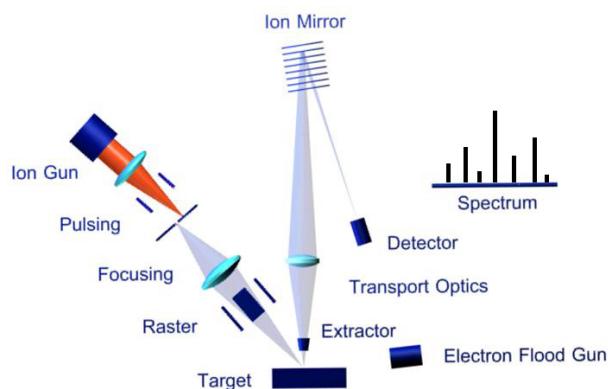

Figure 2.2: Time−of−flight mass analyzer (reflectron type)[2]

The most common mass analyzers in SIMS are *quadrupole mass spectrometer*, *double focused sector field instruments* and *time−of−flight mass analyzer* (figure 2.2). In principle the ions are sorted by their masses by applying electromagnetic fields and (or) by their

---

[2]figure from company−internal documents of ION−TOF GmbH

time−of−flight. The sector field instruments have a better lateral resolution and lower detection limit than time−of−flight (ToF) instruments, but ToF mass spectrometers are more flexible (e.g. the *static sims mode* is only available for ToF−SIMS instruments).

For ToF measurements the primary ion beam needs to be pulsed to guarantee the correct correlation between time−of−flight and mass of the ions. The time measurement starts at the pulsing of the primary ion beam. According to literature the time−of−flight principle works as follows [15]:

The short pulse of primary ions (energy $\approx 10 - 25$ keV) hit the sample surface and leads to an almost instantaneous emission of secondary ions. The secondary ions (of a given polarity) are accelerated into a drift section of a defined length L_d by means of an electrostatic field U_a (*extractor* energy $1-3$ kV). All secondary ions have been accelerated to the same nominal kinetic energy E_{kin} and enter the field free drift section with different velocities v according to their mass m.

$$E_{kin} = \frac{m \cdot v^2}{2} = e \cdot U_a \tag{2.1}$$

For a given secondary ion energy, the travel time T through the drift region to the detector is directly proportional to the length of the spectrometer:

$$T = \frac{L_d}{v} = L_d \cdot \sqrt{\frac{m}{2 \cdot e \cdot U_a}} \tag{2.2}$$

The lightest ion has the highest velocity, the heavier ions are slower and have therefore a longer time−of−flight. ToF analyzers are capable of parallel mass detection (with a perfect detector: ignoring the death time of the detector et cetera), because all ions of a given polarity will arrive at different times depending on their masses.
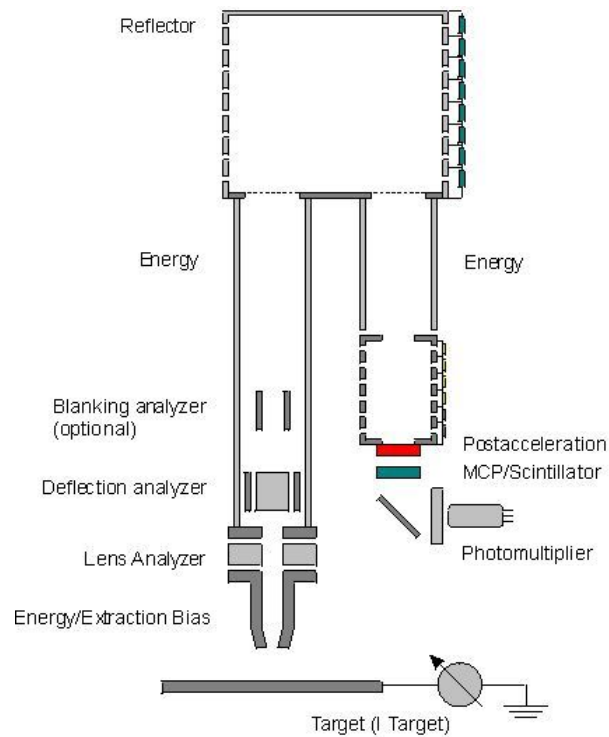
Figure 2.3: Schematic of a reflectron with a time−of−flight path of the emitted secondray ions[3]

The *mass resolution* − which is essential for the quality of the mass spectrum − is defined as the observed mass value divided by the smallest mass difference Δm (between two equal magnitude peaks such that the valley between them is a specified fraction of the peak height) for two ions that can be separated [17]. For ToF analyzers the *mass resolution* $\frac{m}{\Delta m}$ depends on the time resolution $\frac{t_0}{\Delta t}$:

$$\frac{m}{\Delta m} = \frac{t_0}{2 \cdot \Delta t} = \frac{1}{\gamma} \tag{2.3}$$

Looking at this formula (formula 2.3) it should be clear that the mass resolution improves as the flight time − and therefore the spectrometer length − increases, but the mass resolution is limited by other properties as well (e.g. the primary ion pulse width and speed of the detector system for low masses & the voltage stability of the analyzer and the ion detector for higher masses) [15]; but the most limiting factor to the mass resolution for a *linear ToF analyzer* is that secondary ions of the same mass are not emitted with the same energy but with a little energy dispersion. A longer drift tube will even lead to a broadening of the ion packet, hence a longer time of flight will not enhance mass

---

[3]figure from company−internal documents of ION−TOF GmbH [16]

11

resolution.

In order to compensate this "energy error (ΔE)", *Energy focusing ToF−SIMS analyzers* can be used. A commonly used instrument to reduce the energy broadening is a *reflectron* (figure 2.3), which is a combination of an ion mirror and two drift regions. An electrostatic field reflects the secondary ions to reduce the time dispersion. As all ions are subjected to the same electrostatic field, ions with the same mass but slightly higher kinetic energy will be reflected a little bit later and therefore have a longer flight path. Hence the secondary ions with identical mass are "bunchend" together. The ToF-SIMS instrument, which was available during this thesis is equipped with such kind of reflectron.

If the sample is an insulator or a semiconductor the sample surface will charge up due to the bombardment of the primary ions. The potenital between the extractor and the sample surface will vary and hence the kinetic energy of the secondary ions in the drift tube. An additional charge compensation is needed. Sample charging for ToF−SIMS analysis is in general positive. Standard charge compensation works by applying low energy electrons via an electron flood gun (figure 2.2) onto the target surface between two extraction pulses and a readjustment of the reflectron voltage [18].

2.1.3 The Static SIMS Mode

The *Static SIMS Mode* is used to get the information of the surface chemistry of an (organic) sample. Therefore the primary ion bombardment has to be controlled in such a way that the bombardment induced changes to the molecular formation are negligible. According to literature the maximum allowable primary ion dose limit (*static SIMS limit*) can be defined as follows [19]:

"If σ is the area at the surface which on average is affected by a primary ion (disappearance cross section) and A is the totally bombarded area then one can write for low primary ion dose densities:

$$\sigma_{total} \approx \Sigma\sigma = PID \times \sigma \ll A$$

$$\text{or with}$$

$$PIDD = \frac{PID}{A}$$
$$PIDD \ll \frac{1}{\sigma}$$

(2.4)

PID primary ion dose
$PIDD$ primary ion dose density

Typical values for σ are in the order of $10^{-13}-10^{-15}\ cm^2$ depending on the sample material and the bombardment conditions." Therefore the value for the *static SIMS limit* should not exceed 10^{12} to $10^{13}\ ions/cm^2$. It is assumed that less than 1 % of a monolayer is destroyed within that limit, thus the degradation of the first monolayer does not influence the measurement results in a significant way. Static SIMS has already been successfully used to analyse the chemical composition of the first layers on semiconductors, biological samples, ionic liquids and many more [20, 21, 22, 23].

2.1.4 The Dynamic SIMS Mode

In contrast to the *Static SIMS mode* the *Dynamic SIMS mode* exceeds the static sims limit. An ion beam is used to erode the sample surface continuously in order to generate depth profiles and gain information of the layer composition of the sample. The interaction of the primary ions with the sample surface changes the sample composition into a new equilibrium state. Therefore the information of the first layers is lost until the new equilibrium state − the "*dynamic balance*" between primary ions, original sample and the ambient gas phase − is reached. In the Dynamic SIMS mode it is possible to analyze the chemical composition layer by layer with a depth resolution in the nm regime and with a sensitivity down to the ppm−ppb range (depending on the element of interest) [14]. SIMS uses different primary ions (O_2^+ or Cs^+) to analyze and/or erode the sample surface. Sector field mass spectrometer use a continuous primary ion beam for both: generation of the secondary ions and echting of the sample surface. Generally O_2^+, Cs^+ and Ar^+ are used as primary ion species for sector field instruments. The change of the primary ion species can lead to an enhanced sputter− and ion− yield. The emission of secondary positive ions is increased by eroding with O_2^+, the emission of secondary negative ions by eroding with Cs^+, respectively. This enhancement can be about several orders of magnitude. Combined with the imaging capacity of SIMS three−dimensional element mappings can be generated.

In contrast to sector field mass spectrometer ToF−SIMS cannot use a continuously primary ion beam for depth profiling (see also section 2.1.2), therefore depth profiles are carried

out in the so−called *Dual−Beam−Mode* [24]. A pulsed high energy (25 keV) primary ion beam with low current (approx. 1 pA) is used to generate secondary ions and analyze the target surface. Alternating, a second beam with low energy (0.5 keV − 2 keV) and high current (up to 600 nA) erodes the sample surface. In order to achive a high *sputter yield* − which is defined by the number of secondary ions aquired per incident particle − **L***iquid* **M***etal* **I***on* **G***uns* (LMIG) are used as primary ion sources [25]. In principle these sources consist of a sharp − metal or alloy covered − tungsten tip ($\varnothing \approx 10\ nm$) (figure 2.4).
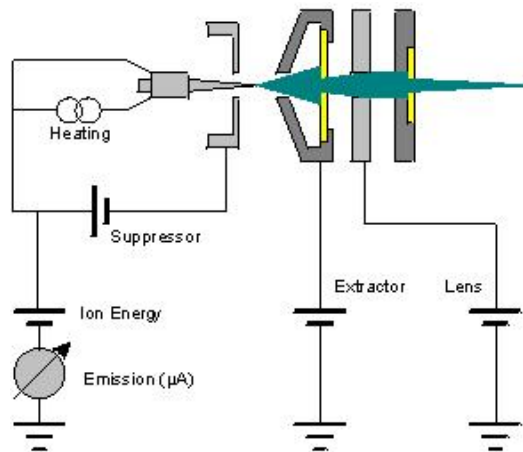
Figure 2.4: Schematic of a primary ion source (LMIG)[4]

In order to generate a primary ion beam the tungsten tip is heated to generate a liquid phase. A continuous current of primary ions is extracted from the ion−optical axis of the tip by applying an external voltage. Afterwards the beam is focused and guided through an ion−optical stack to form the desired short pulses of primary ions.

The preferable material properties for these emitters are:

- low melting point

- high mass

- mono−material (best case mono−isotopic)

Prominent materials for these tips are gold (Au) and bismuth (Bi), both have the possibility to form ion clusters. The instrument at hand uses Bi as primary ion source with the ability to generate $Bi_{1-7}^{\pm}$ clusters. These clusters may increase the sputter yield, which is not only desirable for depth profiling but also for imaging purposes. The sputter yield

---

[4]figure from company−internal documents of ION−TOF GmbH [16]

depends on the mass of the primary ion, its energy and angle of incidence as well as the composition of the sample. The sputter yield has a maximum for an energy of the primary ions of about 8 keV. As mentioned before the primary ion accerleration energy is about 25 keV for this instrument. The acceleration energy is the same for all primary ion clusters. The impact on the sample surface destroys the ion cluster, hence a Bi_3^+ has only one−third of it's acceleration energy, which corresponds to the maximum of the sputter yield.

The lower energy is also favorable for organic characterization, because it leads to a reduced atomic mixing. The Bi ion implantation destroys the sample surface. In particular organic surfaces tend to fragment into small pieces, which makes it's identification very difficult. Larger Bi cluster enhance the formation of large organic fragments. This can be used to identify organic substances [20, 22, 21, 26].

2.1.5 Quantification in SIMS

Quantification in SIMS means the conversion of the measured secondary ion intensity into analytical concentrations. Although this sounds easy, it is complex in reality. The dependence of the secondary ion intensity is given by the following equation:

$$I_{S(A)} = I_P \cdot S \cdot \alpha_A^\pm \cdot i_{S(A)} \cdot \eta_A \cdot c_A \tag{2.5}$$

$I_{S(A)}$ Secondary ion intensity of the measured isotope of the element A [ions / s]

I_P Primary ion intensity [ions / s]

S   Sputter yield [atoms / primary ion]

$\alpha_A^\pm$ Positive respectively negative ionization probability of the sputtered atoms

$i_{S(A)}$ Isotope frequency of the measured isotope of the element A

η_A Efficiency of the secondary ion measurement (output of the ion extraction, transmission of the mass spectrometer, efficiency of the detector)

c_A atom concentration of the element A in the sample

For depth profiling the sputter time needs to be converted into a depth scale. The crater depth can be measured with a stylus (a *profilometer*) or an optical instrument (a *white light interferometer* or a *digital holography microscope − DHM*). This approach is only correct under the assumption that the sputter rate is constant during the measurement. One has to keep in mind that the etching rate will vary from layer to layer, hence this will only work for single layer systems. Otherwise the sputter rate has to be determined for every layer.

2.1.6 Relative sensitivity factors − RSF

Relative sensitivity factors are used to correct instrumental instabilities (e.g. instabilites in the primary ion current). The concentration of an element A in the sample is referred to the concentration of an internal reference element, commonly a main compound of the sample (e.g. a Si isotope in a Si−wafer)[27].

$$\rho_{A/B} = \frac{I_P \cdot S \cdot \alpha_A^{\pm} \cdot i_{S(A)} \cdot \eta_A}{I_P \cdot S \cdot \alpha_B^{\pm} \cdot i_{S(B)} \cdot \eta_B} = \frac{I_{S(A)} \cdot c_B}{I_{S(B)} \cdot c_A} \tag{2.6}$$

$\rho_{A/B}$	Relative sensitivity factor
I_P	Primary ion intensity [ions / s]
S	Sputter yield [atoms / primary ion]
$\alpha_A^{\pm}$, $\alpha_B^{\pm}$	Positive respectively negative ionization probability of the sputtered atoms of the element A respectively B
$i_{S(A)}$, $i_{S(B)}$	Isotope frequency of the measured isotope of the element A respectively elements B
η_A, η_B	Efficiency of the secondary ion measurement (output of the ion extraction, transmission of the mass spectrometer, efficiency of the detector) for the element A respectively B.
$I_{S(A)}$, $I_{S(B)}$	Secondary ion intensity of the measured isotope of the element A respectively B [ions / s]
c_A, c_B	Atom concentration of the element A respectively B in the sample

RSF are commonly used in SIMS for quantification. Usually an implant standard with a defined dose is used to calculate the RSF. It is calculated from sum of the concentrations in each depth over the whole implantation range, which corresponds to the implantation doses. The RSF is assumed to be constant over the whole concentration range [28].

$$\rho_{A/B} = \frac{\sum_i^z \frac{I_{S(A)(i)}}{I_{S(B)(i)}} \cdot d}{Q_d \cdot z} \tag{2.7}$$

z	Number of cycles
$I_{S(A)(i)}$, $I_{S(B)(i)}$	Secondary ion intensity of the measured isotope of the element A respectively B at cycle i [ions / s]
d	Depth [cm]
Q_d	Implantation doses [$atoms/cm^2$]

The concentration of the analyte A can be calculated after deriving the RSF:

$$c_A = \frac{I_{S(A)} \cdot c_B}{\rho_{A/B} \cdot I_{S(B)}} \tag{2.8}$$

In general the RSF is constant for concentrations over several orders of magnitude, but it is only valid for the same sample matrix. Therefore new RSF have to be determined for the same element of interest in different sample matrices.

Experimental

3

Characterization of process induced bond pad contaminations

3.1 Introduction

The production of a typical semiconductor device consists of more than 100 process steps, each manufacturing process can induce contamination on the device. "Contaminants" are usually ordinary foreign atoms, molecules or particles, which are chemically and physically different from the desired layer materials (e.g. metal−, alkali ion−, organic− or inorganic contaminations) [29].

Even low levels contaminations on bond pads might influence device reliability and assembly processes of semiconductor devices, therefore they need to be controlled for optimum product performance [30]. For instance, particles have been made responsible for about 75% of the yield loss of volume manufactured VLSI chips. In general, contaminations of electronic products are mainly caused by:

- **Operators**

- **Environment** (clean rooms, transport & atmospheric contamination)

- **Equipment**

- **Processes** (Ion implantation, plasma etching, chemical vapor deposition, thermal treatment, metallization, ...)

Process contamination can be illustrated as a "food chain". It includes generation, transportation and deposition of the particles onto the wafer (figure 3.1).
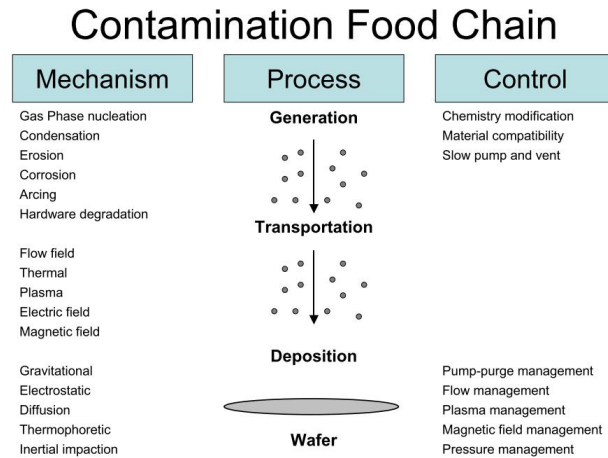

Figure 3.1: Contamination food chain[1]

Owing to the trend towards very small structure widths, the amount and the size of tolerable defects has been significantly reduced. In contrast, the number of possible particle sources has drastically increased due to more complex processes and smaller lethal particle sizes. [29].

It is already well known in literature that **T**ime−**o**f−**F**ight **S**econdary **I**on **M**ass **S**pectrometry (ToF−SIMS) is capable to detect trace elements (in the ppm − ppb range). Therefore it is the ideal tool for monitoring and failure analysis in semiconductor industry. It can provide useful information for a broad range of problems, including:

- General contamination studies (organic and inorganic)

- Debonding

- Discoloration

- Particle analysis

- Changes in resistivity

- Changes in wettability

- Incomplete etching

---

[1]figure from basic semiconductor books [29, 31]

- Over etching

- Void formation

- Changes in electron emission

- Additive segregation

The product's performance of high technology industries − like the semi conductor industry − can easily be affected by contaminations [32].

In this section ToF−SIMS and **A**uger − **E**lectron − **S**pectrometry (AES) are used to detect and identify contaminations and their possible causes on typical MOSFeT devices after different process steps.

3.2 Sample preparation[2]

Samples of an eight inch n−channel MOSFeT device with a 5 μm $AlSi(1)Cu(0.5)$ metallization were manufactured at our project partner Infineon. The samples were broken into two pieces, one half was sent to the university of technology Vienna for ToF-SIMS analysis and the other one to Siemens CT Munich for AES measurements. An *Entegris* wafer box was used for transportation. The influence of the transport on the (organic) contamination level and therefore on the ToF-SIMS results was focus of another experiment and is discussed in section 4.

---

[2]In co−operation with Infineon, Villach

sample	process	sampling	comment	Imidprocess	Snit	Imid NB
2	AlSiCu structured	post polymer removal	reference	no	no	no
3	AlSiCu structured + annealing	after annealing	annealing	no	no	no
6	AlSiCu structured + annealing + 40nm SNIT, Imid Ratio, Cure, SNIT AE	post SNIT etching	compare with (c.w.) #13, #16: SNIT-AE duration	Ratio	40	no
7	AlSiCu structured + annealing + 40nm SNIT, Imid Ratio, Cure, SNIT AE, $Ar-O_2$, BEOL Std	whole Flow	c.w. #10: cleaning $Ar-O_2$ vs. Recess 40	Ratio	40	$Ar-O_2$
9	AlSiCu structured + annealing + 40nm SNIT, Imid Ratio, Cure, SNIT AE, Recess 40sec	post SNIT etching	c.w. #10: BEOL process	Ratio	40	no
10	AlSiCu structured + annealing + 40nm SNIT, Imid Ratio, Cure, SNIT AE, Recess 40sec, BEOL Std	whole Flow	c.w. #9: BEOL process c.w. #7: cleaning $Ar-O_2$ vs. Recess 40 c.w. #17: SNIT-AE duration	Ratio	40	Recess 40
13	AlSiCu structured + annealing + 800nm SNIT, Imid Ratio, Cure, SNIT AE	post SNIT etching	c.w. #6, #16: SNIT-AE duration	Ratio	800	no
16	AlSiCu structured + annealing + 800nm SNIT, Imid Ratio, Cure, SNIT AE	post SNIT etching	c.w. #6, #13: SNIT-AE duration	Ratio	800	no
17	AlSiCu structured + annealing + 800nm SNIT, Imid Ratio, Cure, SNIT AE, Recess 40, BEOL Std	whole Flow	c.w. # 10: SNIT-AE duration	Ratio	800	Recess 40
18	40nm SNIT, Imid Ratio, Hardbake, Recess 25sec, SNIT AE, Cure	post imide cyclization = sample 19	c.w. #21, #22	std	40	no
19	40nm SNIT, Imid Ratio, Hardbake, Recess 25sec, SNIT AE, Cure	post imide cyclization = sample 18	c.w. #21, #22	std	40	no
20	40nm SNIT, Imid Ratio, Hardbake, Recess 25sec, SNIT AE, Cure, Recess 13sec, $Ar-CF_4$	post $Ar-CF_4$	c.w. #21, #22: $Ar-CF_4$	std	40	$Ar-CF_4$
21	800nm SNIT, Imid Ratio, Hardbake, Recess 25sec, SNIT AE, Cure, Recess 13sec	post Recess = sample 22	c.w. #18, #19: Organic-cleaning effect Recess 13	std	800	recess 40
22	800nm SNIT, Imid Ratio, Hardbake, Recess 25sec, SNIT AE, Cure, Recess 13sec	post Recess = sample 21	c.w. #18, #19: Organic-cleaning effect Recess 13	std	800	recess 40
23	800nm SNIT, Imid Ratio, Hardbake, Recess 25sec, SNIT AE, Cure, Recess 13sec, $Ar-CF_4$, BEOL Std	whole Flow	c.w. #24: BEOL	std	800	
24	800nm SNIT, Imid Ratio, Hardbake, Recess 25sec, SNIT AE, Cure, Recess 13sec, $Ar-CF_4$	post $Ar-CF_4$	c.w. #23: BEOL	std	800	

Table 3.1: Detailed process steps of the investigated MOSFeT devices

The samples were carried out after different process steps (detailed processes in Table 3.1), in order to allocate process immanent contaminations on aluminium bond pads and identify their sources. Several processes have been investigated:

- **Back End Of Line** (BEOL) process: includes every process step after "*Metal 1*", it is a general term for processes after the contact hole etching.

- **Recess 40** process: is an O_2 remote plasma process to clean wafer surfaces from organic residues. The substrate is not supposed to plasma but only etched purely chemically.

- $Ar-O_2$ process is an anisotropic plasma process, hence has an additional abrasion

of the surface in comparison to the *Recess 40* process.

- $Ar - CF_4$ is an anisotropic plasma process to activate the surface for an electro-chemical deposition at a succeeding process step.

- **Annealing** metal relaxation process at $430°$ C for 30 min in reducing or inert atmosphere

- **protective nitride layer thickness variation**: Si_3N_4 is a very hard and brittle material, hence a increased layer thickness leads to an enhanced stress level in the device.

3.3 Experimental settings for ToF−SIMS analysis

The ToF-SIMS measurements have been performed in the so−called *Static−SIMS−Mode*, in order to analyse the uppermost surface (information depth approx. 3 monolayers) [19]. The *primary ion dose* (PID) was set to $1 \cdot 10^{11}$ $ions/cm^2$ and is therefore well below the *static SIMS limit* (see also section 2.1.3). Considering target current measurements of the primary ions, the influence of the primary ion cluster species on the gained fragmentation pattern and literature references Bi_3^+ has been chosen as primary ion species. Bi_3^+ reduces the fragmentation of organic contaminations in comparison to Bi_1^+. The emission current has been reduced to 0.5 μA to enhance the emission of ion clusters from the LMIG. The primary ion current is stable during the measurement with this parameter setup. The target current itself was measured with a Faraday−Cup in positive polarity. All additional light sources have been turned off, to minimize the formation of secondary electrons generated by photo−emission processes and therefore their influence on the current measurement. Target current measurements and all measurements on the semiconductor surfaces − either in positive or negative polarity − have been performed at a cycle time of 100 μs. The mass range, which is predetermined by the cycle time is $0 - 930$ mu (Table 3.2).

cycle time [μs]	mass range [mu]
30	$1 - 79$
40	$1 - 141$
50	$1 - 221$
60	$1 - 318$
70	$1 - 432$
80	$1 - 565$
90	$1 - 715$
100	$1 - 882$
120	$1 - 1270$
140	$1 - 1728$
160	$1 - 2257$
180	$1 - 2856$
200	$1 - 3526$

Table 3.2: Mass range as a function of cycle time from 30 to 200 μs [3]

3.4 Results & Discussion

3.4.1 Characterization of the Bi−Emitter & determination of the Static SIMS measurement setup

In order to determine the optimum parameter setup for investigations of bond pad contaminations the target current of different primary cluster ions (Bi_1^+, Bi_3^+ and Bi_5^+) has been measured as a function of the emission current. The same cycle time (100 μs) has been used for the target current measurements and for the investigations on the bond pads. Every measurement has been repeated three times to average statistical fluctuations in the target current, the estimated error of these measurements is about 10%.
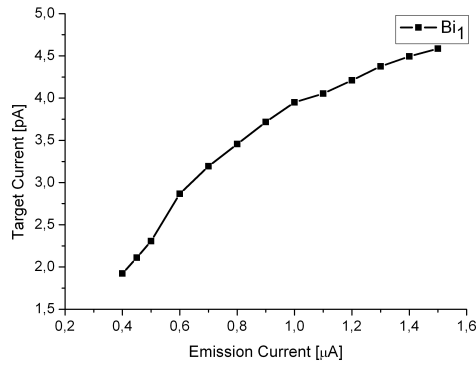
---

[3] values from ION−TOF software

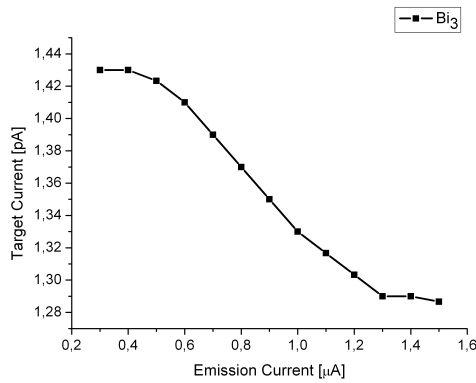Figure 3.2: Target current as a function of the emission current for Bi_1^+ primary ions

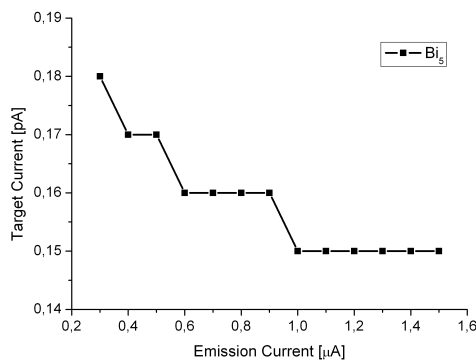Figure 3.3: Target current as a function of the emission current for Bi_3^+ primary ions

Figure 3.4: Target current as a function of the emission current for Bi_5^+ primary ions

Figures $3.2 - 3.4$ show the target current as a function of emission current for Bi_1^+, Bi_3^+ and Bi_5^+. A clear relation between pulsed primary ion target$-$ and emission current

is shown:

For mono−atomic species the target current decreases, when the emission current is reduced (figure 3.2). Higher clusters show the opposite behaviour, the measured target current is increasing, if the emission current is lowered (figures $3.3 - 3.4$).

A decrease of the emission current from 1.5 μA to 0.4 μA results in a decrease from 4.6 to 1.9 pA of Bi_1^+ − and an increase from 1.28 to 1.43 pA of Bi_3^+ ion current. The characteristic of the Bi−emitter shows that the relative enhancement of the pulsed target current is even bigger for higher $Bi-cluster-ions$ (comparison of Bi_3^+ & Bi_5^+).

It is well known in literature that primary cluster ions show a better fragmentation pattern than "single" primary ions [33]. It would be favorable to use primary ion clusters as large as possible for the analysis of organic matter (see also section 2.1.3). Nevertheless absolute current values are decreasing for larger clusters, which enhance the measurement time and therefore the possibility of measurements artefacts (e.g. fluctuations in the target current). For Bi_6^+ and Bi_7^+ the target current was not measureable anymore with the given setup.
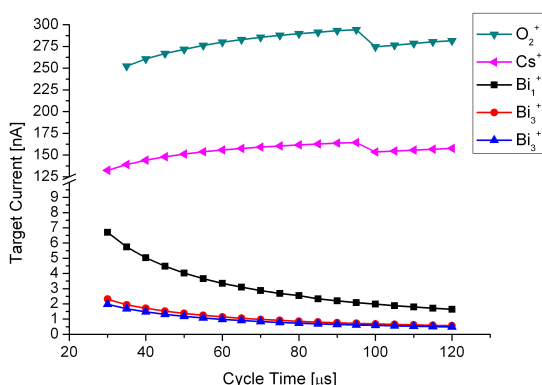

Figure 3.5: Target current as a function of the cycle time for Bi_1^+, Bi_3^+, Bi_3^{++} primary ions and the sputter guns (O_2^+ & Cs^+ 1 keV setup)

In order to enhance the target current, it would be necessary to reduce the *cycle time*, but this would reduce the mass range, which is not favorable for the analysis of organic materials (Table 3.2 and 3.5). As a result of these investigations Bi_3^+ with an emission current of 0.5 μA was used for all further static SIMS measurements, which is a good trade−off between pulsed target current, gun stability and fragmentation formation (see also section 2.1).

26

3.4.2 Characterization of prozess− induced bondpad contamination on MOSFet− devices

Samples of a MOSFet−device have been taken out after different process steps and measured by means of AES and ToF−SIMS in order to identify possible contaminations and allocate them to their sources. An overall overview about contamination in semiconductor industry and their possible impact on the device has already been discussed (see also section 3.1).

samples	O at%	Al at%	C at%	F at%	Alox-D	N at%
2	59,1	18,6	16,4	6	0,9	
3	60,8	20,2	15,2	3,8	1	
6	48,9	23,9	15,7	11,6	1,3	
7	33,7	16,9	40,8	8,5	1	
9	54,3	22,4	12,3	11	0,84	
10	38,3	19,2	33,6	8,9	1,15	
13	48,8	22,4	15	13,7	0,9	
16	51,1	21,5	13,4	14	0,9	
17	35,5	19,3	35,5	11,4	0,9	
18	35,3	15,9	45	2,1	1	1,7
19	34,2	15,3	47	1,8	0,9	1,7
20	15,1	12,4	53,9	18,6	1,3	
21	60,3	22,2	11,3	6,3	0,84	
22	60,4	21,5	11,9	6,1	0,84	
23	38,6	20,2	26,8	13,8	0,8	
24	24,3	21,1	22,4	29,9	0,9	2,3

Table 3.3: AES results of the CoolMOS wafer samples

AES measurements just showed the relative concentrations of oxygen, aluminium, carbon, fluorine, aluminium oxide and nitrogen. It is not possible to get any information of the organic formation with AES, aside from the overall carbon signal. The results of the AES measurements are shown in table 3.3.

In contrast to AES, ToF−SIMS has the capability to detect all elements and therefore discover and identify unexpected contaminations[4].

---

[4]The parameter setup for *Static SIMS* measurements has been determined by a comparison of the results of prior investigations of the Bi−emitter characterization and a literature study.
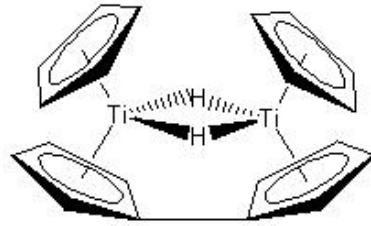
Figure 3.6: Titanocen Dimer[5]

Besides the already mentioned and by means of AES investigated contaminations, titanium contamination was found in ToF−SIMS measurements (figure 3.7). This contamination corresponds to the progress in the wafer process (figure 3.6). Titanocene is used as a radical starter in a particular polyimide resin. Even several process steps after introducing polyimide, containing this particular contamination, titanium can still be found on the sample surface (figure 3.7). Therefore this contamination can affect the wire bond process (see also chapter 5).
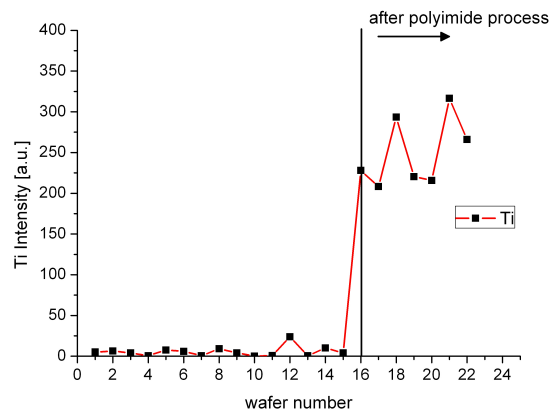
Figure 3.7: Titanium contamination on aluminium bond pads as a function of manufacturing process steps.

In general, AES and ToF−SIMS showed similar results and contamination levels (by comparing the relative intensities displayed in figures 3.8 − 3.12 [6] and table 3.3):

- The combination of process instabilities and measurement error can be investigated by comparing wafer #13 and #16, which have seen the same processes. The variation

---

[5]figure from wikipedia [34]

[6]The notation "organic" in figure **??** is a synonym for several C_xH_y−cluster, the notation "$AlOF$−cluster" for serveral $Al_xO_yF_z$−cluster, respectively

of the AES measurements was up to 1.5%. Figure 3.8 shows the variation range of for the process induced contamination (of a specific process: SNIT layer) and the ToF−SIMS measurements. The ToF−SIMS measurement error is at most 10%.

- AES measurements reveal that the **B**ack **E**nd **O**f **L**ine (BEOL) process enhances the concentration of fluorine and carbon on the sample surface (wafer # 9 vs. # 10 & wafer # 23 vs. # 24). ToF−SIMS confirm these results and show an increase of the chlorine concentration as well (figure 3.11).

  In general, halogen contamination may lead to discoloration and weak wire bonds on aluminium bond pads, because of irritation of the intermetallic phase formation, corrosion and increased oxide growth [35]. Furthermore fluorine has an influence on the reliability of gate oxides [36]. As already mentioned before the BEOL process includes every process step post "Metal 1". During the BEOL process several additional layers are deposited, which are possible contamination sources. The BEOL process also pushes hydrogen toward the gate oxide (section 6.3.2).

- The thickness of silicon nitride (SNIT) with the respective change in etching time has no influence on the contamination level of the bond pads, or at least cannot be measured (wafer # 10 vs. # 17 & wafer # 6 vs. # 13, #16; figure 3.12). The variation was within the error of measurement of the AES and ToF−SIMS analysis.

- The comparison of two used plasma processes (*Recess 40* (wafer # 10) and $Ar − O_2$ (wafer # 7)) is given in figure 3.10. Both processes show similar results, but do not reduce the organic contamination on the bond pads significantly.

- The measured fluorine content of all samples varied for AES measurements between 1.8 and 29.9 $at\%$. Annealing at a certain temperature (at $430°$ C) leads to a rise in the $AlO_2−$ and $O−$ signals and a clear reduction of fluorine, AlF_4 and all $AlOF−$cluster (wafer # 2 & wafer #3; figure 3.9). It seems that the fluorine diffuses into deeper layers. Once fluorine reaches the GOX it can cause serious problems [36, 37, 38]. A clear increase of fluorine concentration was detected after the $Ar − CF_4$ process (highest concentrations for wafer # 20 & #24 with $Ar − CF_4$).
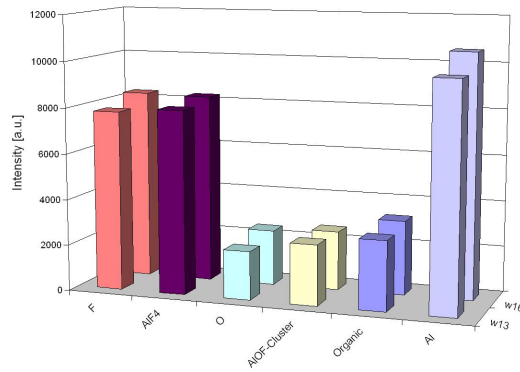
Figure 3.8: Fluctuation of the process induced contamination and measurement error of the ToF−SIMS measurments.
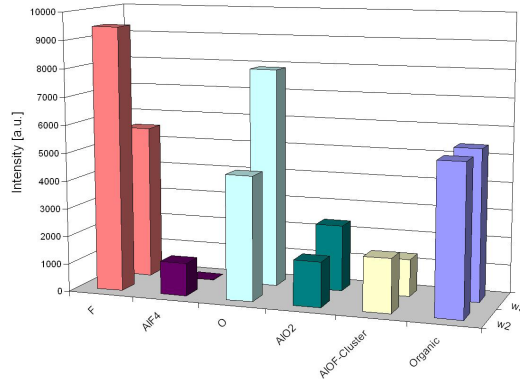

Figure 3.9: Influence of Annealing on the bond pad contamination level. Comparison of wafer # 2 (no anneal) with wafer # 3 (annealing at).
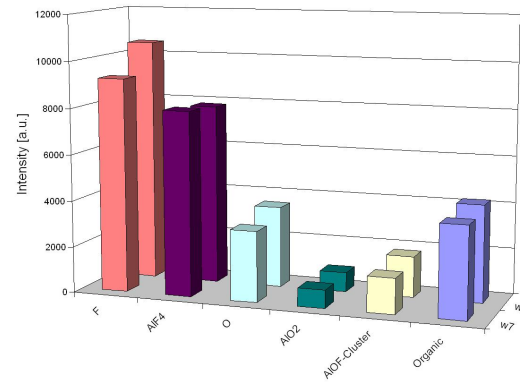

Figure 3.10: Comparison of the cleaning effect of the $Ar - O_2-$ (sample # 7) and the $Recess40-$ (sample # 10) plasma processes.
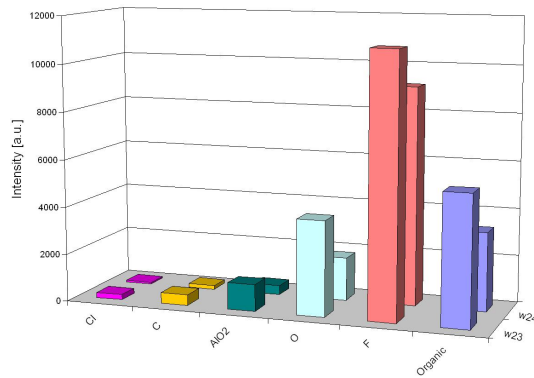
Figure 3.11: Influence of BEOL on the bond pad contamination level. Comparison of wafer # 23 ($Ar - CF_4$ & BEOL standard process) with wafer # 24 (only $Ar - CF_4$ process).
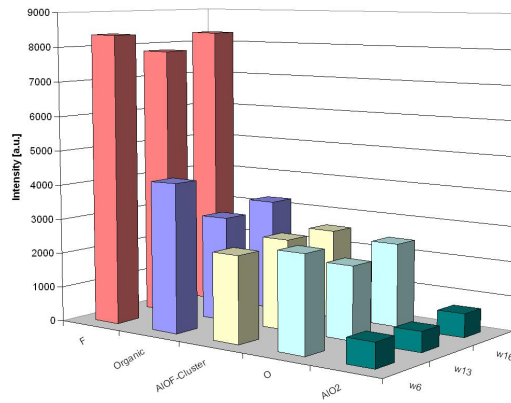
Figure 3.12: Influence of $SNIT - layer$ thickness on the bond pad contamination level. Comparison of wafer # 6 (40 nm thickness) with samples # 13 & # 16 (800 nm thickness).

4

Organic Contamination

4.1 Introduction

Organic contamination has been found on bond pad surfaces in previous studies by means of AES and ToF−SIMS (section 3). Possible contamination sources are:

- Manufacturing processes

- Environment (clean rooms, transportation & atmospheric contamination)

- Operator

- Equipment

Wafer production and further device fabrication need not be on the same location, often wafers are shipped to different locations (e.g. for wire bonding prozesses). The devices are exposed to contaminations during transportation. Next to atmospheric contamination, outgassing of organic materials of transport boxes and packing material may influence following assembly processes. Plastic bags and transport boxes are commonly known to introduce additional contaminations onto sample surfaces [32].

In this section the possibility of the analysis of volatile organic contaminations with ToF-SIMS is discussed. Organic contaminations from transportation and environment were monitored with ToF−SIMS and GC−MS.
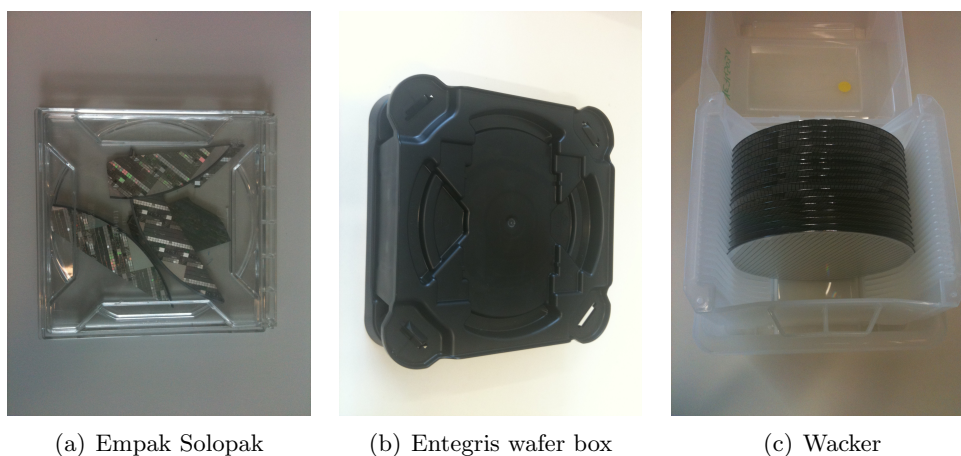
4.2 Sample preparation and measurement settings[1]

(a) Empak Solopak   (b) Entegris wafer box   (c) Wacker

Figure 4.1: Different transport boxes used in semiconductor industry

Samples of eight inch n−channel MOSFeT devices with a 5 μm $AlSi(1)Cu(0.5)$ metalliza-tion were used to investigate the impact of transportation on the organic contamination level. The reference sample of previous studies (section 3; sample 2 in Table 3.1) was used for this investigation as well.

Present organic contamination on the samples had carefully been removed by annealing (at $400°$ C) and ultrasonic application in acetone and ethanol, then the samples were dried with nitrogen. This procedure should ensure the removal of any residual surface adsorbates (cleaning effect displayed in figures 4.2 & 4.3).

Afterwards the cleaning procedure was monitored by means of ToF−SIMS, to get a ref-erence contamination spectrum. Two samples each were transferred into one wafer box (*Entegris, Empak Solopak* figure 4.1) for one week at $50°$ C temperature in order to simulate transportation. In order to reduce the possibility of introducing additional con-taminations, these procedures were performed as fast as possible and at the same time for all sample batches. The samples were analyzed at the Vienna University of Technology by means of ToF-SIMS.

All ToF-SIMS measurements were carried out in the *Static SIMS mode* on a $ToF-SIMS^5$ instrument [2] equipped with a Bi−LMIG as primary ion gun. The measurements were per-formed with the same parameter setup as in previous investigations (details in section 3.3):

---

[1]In co−operation with Infineon, Villach
[2]from IONTOF, Germany

Pimary ion dose:	$1 \cdot 10^{11} \; ions/cm^2$
Primary ion species:	Bi_3^+
Cycle time:	$100 \; \mu s$
Emission current:	$0.5 \; \mu A$
Area of Interest:	$300 \times \; 300 \; \mu m$

Next to ToF−SIMS measurements gas chromatography−mass spectrometry (GC−MS) investigations were carried out at the Siemens CT (Munich). The samples were transfered warped in aluminium foil to prevent additional contamination due to transportation.

4.3 Results and Discussion

Static SIMS spectra were carried out on several spots of each sample batch. In the *Static SIMS mode* it should be possible to analyze/identify molecular contaminations at the topmost monolayer with a high lateral resolution [39]. In principle ToF−SIMS is a powerful technique for chemical surface analysis, nevertheless data interpretation can be very complex [40].

ToF−SIMS spectra display the signal intensities of the generated secondary ions as a function of their masses. The secondary ion formation is influenced by the primary ions, the organic contamination covering the substrate surface and the substrate itself [41]. Furthermore the relative signal intensities of a ToF−SIMS mass spectrum vary under different cluster ion bombardment, the signals of higher mass fragments are increasing under higher cluster ion bombardment (Bi_n^+; $n = 1 - 7$) [21, 22].

Primary ions interact with the substrate and their energy is transfered to the sample. The sample surface and therefore also the organic material on the surface is destroyed during this process, only fragments of the organic substances reach the detector. The gained spectra of unknown organic contaminations/fragments can be compared with reference spectra from searchable libraries[3], but due to possible *cross−contaminations* and variations of the library spectra − taking into account different matrix signals and SIMS techniques (primary ion guns) − the real composition of a unknown sample can only be estimated.
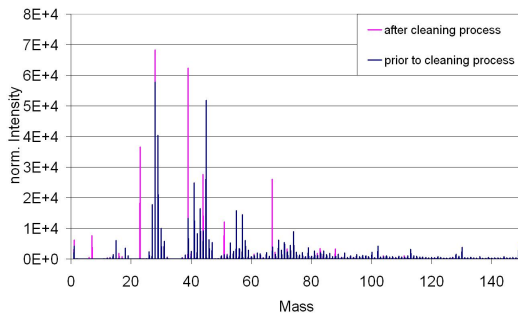
---

[3]library provided by IONTOF

Figure 4.2: Comparison of static SIMS spectra before and after cleaning measured in positive mode
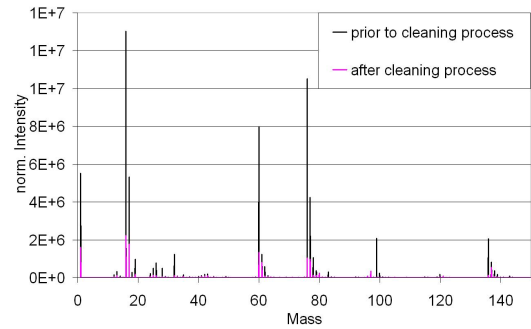

Figure 4.3: Comparison of static SIMS spectra before and after cleaning measured in negative mode

The mass spectra of airborne organic contamination on a Si−wafer and the mass spectra of the reference sample after cleaning are displayed in figure 4.2 (ToF−SIMS measurement in positive mode) and figure 4.3 (ToF−SIMS measurement in negative mode). The main components of organic contamination are decreasing after cleaning, while additional contaminations (Na^+, K^+) are also applied onto the sample surface. These signal peaks were neglected in the mass spectra of the contaminated samples.
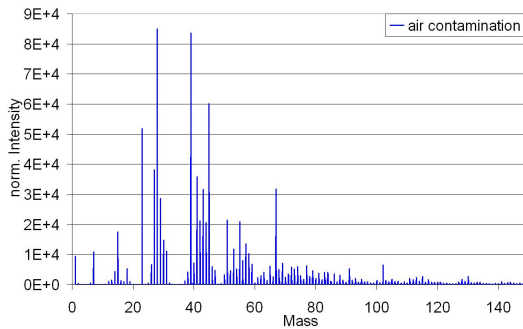
Figure 4.4: Static SIMS spectra of airborne contamination open stored in the laboratory measured in positive mode
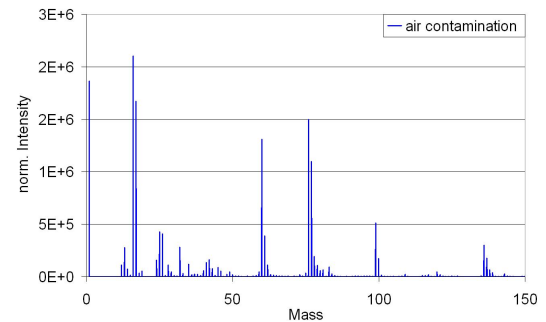
Figure 4.5: Static SIMS spectra of airborne contamination open stored in the laboratory measured in negative mode
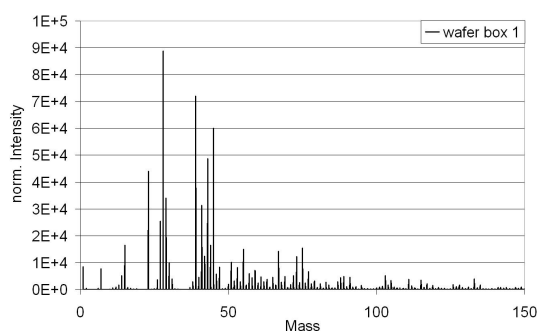
Figure 4.6: Static SIMS spectra of contamination found a sample stored in wafer box 1 measured in positive mode
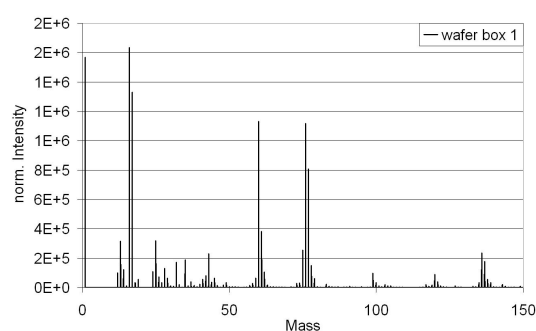

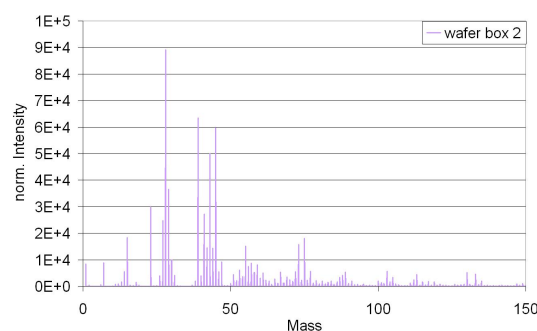Figure 4.7: Static SIMS spectra of contamination found a sample stored in wafer box 1 measured in negative mode

Figure 4.8: Static SIMS spectra of contamination found a sample stored in wafer box 2 measured in positive mode
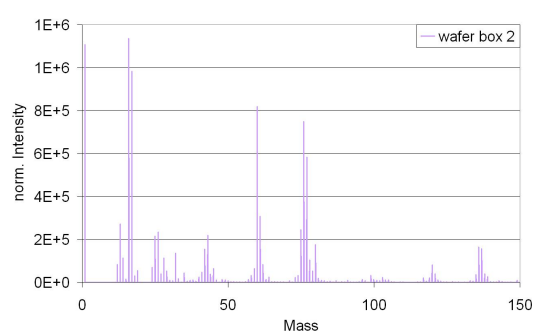

Figure 4.9: Static SIMS spectra of contamination found a sample stored in wafer box 2 measured in negative mode

Figures $4.4 - 4.9$ display the ToF$-$SIMS mass spectra of contaminated samples. The mass spectra of the transport boxes show similar organic contamination, the sample from the laboratory environment shows some additional mass peaks.

The main components of each mass spectrum have been compared with reference spectra from libraries and literature, revealing a correlation between the increased signals after contamination and mass peaks of polycarbonate[4] (PC), silicones[5] (polydimethyl$-$siloxane $[Si(CH_3)_2O]_n$) and phthalates[6]. Next to these contaminations PMMA[7] (polymethyl-methacrylat) is strongly suggested as additional contamination. The gained ToF$-$SIMS spectra seem to be a superposition of the peaks expected from these four molecules.

[4]polycarbonate mass peaks: 93, 117, 133, 149
[5]silicone mass peaks: 28, 73, 147, 207
[6]phthalate mass peaks: 121 & 149
[7]PMMA mass peaks: 31, 41, 55, 85, 141

Silicones were also detected by means of GC−MS (figures 4.10 − 4.12). They are known to be introduced during shipment, storage or device handling and are very mobile on sample surfaces, due to their low surface tensions and viscosities [32]. Hence they are often detected as indirect contamination. Next to silicones, DOP (Dioctyl−phthalate) and its degradation products were measured by means of GC−MS. It is used as plasticizer in manufacturing of articles made of PC.

All found organic contaminations are volatile and have significant vapour pressures in the ultra−high vacuum (UHV) of the ToF−SIMS main chamber. A cooled sample stage could be used to reduce the vapour pressure, hence more organic substances can be detected and signal intensities are increasing (even for higher masses) in the ToF−SIMs spectrum [32]. For the analysis of unknown organic substances with ToF−SIMS a cooling stage should always be used. Volatilization of airborne contaminants can be reduced, the gained information is significantly enhanced and therefore the chance of success is increasing. Unfortunately a cooling stage was not available during this experiment.
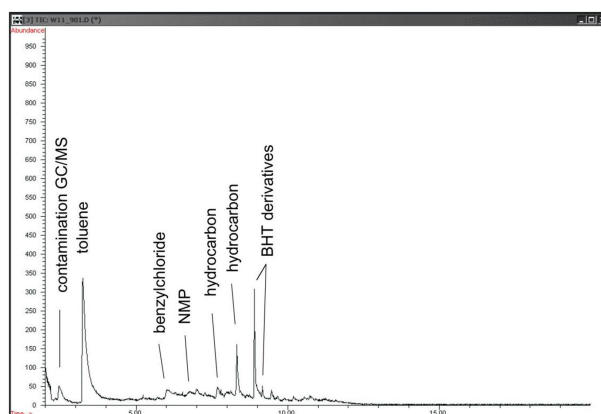

Figure 4.10: GC−MS data of the reference sample[8]

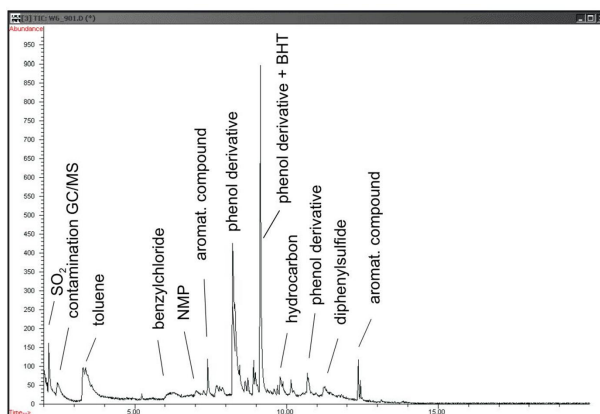[8]GC−MS data from Siemens CT report
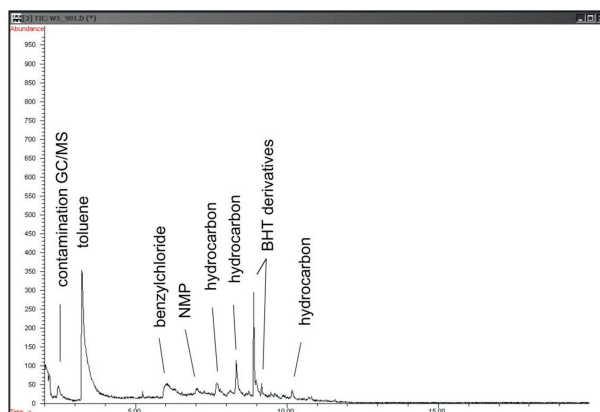
Figure 4.11: GC−MS data of wafer # 1[8]

Figure 4.12: GC−MS data of wafer # 2[8]

5

Titanium Contamination[1]

5.1 Introduction

Quality, performance and (long−term) reliabilty of semiconductor devices is highly demanded in applications for the automotive industry to satisfy high market requirements. One of the main life−time concerns and reliability problems of power devices are wire bond failures (e.g. bond wire lift−offs) [42, 43]:

During the on/off periods of the device a part of the controlled power is dissipated as heat within the device. Therefore a mismatch of the thermal expansion coefficient at each interface in the device can possibly lead to thermomechanical fatigue failures [44, 45, 46]. The most common failure modes, due to thermal fatigue, are solder cracks/propagation of fatigue cracks and bond wire lift−offs [47].

Poor bond force and contamination is expected to reduce fracture strength at the bonding interfaces [48]. It is already well−known in literature that contaminations (e.g. halogene) on aluminium bond pads can lead to discoloration and weak wire bonds , because of irritation of the intermetallic phase formation, corrosion and increased oxide growth [49]. Nevertheless, the infuence of metal contamination has not yet been investigated in detail. As titanium contamination has been found on bond pad surfaces in previous studies (section 3), its influence on bond wire reliability was investigated here.

Normally, procedures with accelerated power and temperature cycling (with extreme tem-

---

[1]details in publication B.1

perature excursions) are used to simulate the thermal stresses induced during applications [50, 46, 51, 52]. These thermal tests usually take a very long time.

In our case, different mechanical tests (shear− and vibration− tests) were performed on wire bonded samples to characterize the influence of breeded titanium contamination on the wire bond reliability. An ultrasonic resonance fatigue testing system in combination with a laser Doppler vibrometer was used to estimate the life time of the contaminated micro−joints. This allows a life−time approximation within a resonable time period [53]. The life time prognosis based on accelerated mechanical tests should be as reliable as the life time prediction of thermal tests procedures [54].

In order to get a deeper understanding of the fracture mechanism, ToF−SIMS measurements were performed on a batch of samples directly after titanium deposition, as well as on the fracture surface after life−time tests. Next to ToF−SIMS investigations, cross−sections of the wire bonds and fracture areas after the life−time tests were analyzed with a **S**econdary **E**lectron **M**icroscope (SEM).
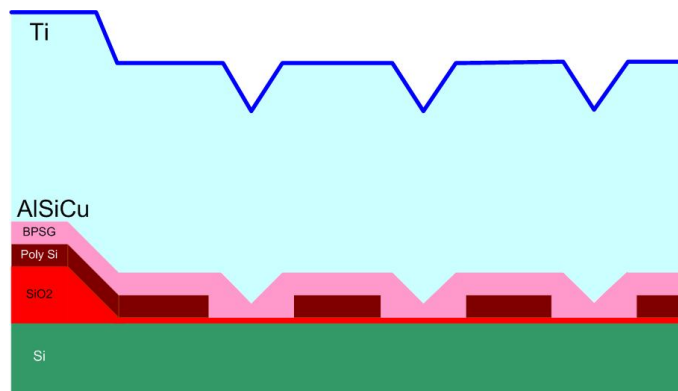
5.2 Sample preparation

Figure 5.1: Schematics of the contaminated device structures

Our project partners at Infineon Villach[2] and Infineon Warstein[3] were responsible for the sample preparation. The sample structure corresponds to the device structure of prior investigations. It is based on the same devices where the titanium contamination has been found (see also section 3). The additional extreme level titanium contamination was

---

[2]for device perparation prior to wire bonding
[3]for wirebonding

deliberately breeded onto the non-planarized low voltage n-channel MOSFeT device by the following method: on a batch of twenty−five silicon wafer different titanium layer thicknesses (0; 2; 6; 10 and 15 nm) were deposited by means of physical vapor deposition onto a 5 μm $AlSi(1)Cu(0.5)$ standard metallization, either directly after $AlSiCu$ deposition or after an so−called $air{-}break$ (Table 5.1). The samples with air−break stayed under ambient atmosphere between aluminium and titanium deposition. During the aluminium deposition the substrate temperature raises from $80°\ C$ to approx. $300°\ C$, because it was not actively controlled. The titanium deposition happened at constant $200°\ C$.

In order to reduce the influence of the surface topography on wire bond reliability and the sample costs the number of layers and workflows has been reduced to a minimum level (e.g. the contact holes haven't been etched; see also figure 5.1). Depending on the pattern below the surface topography is about 0.5 μm with an additional aluminium roughness of approximate 100 nm.

Sample number // Sample group	Preparation
1 (Reference)	no titanium deposition
2	2 nm without air−break
3	2 nm with air−break
4	6 nm without air−break
5	6 nm with air−break
6	10 nm without air−break
7	10 nm with air−break
8	15 nm without air−break

Table 5.1: Sample description & preparation

After titanium deposition one sample of each group was sent to Vienna for analytical characterization. All other samples were sent to Infineon Warstein for wire bonding. *Symmetric* wire bonds are favorable for vibration tests to minimize measurement failures. The devices were bonded using ultrasonic aluminium wedge bonding with a 200 μm aluminium wire.

Figure 5.2: Wirebonded devices, two asymmetric bonds for shear tests & one symmetric
bond for vibration tests, respectively

The wire was bonded on three devices to manufacture one symmetric wire bond (figure
5.2). The additionally manufactured *asymmetric* wire bonds were used to perform shear
tests. Life time tests were performed at the Department for Physics of Nanostructured
Materials at the University Vienna, shear tests at Infineon Villach.

5.3 ToF−SIMS measurement settings

A high energy beam with a good lateral resolution and a very low current ($\approx$ 1 pA)
− in order to avoid surface irritation during the measurement − was used for sample
analysis. All measurements were performed in the high current bunched (HCBU) mode
for enhanced mass resolution (lateral resolution 4 μm, mass resolution at 29 u more than
10500 full width at half maximum). .

The energy of the beam for material abrasion was set to 500 eV in order to increase the
depth resolution [55]. Both ion beams hit the target with an angle of 45°, which is favored
to minimize sample roughening.

A sample area of a 99.6 × 99.6 μm^2 was analyzed with a Bi_1^+ beam (25 keV energy,
128 × 128 pixel) in positive and negative mode. The pulse width of the primary ion beam
has been reduced to 2 ns in negative mode and 3.9 ns in positive mode, respectively.
These parameters lead to a better resolution for the titanium and aluminium signal at the
oxide interfaces. In addition, measurements at a pulse width of 19.9 ns were performed
for comparison.

Either an ion beam of O_2^+ particles (for enhanced positive ion detection), generated by an
electron ionization impact source, or Cs^+ particles (for enhanced negative ion detection),

generated by a thermal ionization source were applied to ablate the surface. The O_2^+ gun was used to determine the distribution of aluminum and titanium and the Cs^+ gun to characterize the oxides. The area for the removal of the surface was set to $300 \times 300 \ \mu m^2$ and all sputter guns were centered at the same point, in order to avoid crater side effects.

5.4 Results & Discussion

In order to correctly interpret failure mechanism of the wire bond interfaces it is crucial to investigate the used model system first. ToF−SIMS and AFM measurements were performed on a batch of samples before wire bonding to analyze the surface roughness and layer composition.

The following section is divided into two parts. The first section deals with the results of not−wire bonded samples while the second part describes the results of bonded devices.

5.4.1 Results on non−wire bonded devices

Characterization of the surface topography

Surface roughness measurements were performed by atomic force microscopy[7] (AFM) on an undisturbed sample surface and in the middle of one sputter crater with an area of interest of $3 \times 3 \ m^2$ area each. The topography of the poly silicon underneath the metallization limited the area for the surface microroughness measurement. The root mean squared R_q (equation 5.1)

$$R_q = \sqrt{\frac{1}{n} \cdot \sum_i^n y_i^2} \tag{5.1}$$

and the arithmetic average of the absolute values R_a (equation 5.2)

$$R_a = \frac{1}{n} \cdot \sum_i^n \mid y_i \mid \tag{5.2}$$

were calculated.

y_i vertical distance from the mean line at the ith data point

---

[7]with a MultiMode V instrument from Veeco

Crater depth measurements were performed − contactless − with a digital holography microscope[8] and compared to simulated data, as well as to profilometer depth measurements, carried out with a DekTak 6 stylus profilometer [9].

(a) AFM scan of sample 7
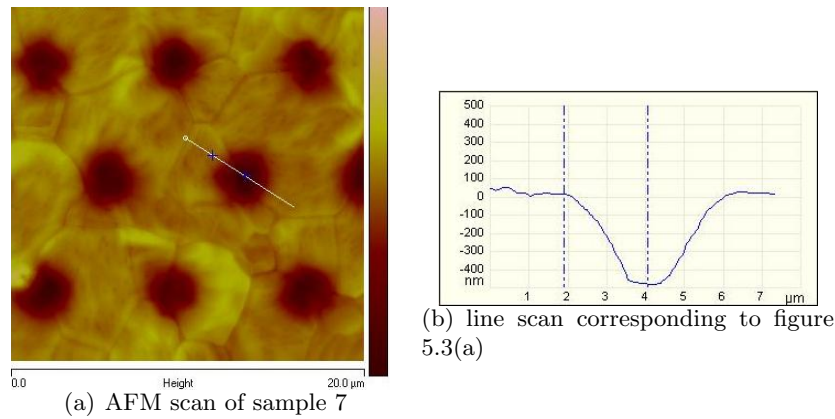

(b) line scan corresponding to figure 5.3(a)

Figure 5.3: AFM picture of sample 7 showing the contact holes and the grain structure of the $AlSiCu−$metallization

The depth resolution of SIMS analysis can be limited to surface roughening due to the angular, low energy primary ion beams. The effect of surface roughening during SIMS analysis was investigated of AFM (figure 5.3 & Table 5.2). The measurements showed nearly identical values on the initial surface and in the ToF−SIMS crater, hence the additional roughening induced by the sputter beam during SIMS analysis was negligible. The values for R_a and R_q on the different sample surfaces varied between 10 and 25 nm. These values are typical for sputtered $AlSiCu−$layers with that kind of pattern and thicknesses.

Sample	R_q [nm]	R_a [nm]
1	14,4	11,7
2	17,3	14,1
3	13,7	10
4	21,8	18,1
5	17,3	13,7
6	25,3	20,3
7	19,5 / (18,2)[11]	15,0 / (14,1)[11]

Table 5.2: Surface micro roughness of samples 1−7

---

[8]a DHM 1000 from Lyncee Tec SA, 1015 Lausanne, Switzerland

[9]from Veeco Instruments Inc

[11]measurements from the surface of a ToF−SIMS crater

ToF−SIMS measurements on the non−wire bonded samples

Before the influence of the breeded titanium contamination on the wire−bond reliablity can be investigated, the composition of the model system needs to be characterized. ToF−SIMS measurements were performed with a $TOF.SIMS^5$ instrument[12] on a batch of samples prior wire bonding. Depth profiling was performed in dual beam mode [24, 56] on *not−bonded samples* to characterize the composition of the samples and get a deeper understanding of the effect of an air break on the titanium distribution. The composition of the samples (thin layers of Ti on rough bond pads) requires an optimisation of the ToF−SIMS measurement parameter regarding signal intensity and depth resolution.
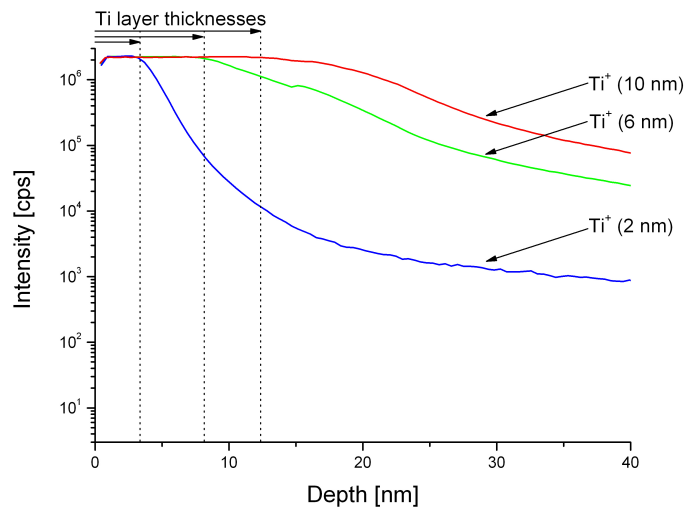
Figure 5.4: Depth profile measured in positive mode with 500 eV O_2^+ sputtering. De-stribution of the titanium signal of samples 3, 5 and 7 with 2, 6 and 10 nm Ti thickness, respectively. Oxygen in−cooperation leads to thicker Ti−layers than estimated.

A reduction of the sputter energy enables a clear determination of the different deposited titanium thicknesses (shown in figure 5.4). The oxidation of the titanium layer with ambient atmosphere leads to an increased thickness compared to the deposited layers. The effective titanium layer thickness of samples 3, 5 and 7 are 3, 8 and 12 nm, respectively.

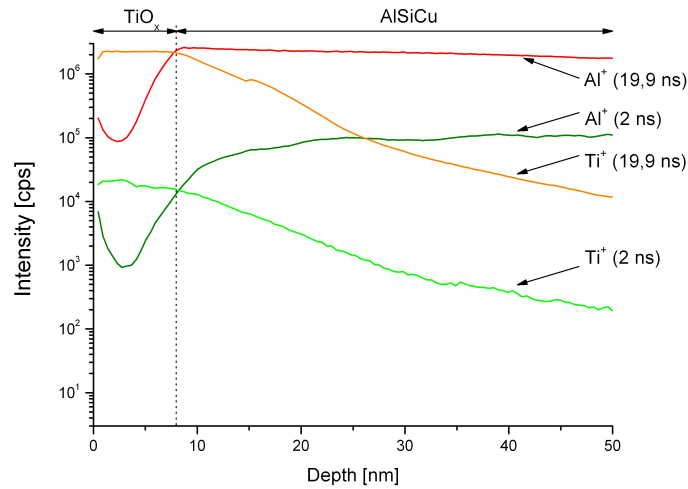[12]ION−TOF GmbH, Münster, Germany

Figure 5.5: ToF−SIMS depth profile of sample 7 measured with different pulse width (19.9 ns & 2 ns)

Owing to the fact that aluminium has only one isotope, a reduction of the primary ion intensity per shot is necessary to avoid detector overflow. A decrease of the cycle time reduces the measured current at the faraday cup (figure 3.5), but not the primary ions per shot and therefore will not change the yield of generated secondary ions.

Reducing the pulse width from 19.9 to 2 ns lowers the current of the LMIG from 2.9 to 0.034 pA and the primary ions per shot (current measurement at a cycle time of 50 μs). Figure 5.5 shows that this measure avoids detector overflow, therefore the aluminium and titanium distribution in the first few nm can be investigated without any information loss. However, the information of the $^{63}Cu^+$ and $^{65}Cu^+$−signals (and other trace elements) are lost, because they are below the detection limit.
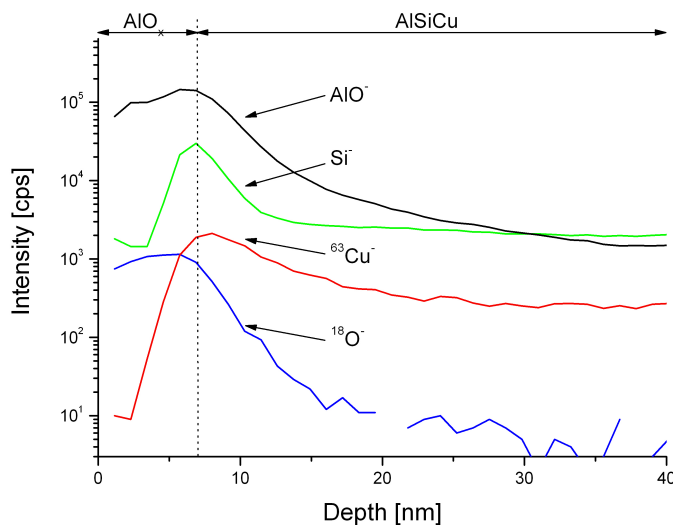
Figure 5.6: ToF−SIMS depth profile of sample # 1 measured in negative mode, demonstrating the effect of an air−break on the sample composition (oxide and metallization formation). Si^- and $^{63}Cu^-$ show a pile−up effect at the oxide/metallization interface.

In order to understand the effect of an *air−break* on the titanium's behavior, the self−passivating mechanism of aluminium alloys has to be investigated before. Figure 5.6 shows the ToF−SIMS profile of sample # 1 (reference without titanium) measured in negative mode. Contact of the deposited *AlSiCu* with ambient atmosphere leads to an oxide−layer formation with an approximate 6 nm thickness. The oxide−layer thickness of all samples was nearly identical, hence the self−passivation mechanism already stopped and the duration of the air−break was long enough to built up a complete oxide layer on top of the metallization.

Reaction	*Standard enthalpy at $RT[kJ/mol]$*
$Si \ + \ O_2 \rightarrow SiO_2$	-910.7
$4 \ Al \ + \ 3 \ O_2 \rightarrow \ 2 \ Al_2O_3$	-1675.7
$2 \ Cu \ + \ O_2 \ \rightarrow \ 2 \ CuO$	-157.3
$Ti \ + \ O_2 \ \rightarrow \ TiO_2$	-1520.9

Table 5.3: Chemical reactions and enthalpy at room temperature (RT) [16]

Moreover the aluminium, silicon and copper distribution close to the surface is changed

---

[16]values from CRC Handbook of Chemistry and Physics [57]

due to the reaction with the ambient atmosphere. After the PVD sputter process all deposited elements are equally distributed according to the target composition (figure 5.6 at a depth of $30 - 40$ nm). Al, Cu and Si compete with each other and try to interact with the oxygen of the ambient atmosphere as soon as the sample is taken out of the vacuum chamber (Table 5.3).

Aluminium has the highest affinity to oxygen, hence the topmost layer is almost pure aluminium oxide (see also figure 5.6). Si and Cu are concentrating at the metal$-$oxide interface during oxidation and do not contribute significatly to the oxide formation. Figure 5.6 shows a pile$-$up effect of the $Si-$ and $Cu-$ signals, which can be explained by the reduced solubility of Si and Cu in aluminium oxide. The oxide layer prevents Si and Cu from diffusing toward the surface.

Figure 5.7: A scan of a Richardson $-$ Ellingham diagram [17]

ToF$-$SIMS profiles of sample # 4 (without air$-$break; figure 5.8) and sample # 5 (with air$-$break; figure 5.9) $-$ both with the same deposited titanium thickness $-$ show the influence of an air$-$break on the titanium and aluminium distribution. The $Si^{\pm}-$signal was used to identify the oxide/metallization interface and valuate the measured crater depth.
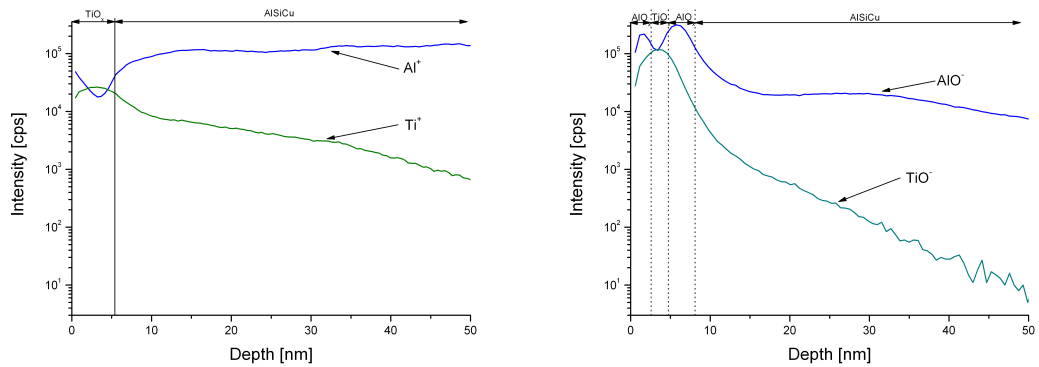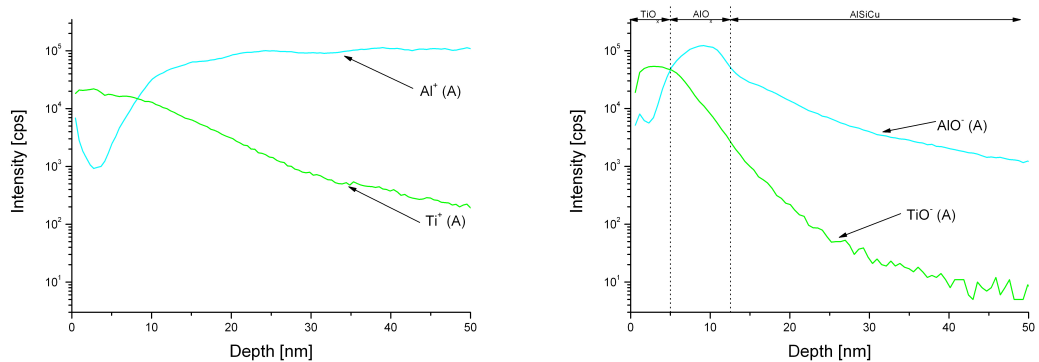
---

[18]as it appears in Handbuch Hochtemperatur$-$Werkstofftechnik, page 249 [58]

(a) ToF−SIMS depth profile of a sample without air break measured in positive mode after titanium deposition.

(b) ToF−SIMS depth profile of a sample without air break measured in negative mode after titanium deposition

Figure 5.8: ToF−SIMS profiles of sample # 4 measured in negative (figure 5.8(b) on the left side) and positive mode (figure 5.8(a) on the right side). Titanium diffuses into the $AlSiCu$−metallization.

(a) ToF−SIMS depth profile of a sample with air break measured in positive mode after titanium deposition.

(b) ToF−SIMS depth profile of a sample with air break measured in negative mode after titanium deposition

Figure 5.9: ToF−SIMS profiles of sample # 5 measured in negative (figure 5.9(b) on the left side) and positive mode (figure 5.9(a) on the right side). The aluminium oxide formation suppresses the interaction of the $AlSiCu$−metallization with the deposited titanium.

Without any air contact between titanium and aluminium deposition, the titanium can interact with the $AlSiCu$−metallization. It diffuses into layers underneath. Once the sample are taken out of the vacuum chamber, Ti, Al, Si and Cu want to react with the oxygen from the ambient atmosphere. Four reactions compeed with each other. According to their standard enthalpy (standard enthalpy at RT given in Table 5.3) and the corre-

sponding Richardson−Ellingham diagram (figure 5.7[18]), mostly aluminium will react with oxygen and build an oxide layer on top of the metallization. Although the titanium layer interacts with the oxygen first, aluminium diffuses − due to its higher oxygen affinity − to the surface (figure 5.8(b)).

In case the aluminium was exposed to air prior to the Ti deposition, a titanium oxide layer is formed on top of the Al_2O_3 layer, since the native aluminium oxide acts as a diffusion barrier for Ti and prevents the titanium from interacting with aluminium.

Looking at the ToF−SIMS measurements performed in positive mode (figure 5.9(a) & 5.8(a)) the same conclusions can be drawn. Only the sample without air−break shows a titanium diffusion profile (shoulder in diagram in figure 5.8(a)). The sample with air−break shows a continuous decrease of the titanium signal once the aluminium oxide layer is reached.

Beneath the already mentioned ToF−SIMS investigations, temperature dependent measurements down to $-100°$C have been performed and compared to room temperature results in order to valuate SIMS artefacts [59, 60, 61].
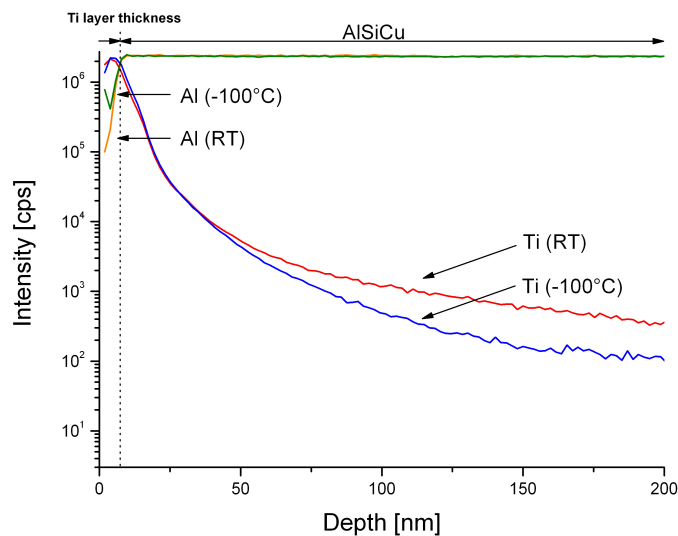

Figure 5.10: Temperature dependence of ToF−SIMS signals in $AlSiCu$ metallizations

We assume that a lower temperature leads to a reduced mixing zone, comparable to organic depth profiling [62]. On the one hand the Ti^+ signal decreases faster and on the other hand the shape of the Al^+ signal is different within the oxide. Although these

effects are reproducible, several other effects − like the surface roughness or sputter angle − contribute to the distribution of titanium and aluminium signals as well.

5.4.2 Investigations on wire bonded samples
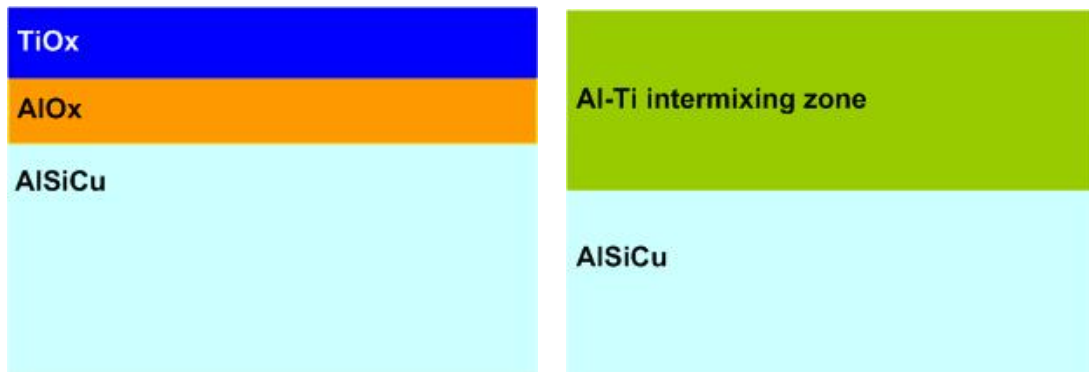
(a) Schematics of the titanium contaminated sample with air−break

(b) Schematics of the titanium contaminated sample without air−break

Figure 5.11: Schematics of the samples with breeded titanium contamination

In order to characterize the effect of breeded titanium contamination on wire bond reliability, the knowledge about the layer composition is essential. Two different model systems (schematics in figure 5.11) were developed to understand the influence of titanium contamination on wire bond reliability. The main difference between samples with & without air−break is the composition of the topmost layer:

The sample without air−break prior titanium deposition has a titanium/aluminium intermixing zone on top. The topmost layer of the sample with air−break consists of an titanium oxide layer, followed by an aluminium oxide layer and the $AlSiCu$−metallization.. The sample with air−break has a slightly higher oxide thickness[23].

The effect of metal contamination was tested by means of fatigue− and shear− tests. SEM and ToF−SIMS measurements were performed to investigate the failure mechanism of the micro−joints.

Determination of the effect of titanium contamination on the strength of adhesion of a semiconductor wire bond

Shear tests were performed on twenty to forty asymmetric wire bonds of each batch (Table 5.1 on page 41) with a *Condor 100[24]* instrument at Infineon Villach. The samples were glued onto a copper plate prior the shear test and the plate was mounted to minimize possible measurement failures. The measurement height was 160 μm, the needle diameter

---

[23]comparison of figures 5.9(b) & 5.8(b) on the page 49.
[24]from XYLTEC

$3\ mm$, the test velocity of $250\ \mu m/s$ and the test distance $900\ \mu m$, respectively.

(a) Devices with asymmetric wire bonds glued onto a copper plate

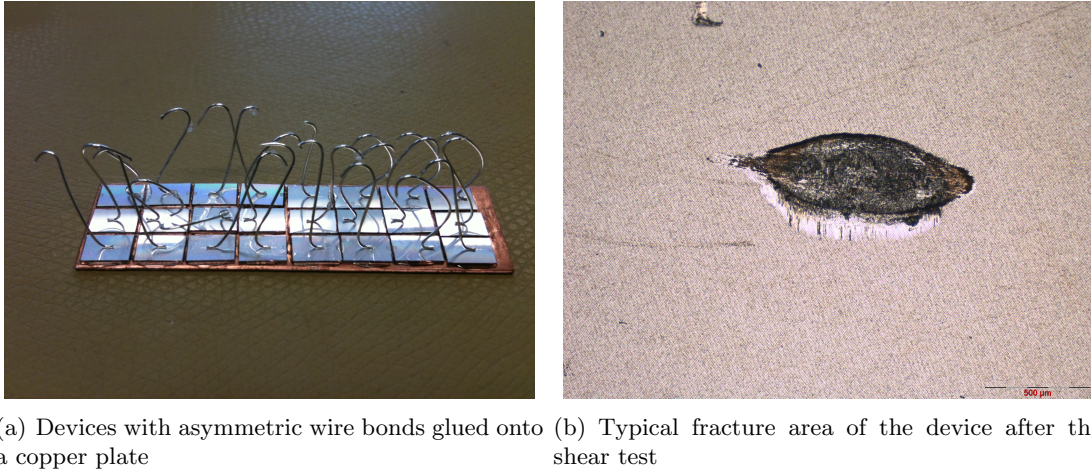(b) Typical fracture area of the device after the shear test

Figure 5.12: Pictures of the devices prior and the sample surface past shear testing

The $T-test$ was used to clarify if there is a relationship between the measured (normally distributed) shear values of the different sample batches. *Normal distribution* is a prerequisite for the $T-test$, therefore the $\chi^2 - test$ and *Kolmogoroff*−*Smirnov*−*test* were used to test if the received values were normally distributed[26]. Both confirm that the value distributions of each sample batch were normally distributed and the $T-test$ showed no relations between the distributions.
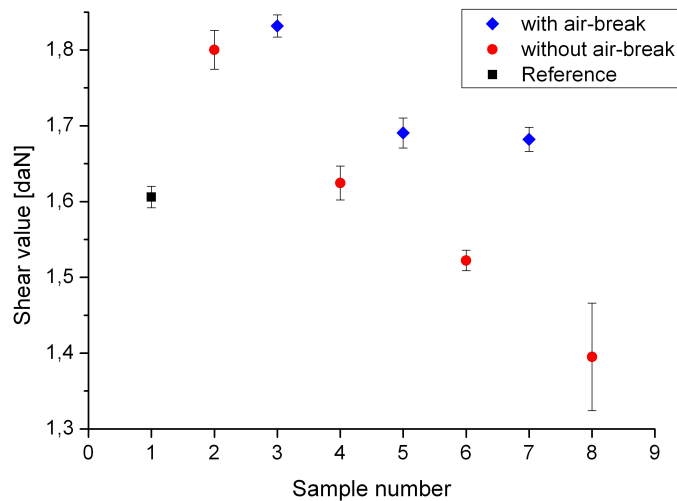
Figure 5.13: Shear test diagram corresponding to data in Table 5.4[29].

---

[26]details of the different statistic tests in [63]

Figure 5.13 and table 5.4 show the shear test results. Thin layers of titanium seem to have a positive effect on the bond interface, while thick layers of titanium seem to weaken the bond interface:

Samples with 2 nm titanium deposition show the highest shear values, thicker titanium layers reduce the necessary shear force for bond failure. Both kinds of samples with 2 nm titanium deposition showed nearly identical shear values. The shear value difference between the two models[27] increases according to the titanium thickness. Samples without air−break show lower shear values than samples with air−break and therefore seem to have a weaker bond interface.

Sample[28]	Shear values & standard deviation [daN]
1	$1,6061 \pm 0,014181$
2	$1,8003 \pm 0,025626$
3	$1,8317 \pm 0,014606$
4	$1,6245 \pm 0,022423$
5	$1,6905 \pm 0,019844$
6	$1,5223 \pm 0,013409$
7	$1,6821 \pm 0,015792$
8	$1,395 \pm 0,070909$

Table 5.4: Shear test values from each sample batch. Samples with 2 nm titanium deposition show the highest shear values, thicker titanium layers reduce the necessary shear force for bond failure. Samples without air−break show seem to have a weaker bond interface than samples with air−break.

Life time tests[30]

Figure 5.14: CAD-drawing of the used specimen holder[31]

Instead of *thermal−* or *power− cycle tests*, an *ultrasonic resonance fatigue test* was used to assess the quality and reliability of contaminated aluminium wire bonded micro−joints

---

[27]schematics shown in figure 5.11 on page 52
[29]sample number corresponding to Table 5.1 on page 41
[30]details of the experimental set−up in [54] [53]
[31]picture provided from DUHS GmbH

under shear loading at room temperature. The main advantage of this method is, that it can be performed within a reasonable time interval. This system works with a constant test frequency of 20 kHz, hence data points for fatigue life curves can be obtained up to a number of 10^9 loading cycles within fourteen hours.
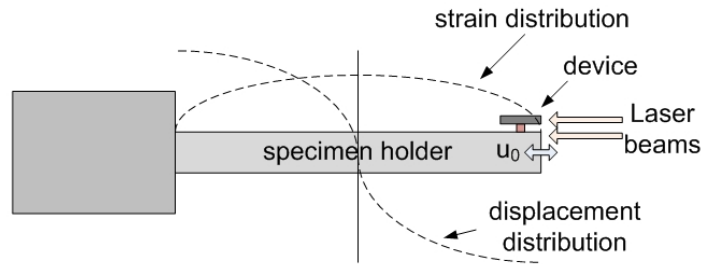

Figure 5.15: Schematics of the strain−displacement distribution of the micro−joints [32]

Each micro−component was attached to a specimen holder (figure 5.14), which was used to apply forced cyclic, longitudinal vibrations to the device. During loading, the maximum displacement occurs at the end of the specimen holder, the maximum strain at the mid−section, respectively (figure 5.15). Depending on the adjusted excitation amplitude the displacement and strain varies (figure 5.16).

---

[33]figure based on [54]
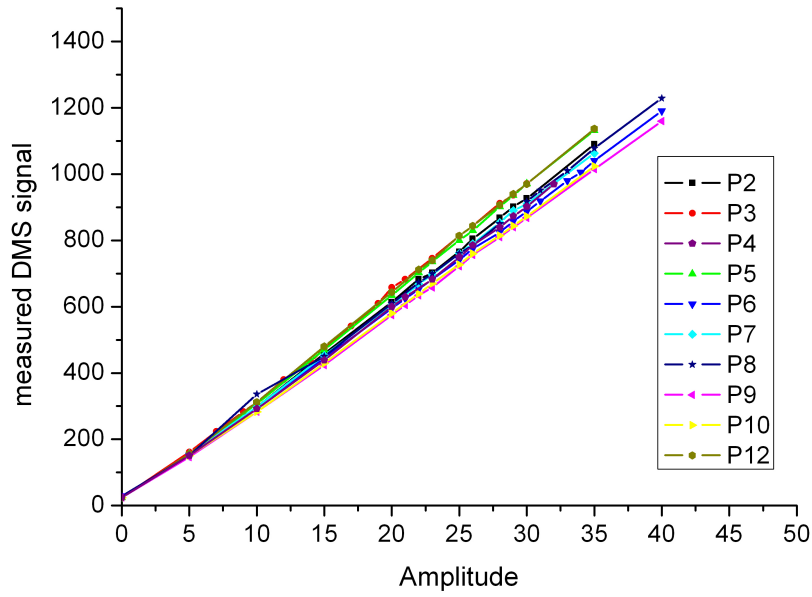
Figure 5.16: Measured DMS signal vs. adjusted amplitude for each sample holder. The strain and velocity can be adjusted with the used excitation amplitude.

The applied shear force F on the device is given by:

$$F = m \cdot a \tag{5.3}$$

F shear force
m device mass
a acceleration of the device // displacement

(a) Schematics of the device attached to the specimen holder

(b) Schematics of the device attached to the specimen holder with an applied force
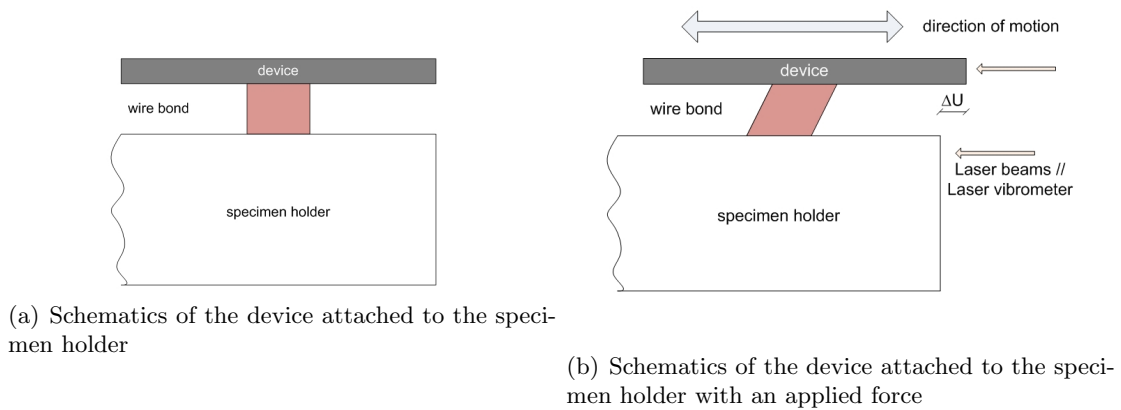
Figure 5.17: Schematics of the used shear fatigue testing system without (figure 5.17(a)) and with (figure 5.17(b)) applied force [33]

The displacement is calculated with a resistance strain gauge, which is located in the mid$-$section of the specimen holder. The vibration velocity ϑ_{max} of each specimen holder was measured with a laser doppler vibrometer (LDV) and plotted as a function of strain (measured via a strain gauge)[36]. Measured velocity and strain showed a linear relationship, which corresponds to literature results (figure 5.18). Literature gives an estimated error of the shear strain measurements in such an experimental setup of approx. $\pm$ 5% [54].
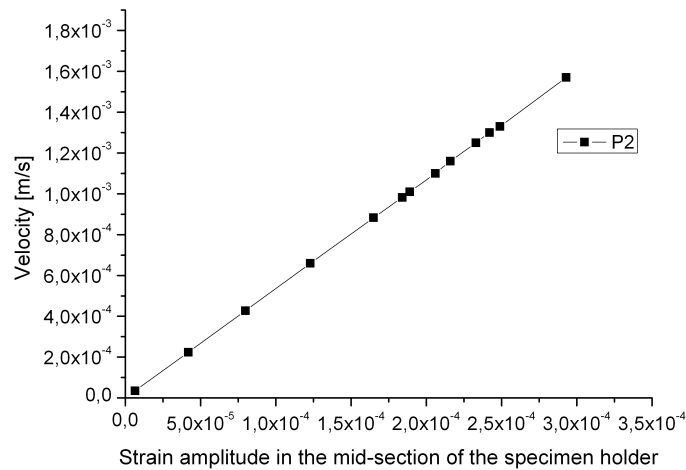
Figure 5.18: Plot of the vibration velocity measured with the LDV vs. strain measured in the mid$-$section of the specimen holder, showing a linear correlation between velocity and strain.

---

[36]schematics of the experimental set$-$up in figure 5.17

The device acceleration can be caluclated with the measured velocity:

$$a_{max} = 2 \cdot \pi \cdot f \cdot \vartheta_{max} \tag{5.4}$$

a_{max} peak acceleration
f frequency
ϑ_{max} vibration velocity

After the received LDV results were calibrated with a transducer (Polytec model $CLV-100$ with a peak velocity of 2.5 m/s and a resolution of 4 $\mu m/s$), the vibration velocity, measured with the LDV at the free end of the specimen holder was used to calibrate the calculated velocity, derived from the measured strain amplitude at the mid$-$section of the holder. The shear strain distribution can be calculated via:

$$\varepsilon = \frac{2 \cdot \pi}{\lambda} \cdot U_0 \cdot \sin\left(\frac{2 \cdot \pi \cdot x}{\lambda}\right) \sin\left(\omega \cdot t\right) \tag{5.5}$$

The maximum strain amplitude in the mid$-$section of the holder is given by: with

$$\varepsilon = \frac{2 \cdot \pi}{\lambda} \tag{5.6}$$

and the peak velocity at the end of the holder can be calculated with the equation 5.5 and 5.6:

$$\vartheta = \omega \cdot U_0 \tag{5.7}$$

ε strain distribution
U_0 displacement amplitude
λ wave length
ω angular frequency
ϑ peak velocity at the end of the holder
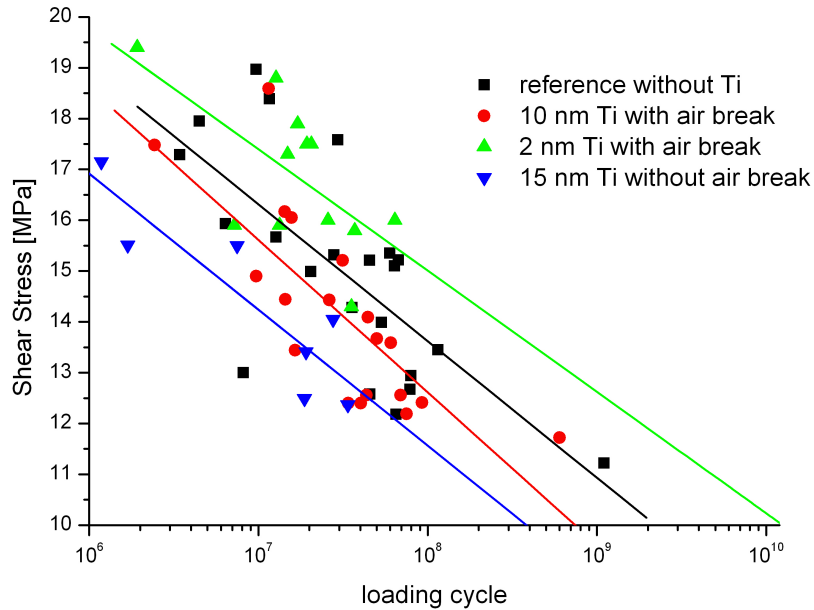
Figure 5.19: Fatigue life cures of 4 sample batches, showing calculated shear stress as a function of loading cycles

The results of the prior performed standard bond shear test were used to select the sample batches, which should be investigated by the fatigue life time test. Vibration−tests were performed on four different batches:

- reference without titanium

- 2 nm with air−break

- 10 nm with air−break

- 15 nm without air−break

Figure 5.19 shows the results of the fatigue life time tests. All data sets show a relatively high scatter of stress values. The data gained from the life time tests varied more than data from the shear stress, nevertheless the data distributions are distinguishable.

Data points were collected at higher displacement values (lower loading cycles 10^6) and at minor long-term loading − and therefore higher loading cycles (10^9) − from all sample batches. Noticeable differences in the life time of the different sample batches were observed:

Highest fatigue life time can be found in the test group with 2 nm Ti. The titanium−free reference samples are nearly comparable regarding life time extrapolation, while samples with 10 nm and more Ti (regardless whether air−break or not) bear significantly lower loading cycles (reduction by one decade). This investigation corresponds to shear test results (table 5.4 on page 54), which indicates that titanium contamination has an influence on wire bond quality: While thick layers of titanium ($> 10nm$) reduce the reliablity, thin layers ($< 2nm$) seem to enlage the endurance of bond interconnects.
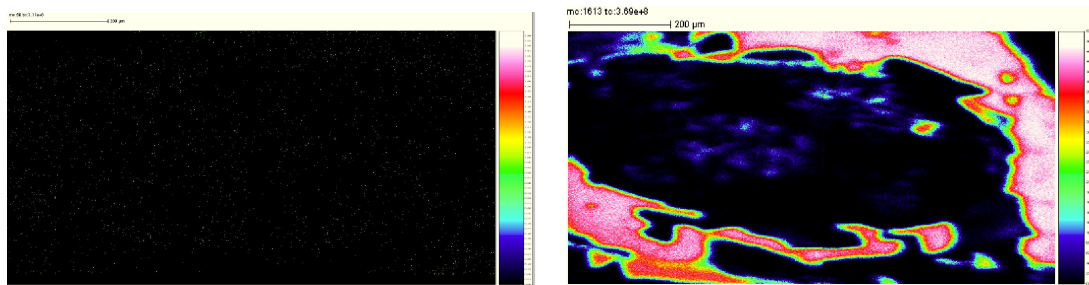
(a) ToF−SIMS image of the fracture area of a reference sample[3] (without breeded titanium contamination) after a life−time test

(b) ToF−SIMS image of the fracture area of sample # 7[3] (with 10 nm titanium with air−break) after a life−time test

Figure 5.20: ToF−SIMS images[39] of the fracture area after vibration tests, displaying the titanium distribution on the surface. Figure 5.20(a) (on the left side) showes no additional titanium signal on the surface. Samples with titanium contamination (figure 5.20(b) on the right side) show an enhanced titanium signal, which implies a wire bond failure due to interface separation.

A scanning electron microscope (**SEM**)[41] and a ToF−SIMS instrument were used to analyze the fracture surface after life time tests, in order to investigate the fracture mechanism during the fatigue process. In most instances SEM images indicate a wire bond failure due to interface fracture. A characteristic feature of fracture due to interface separation is a flat fracture area, which can be seen in all kind of samples (with & without titanium deposition).

ToF−SIMS images confirm the assumption of an interface failure:

Titanium was detected on the fracture surface of a sample with a breeded titanium layer (10 nm with air−break) after wire bond failure (figure 5.20(b)). This titanium on the fracture surface must have been located directly at the wirebond/device−interface, because samples with additional breeded titanium contamination contain only in the uppermost

---

[40]corresponding to SEM images of the wirebond and the device surface in section A.1, image 5.20(a) to figure A.2 & image 5.20(b) to figure A.5, respectively.

[41]figures in appendix A.1 on page 86

layers $(5 - 10 \; nm)$ a lot of titanium (figure 5.9(b) [42]).
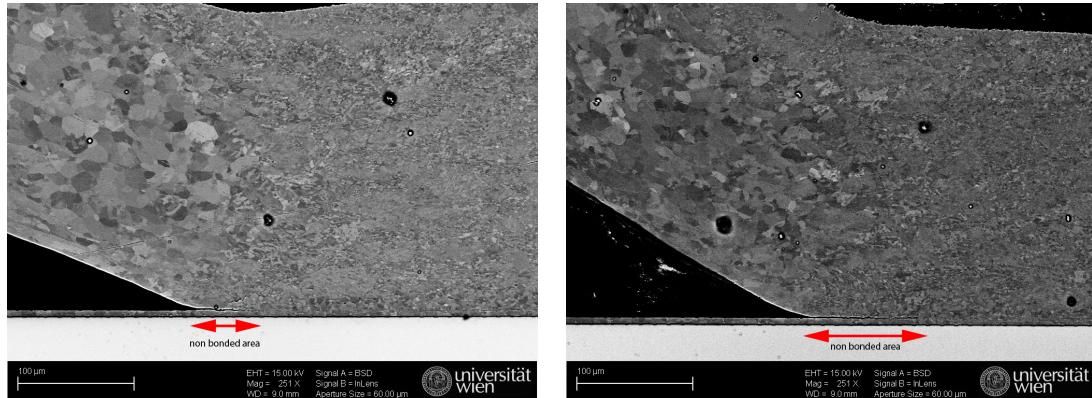
(a) Cross section of a reference sample[3] (without breeded titanium contamination) with wire bond before loading

(b) Cross section of sample # 7[3] (with 10 nm titanium with air−break) with wire bond before loading

Figure 5.21: Cross sections of a reference sample (figure 5.21(a), left side) & a sample with an additional titanium layer (figure 5.21(b), right side). Non−bonded areas are indicated by red arrows. Thick layers of titanium lead to a huge areas of reduced contact in comparison to samples without titanium.

Looking at the SEM images of the fracture surface (section A.1), one major difference between reference and contaminated samples can be observed:

The samples with thick titanium layers $(10 - 15 \; nm)$ show bigger and more flat surface regions (which indicate interface failures) than samples without titanium and samples with 2 nm Ti.

Fracture surfaces with areas of strong bonding (e.g. figure A.2[44]) can be related to data points of late wire bond failures, fracture surfaces with weak bonding areas to data points of early wire bond failures, respectively.

SEM images of cross sections showed increased "non bonded areas" for sample batches with thick titanium layers $(> 10 \; nm)$ compared to sample batches with thin layers of titanium $(< 2 \; nm)$ (figure 5.21 and appendix A.2, figure A.7[45]). This is probably due to oxide remants in the bonding area, because the ultrasonic energy or bonding time was not high enough during the bonding process to remove the thicker oxide layers.

The fracture mechanism of samples with thick Ti−layers is accelerated due to non−bonded areas and areas of reduced contact, which explains the reduced life−time of micro−joints

---

[42]on page 49

[44]section A.1

[45]on page 91

61

of such sample batches, while samples with 2 nm Ti show a enhanced fatigue life, bonding strength and more areas of strong bonding, hence thin titanium oxide layers increase the bonding quality.

6

Hydrogen Contamination

6.1 Introduction

The analysis of hydrogen is very important in many fields of material science, particular in semiconductor industry. Even small amounts of hydrogen can have a big impact on the physical, electrical and chemical properties of metals, semiconductors and insulators, and therefore on the whole semiconductor device [64, 65]. It also plays an important role in the negative bias temperature instability (NBTI) of MOS devices [66, 67]. Recent activities showed that the charge pumping (CP) current and the permanent threshold voltage (V_{TH}) shift is strongly influenced by the hydrogen concentration next to the GOX [68, 69]. Traces of hydrogen contamination can be a result of thin film preparation or on purpose by exposing the wafers to pure hydrogen or forming gas anneals [70]. Hydrogen incorporation can be a by−product of plasma−enhanced chemical vapor deposition (PECVD) of thin silicon nitride layers (SNIT). Such kind of layers contain a lot of hydrogen since their precursors are the respective hydrides and are therefore commonly known as a hydrogen source [71]. Hydrogen can diffuse to the gate oxide (GOX) during deposition of SNIT or afterwards during a following process step with a higher temperature budget. Hence it is crucial to monitor the hydrogen content in semiconductor devices by means of depth profiling. This chapter is devoted to the *"hydrogen hunt"* in semiconductor devices, especially:

- Determination of Relative Sensitivity Factors for Hydrogen in different materials and

- Investigations of the impact of several process steps on the hydrogen concentration next to the GOX

6.2 Determination of Relative Sensitivity Factors for Hydrogen in Si & $SiO_xN_yH_z - layers$

6.2.1 Introduction

It is still a challenging task to determine the atomic concentrations in thin films for material science. In particular, the measurement of hydrogen − with its very low mass − in the ppm to ppb range with a depth resolution in the nm regime [64]. Only a few measurement techniques are even capable to detect hydrogen, some of them are still not sensitive enough for the requirements in semiconductor industry (e.g. Elastic Recoil Detection Analysis (ERDA)) or do not fit to the given device parameter (e.g. lateral dimension of the area of interest of the samples) .

ToF−SIMS has the ablility to detect every element in the ppm − ppb range with a depth resolution in the nm range. Therefore it is the best method to determine the content of trace elements within a multilayer device. However, the quantification is difficult, due to:

- high background noise levels at low masses

- the need for standards in every single kind of layer and

- the lack of "appropriate" standards [1]

This section deals with the determination of RSFs for Si & $SiO_xN_yH_z - layers$.

6.2.2 Sample Preparation & measurement settings[2]

Thin films of amorphous PECVD silicon oxide ($a - SiO_xH_z$), amorphous PECVD silicon oxynitride ($a - SiO_xN_yH_z$) and amorphous PECVD silicon nitride ($a - SiN_yH_z$) were produced from gas mixtures of silane (SiH_4), nitrogen (N_2), nitrous oxide (N_2O) and ammonia (NH_3) using radio frequency assisted deposition at elevated temperature. All films were manufactured on eight inch ($\varnothing$ 200 mm) $\langle 100 \rangle$ silicon wafers, carrying a thermally grown silicon oxide (SiO_2) layer using an Applied Materials P5000 PECVD chamber. The

---

[1]itemization corresponding to literature [72]

[2]In co−operation with DI Dr. Kurt Matoy, Montanuniversity Leoben and DI Dr. Holger Schulze, Infineon Villach

samples were broken into several parts. One part was transferred to SIEMENS CT (Munich) to determine the film composition by means of **E**lastic **R**ecoil **D**etection (ERD) and **R**utherford **B**ackscattering **S**pectroscopy (RBS). $^4He-ions$ with energies of 2.4 MeV and 2.7 MeV were used for RBS and ERD, respectively. The scattering angles were 30° and 170° for RBS and ERD, respectively.

The other part of the samples was transferred to the *Institute of Chemical Technologies and Analytics* (Vienna, University of Technology) for ToF-SIMS analysis. All ToF-SIMS measurements were performed with a $ToF-SIMS^5$ instrument (ION−TOF GmbH, Münster, Germany), which is equipped with a Bi−LMIG (**L**iquid **M**etal **I**on **G**un) for primary ion emission and two sputter guns (O_2^+ & Cs^+) to etch the sample surface for depth profiling. The primary ion beam scanned randomly over an area of interest of 100×100 μm with a 128×128 raster, the emission current of the LMIG was set to 1 μA to get an appropriate target current ($\approx 1,6$ pA at 100 μs cycle time). The analysis was carried out in the *Dual Beam Mode* (section 2.1.4) with Bi_1^+ ions (energy 25 keV)[24]. Alternating, a second beam of Cs^+ ions ablated the sample surface, which increased the yield of negatively charged secondary ions (e.g. H^-, O^-, F^-) and allowed the measurement of CsM^+ cluster ions[3]. Sputtering was carried out on a 300×300 μm area with a target current of ≈ 160 nA. At the expense of depth resolution the energy of the Cs^+ ions was set to 2 keV. This was necessary in order to reduce the measurement time to an adequate level.

An additional charge compensation via a low energy electron food gun was performed, which is commonly used for insulators [18]. In order to provide a ground potential on the insulating samples, additional 40 nm thin $Au-$layers were deposited by means of Ar−plasma induced deposition onto the oxide and nitride thin films. With the aid of this conductive layer peak shifting in the mass spectrum can be reduced or avoided during ToF−SIMS measurements. All measurements were carried out in negative mode at a cylce time of 100 μs and a pause between the cycles of three seconds to ensure surface charge compensation.

---

[3]M for molecule of interesst (e.g. H, O, F)

Sample number	Implantation dose	annealing
1	$1E14/cm^2$	no annealing
2	$1E14/cm^2$	$400° \, C \, for \, 1 \, h$
3	$1E15/cm^2$	no annealing
4	$1E15/cm^2$	$400° \, C \, for \, 1 \, h$

Table 6.1: Proton−implanted samples with different process steps

Proton implantation was used for the determination of RSF for hydrogen in silicon. 300 keV protons (^1H) were implanted at room temperature into four float-zone silicon wafers with a dose of $1E14/cm^2$ and $1E15/cm^2$, respectively (table 6.1).

It is well−known that high proton doses ($\geq 10^{14} cm^2$) lead to a change of the resistivity of low−doped materials and that the resistivity increases with rising vacancy concentration (e.g. Si) [73]. Two wafers (one of each dose) were exposed to a post−annealing process at $400°C$ for one hour, to investigate the effect of postimplantation

Figure 6.1: Schematics of a SRP−measurement[4]

plantation annealing. All samples were analyzed via **S**preading **R**esistance **P**rofiling (SRP) and by ToF−SIMS. Measurement parameter were the same as for the $a-SiO_xN_yH_z$ layers, except the charge compensation and the additional Au−layer, because silicon is conductive.

6.2.3 Results and Discussion

The influence of an additional Au−layer on the insulating surface was investigated, in order to develop a proper measurement configuration for samples with low conductivity. Depth profiles were performed on several different spots on the sample surface.

---

[4]from a report of the SGS institute Fresenius GmbH reportnumber: 1155379 HLM08 145
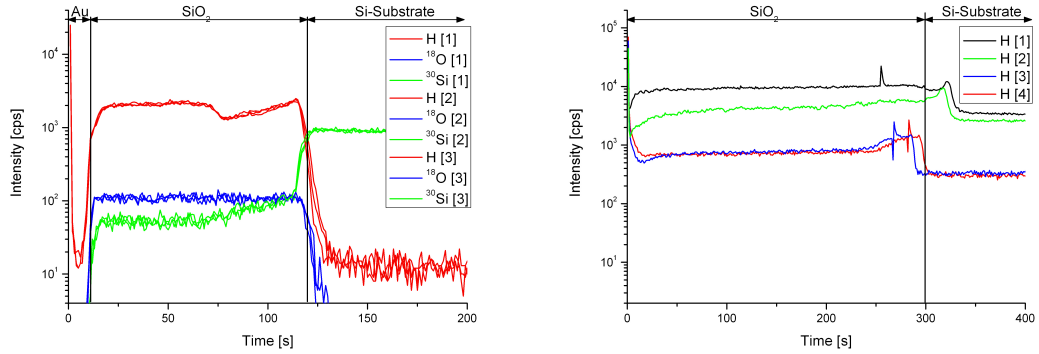
(a) Three ToF−SIMS measurements (1-3) of a SiO_2−layer with additional Au−layer on top. The Au−layer serves as a ground potential and therefore measurements are repeatable

(b) Four ToF−SIMS measurements (1-4) of a SiO_2−layer with standard charge compensation, which is not sufficient and leads to irreproducible results

Figure 6.2: Comparison of ToF−SIMS measurements with standard charge compensation (fig. 6.2(b)) and with additional Au−layer (fig. 6.2(a))

Figures 6.2(a) and 6.2(b) show the measurements with and without an additional Au−layer on top of the silicon oxide.

The standard charge compensation should neutralize the applied charge via an electron flood gun (e^- energy approx. 20 eV) between two excitation pulses. Even though the time between the pulses can be user−defined extended [24, 18], the charge compensation is not sufficient and leads to irreproducible results (figure 6.2(b)). The hydrogen content varies between one order of magnitude for four different measurements of the same sample.

If an appropriate charge compensation is not considered, the primary ion bombardment causes severe problems. It leads to sample charging with the following effects:

1. **Change of extraction energies:** spontaneous surfaces (dis−)charging prevents the adjustment of the secondary ion optics (e.g. reflectron voltage adjustment).

2. **Local field effects:** due to heterogeneous sample charging trajectories of the secondary ions are disturbed and the ions do not reach the detector. Hence the number of counted ions varies although the concentration in the sample is the same.

3. **Migration effects:** mobile ions (e.g. $H^\pm$, $Na^\pm$) migrate under the influence of local charges on the surface [5] [6]

---

[5] itemization corresponds to figure 6.3(a)
[6] itemization and figure from [18]

Moreover the sample charging leads to a peak−shift in the ToF−SIMS spectra, which can only be reduced by an additional conductive layer (figure 6.3(b)). The conductive layer acts as a ground potential, the applied charge discharges on the gold layer. Therefore the surface potential of the $200 - 400$ nm thick SiO_2 layers will remain unchanged during the measurement. An altered surface charge would build up an electric field in the SiO_2−layer and change the measurement settings. Due to the gold layer and an analyzer−reflectron voltage adjustment the above mentioned side effects are avoided, hence reproducible measurements are possible (figure 6.2(a)). A temperature reduction (down to $-130°C$), which would decrease the migration effects by reducing the ion mobility is − in that case − not necessary [60].
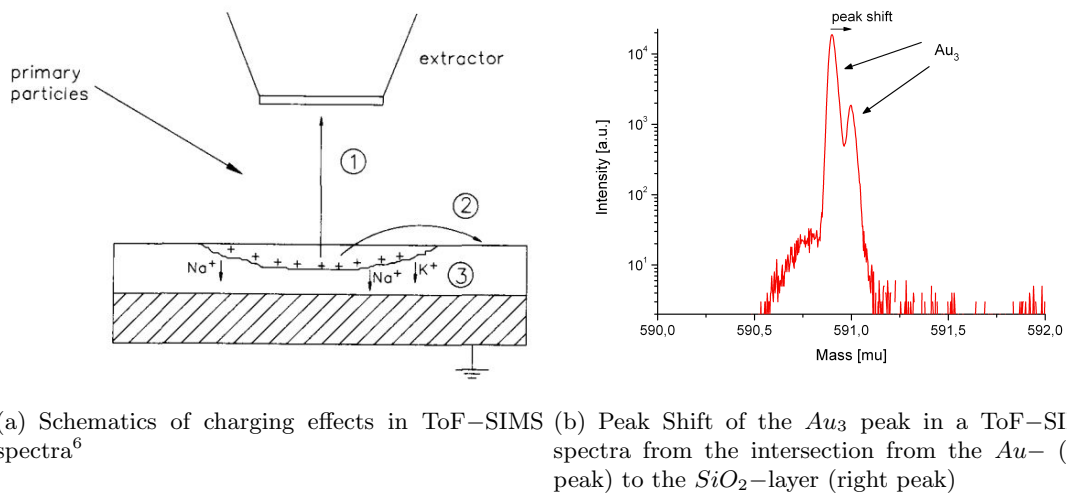
(a) Schematics of charging effects in ToF−SIMS spectra[6]

(b) Peak Shift of the Au_3 peak in a ToF−SIMS spectra from the intersection from the $Au-$ (left peak) to the SiO_2−layer (right peak)

Figure 6.3: Charging effects of in ToF−SIMS spectra: schematics (fig. 6.3(a)); a real ToF−SIMS spectrum (fig. 6.3(b))

Sputter deposited PECVD silicon oxide− $(a-SiO_xH_z)$, silicon oxynitride− $(a-SiO_xN_yH_z)$ and silicon nitride− $(a - SiN_yH_z)$ layers were investigated regarding their nitrogen, oxygen, hydrogen and silicon content by means of RBS, ERD and ToF−SIMS to determine the RSF for hydrogen in different matrices. ToF−SIMS measurements were performed with the prior determined parameter setup. SNIT showed the highest hydrogen content and SiOx the lowest concentration (Table 6.2).

Sample	Thickness [nm]	Material	$1E15at/cm^2$	N/Si	O/Si	H/Si
13	107	SiOx	738	0	1,89	$< 0,12$
14	210	SiOx	1402	0	1,94	$< 0,12$
15	194	SiOx	1280	0,14	1,25	0,32
12	198	SiON	1583	0,73	0,74	0,4
16	201	SiON	1390	0,29	0,93	0,41
17	238	SiON	1984	1,01	0,37	0,43
18	170	SiON	1465	0,96	0,57	0,47
19	191,2	SNIT	1695	1,1	0	0,34
20	201,1	SNIT	1770	1,17	0	0,34
21	207	SNIT	1844	1,29	0	0,3
22	415,8	SNIT	3469	0,89	0	0,27

Table 6.2: ERD and RBS measurement results

Proton−implanted silicon wafer were investigated by means of ToF−SIMS to determine the RSF for hydrogen in silicon. In order to control the implantation parameter, the hydrogen profile was simulated with SRIM software as well (The **S**topping and **R**ange of **I**ons in **M**atter) [74]. ToF−SIMS and SRIM show an approximate depth of the maximum hydrogen peak at 3 μm (6.4 & 6.5(a)), which indicates the correct process parameter during sample preparation.

The crater depth measurements were performed with a *DEKTAK 2* stylus profilometer (Veeco Instruments Inc) and contactless with a digital holography microscope *DHM 1000* (Lyncee Tec SA, 1015 Lausanne, Switzerland). Both measurements have been compared to simulated crater depth[7].
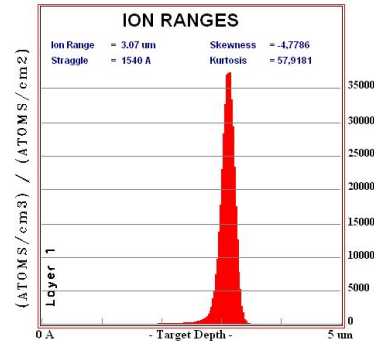
Figure 6.4: SRIM simulation of hydrogen profile with an implantation energy of 300 keV
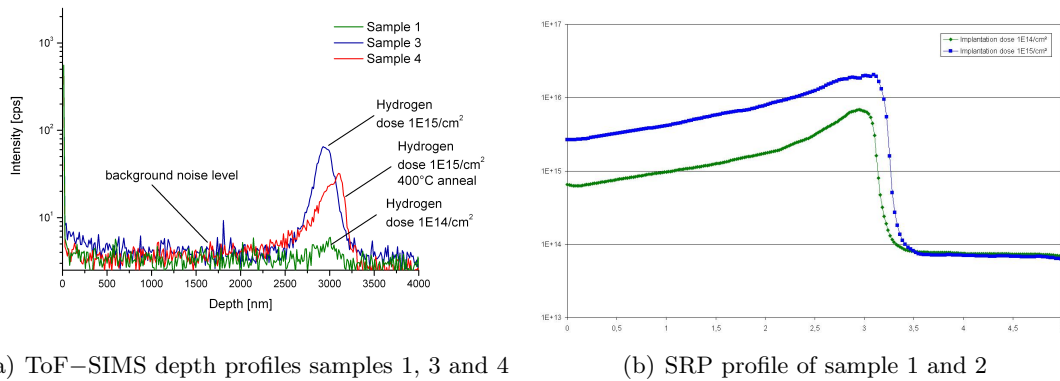
(a) ToF−SIMS depth profiles samples 1, 3 and 4   (b) SRP profile of sample 1 and 2

Figure 6.5: ToF−SIMS (fig. 6.5(a)) and SRP (fig. 6.5(b) measurement results

SRP and ToF−SIMS were used to detect the carrier concentration(in case of the SRP mesasurement electrically active). It was possible to measure the hydrogen distribution of both implantation doses ($1E14/cm^2$ & $1E15/cm^2$) with spreading resistance profiling. ToF−SIMS was not able to measure the hydrogen profile with an implantation dose of $1E14/cm^2$, the hydrogen signal disappeared in the back ground noise.

---

[7]calculated with software provided from IONTOF

In order to determine the RSF for hydrogen in SiO_2 the atomic concentrations of Si, O, H and N in the SiO_2−layer of sample # 15 were calculated based on the ERD and RBS results (Table 6.3). The determinated atomic concentration of hydrogen atoms was used for calculating the relative sensitivity factor in SiO_2.

N $[cm^{-3}]$	O $[cm^{-3}]$	H $[cm^{-3}]$	Si $[cm^{-3}]$
$6,6E+16$	$5,9E+17$	$1,5E+17$	$4,7E+17$

Table 6.3: Atomic concentration of sample # 15 based on the ERD and RBS data

The RSF for hydrogen in SiO_2 was calculated by integrating the H^- signal (I_H) in sample # 15 (Table 6.2), for hydrogen in Si by integrating the H^- signal in sample # 3 (Table 6.1), respectively. ^{30}Si was chosen as a reference matrix signal I_M, it's signal intensity is well below detection overflow and above the detection limit.

The RSF was in both cases calculated with the following formula:

$$RSF_{H,M} = \frac{J_H}{d} \cdot \frac{\int I_M}{\int I_H - \int I_{bg}} \tag{6.1}$$

$RSF_{H,M}$	Relative sensitivity factor for an element H in a matrix M
J_H	atom concentration of the element H in the sample
d	Depth [cm]
I_M	Secondary ion intensity of the measured isotope of the matrix M [ions / s]
I_H	Secondary ion intensity of the measured isotope of the element H [ions / s]
I_{bg}	background noise level of the element H in the matrix M [ions / s]

I_{bg} considers the background noise level of hydrogen in the matrix (see also figure 6.5(a)). In case of the silicon oxide layer it is set to zero, because ERD detects the whole hydrogen content in the investigated layers. The obtained RSF for hydrogen in SiO_2 : $RSF_{H,Si} = 4,08E+20 \ cm^{-3}$, for Si : $RSF_{H,Si} = 5,08E+21 \ cm^{-3}$. This result is close to the literature values if we take differences in the SIMS approach and chosen matrix signal into account [75, 76, 77].

6.3 Characterization of process induced variations of the hydrogen content next to the Gate Oxide[8]

Hydrogen can alter the quality characteristics of semiconductor devices. In particular, differences in the hydrogen budget close to the gate oxide influence physical and electrical properties of semiconductor devices.

This section addresses process induced variations of the hydrogen content next to the **gate oxide** (GOX).

Sample batches were electrical characterisated by **Charge Pumping** (CP) measurements[8] [9] and the hydrogen content was physically verified by **Time−of−Flight Secondary Ion Mass Spectrometry** (ToF−SIMS). The relative sensitivity factors of prior investigations were used to quantify the hydrogen signal from ToF−SIMS results of this section.

6.3.1 Sample preparation and measurement settings[10]

The hydrogen incorporation within the gate oxide was modified during **Back End of Line** (BEOL) fabrication by varying different process steps. The influences of various modifications were investigated:

Influence of the BEOL process: The influence of the BEOL process was compared with the standard *Metal 1* wafer process to check if the resolution and detection limit of the ToF−SIMS instrument is a suitable to identify minute differences in the hydrogen amount next to the GOX (approx. depth 3 μm) and to verify CP measurements. CP measurements can only estimate the charge carrier concentration by counting dangling bonds at the interface and not the "real" hydrogen budget.

Influence of pure hydrogen anneal: Nissan−Cohen described the possibility that hydrogen can be incorporated by exposing wafers during the BEOL process to a pure hydrogen or forming gas anneal [70]. ToF−SIMS measurements were performed to investigate the influence of a pure hydrogen anneal.

Influence of the variation of the titanium barrier thickness below the routing metallization:[11] Ti− layers are considered to be efficient hydrogen barriers [79]. Introduction of a

---

[8]Cooperating with Mag. Dr. Thomas Aichinger
[9]details in [78]
[10]Cooperating with Mag. Dr. Thomas Aichinger and Infineon Technologies Villach
[11]details in publication B.2

Ti−layer between the GOX and the SNIT layer − which is known to be a hydrogen source − and modification of the Ti thickness should vary the hydrogen concentration at the GOX [71].

The target current for the ToF−SIMS measurements was optimized according to standard procedures of the instrument manufacturer[12]. The energy of the eroding beam was varied for the different sample batches: Trading off depth resolution versus measurement time. Depth profiles were performed on large reference capacitors (approx. 1 mm^2). ToF−SIMS analysis was carried out on several different spots located in the vicinity of the electrically measured PMOS devices.

6.3.2 Results and Discussion

It has been reported that the permanent threshold voltage (VT_H) shift and the negative bias temperature instability (NBTI) depends on the hydrogen concentration close to the GOX. Hence, the influence of different process parameters (BEOL influence, effect of pure hydrogen annealing during BEOL processing and variation of hydrogen barrier thicknesses below the routing metallization) on the hydrogen incorporation within the GOX was investigated.

Influence of the BEOL process

For the characterization of the BEOL process, CP measurements were performed and SIMS depth profiles were carried out on two different sample batches:

- wafer with *BEOL std. process*

- wafer with *Metal 1 std. process*

The BEOL process consists of several (deposition) steps and the respective patterning. Some of the deposited layers are known to have a huge hydrogen budget (e.g. plasma−enhanced chemical vapor deposition of SNIT (silicon nitride) layers). Hydrogen may diffuse from such layers after deposition towards the GOX without a proper hydrogen diffusion barrier.

---

[12]IONTOF GmbH
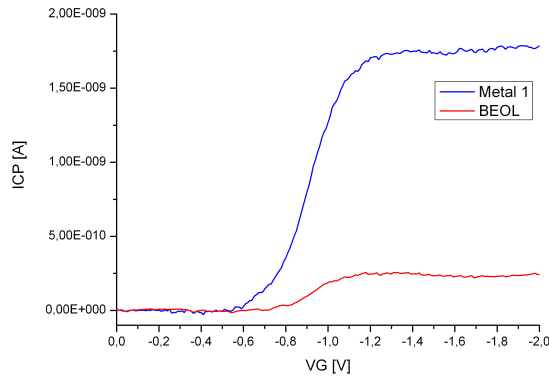
Figure 6.6: CP measurement of *Metal 1* (blue line) and *BEOL wafer* (red line). The CP signal of the *Metal 1 wafer* is much higher than the one of *BEOL wafer*. This is consistent with the assumption that the BEOL process leads to a more efficiently passivated interface by hydrogen than the Metal 1 process.

Figure 6.6 shows the CP measurements results of the *Metal 1* wafer and the *BEOL* wafer. The *BEOL wafer* has a lower CP signal and initially a larger number of positively charged defects, which corresponds to a high hydrogen concentration within the GOX. The ToF−SIMS results are in perfect agreement with the CP measurements (figure 6.7). The sample with the BEOL std. process has a significant higher hydrogen concentration within the whole stack. The *BEOL wafer* has got a larger amount of deposition processes of layers containing hydrogen and therefore more hydrogen within the GOX. Both methods verify that the hydrogen concentration is significantly increasing due to the BEOL process.
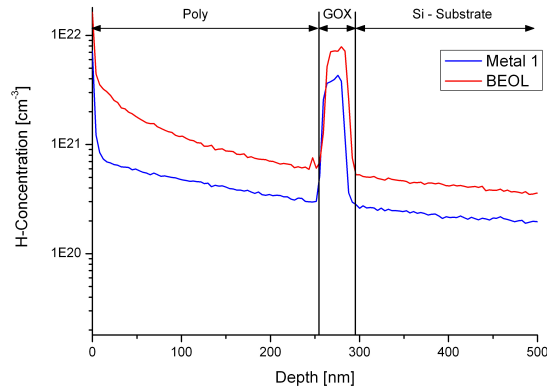
Figure 6.7: ToF−SIMS profile of two different processed wafers (BEOL std. process red line; Metal 1 process blue line). The BEOL process leads to a higher hydrogen concentration within the Poly, the GOX and the Si−substrate in comparison to the Metal 1 process. Note that the ToF−SIMS measurements show to clearly distinguishable graphs for the two different processed samples. Hence ToF−SIMS is suitable to verify the CP measurement results. For the orientation within the device the names of the different layers have been assigned.

Influence of pure hydrogen anneal

annealing 900° C	no annealing	wet GOX	dry GOX
wafer 1, wafer 2	wafer 3, wafer 7	wafer 2, wafer 7	wafer 1, wafer 3

Table 6.4: Sample preparation of the pure hydrogen anneal sample batch

Beneath the effect of pure hydrogen annealing during the BEOL process, the influence of different processed gate oxides was investigated. Therefore a sample batch of four electrically active wafers for CP measurements, and four wafers for ToF−SIMS analysis with a reduced stack size but the identical annealing and GOX processes (details of the sample preparation in table 6.4).
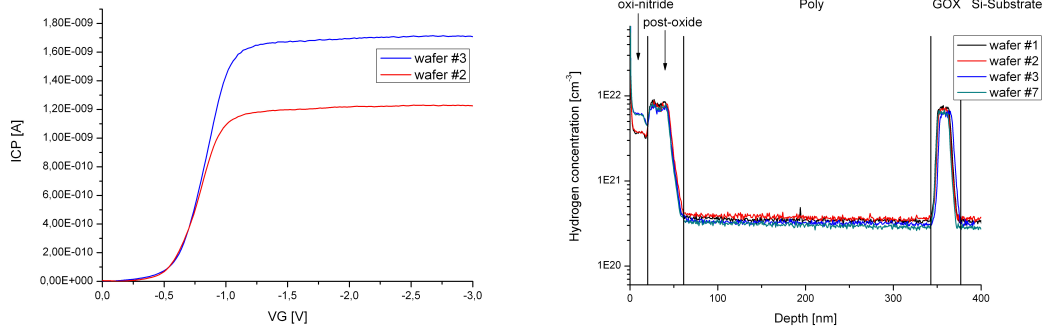
(a) CP measurement of wafer 2 and 3 [13]

(b) ToF−SIMS depth profile of the pure hydrogen anneal split wafers 1, 2, 3, 7[13]

Figure 6.8: CP and ToF−SIMS image of the pure hydrogen annealing sample batch. Figure 6.8(a) shows that wafer 3 has a slightly higher charge pumping current than wafer 2, which would support the assumption that wafer 2 has a higher hydrogen concentration within the GOX. Compared to the difference between the BEOL and the Metal 1 wafer (figure 6.6), this difference is negligible. ToF−SIMS shows nearly no difference in the hydrogen content at all.

Figure 6.8 shows the CP and ToF−SIMS measurements of the *pure annealing split sample wafers.* Unfortunately two of the electrically active wafers were destroyed during manufacturing (wafers 1 & 7) and could not be processed twice owing to capacity bottlenecks at the high temperature annealing process within the production line, therefore CP measurements can not distinguish between the effect of the GOX process and the post−annealing. Wafer 2 has a reduced CP current compared to wafer 3, which implies that the *wet oxidation* and the *pure hydrogen annealing process* increase the hydrogen content within the GOX.

The hydrogen distribution of the device stack is displayed in the ToF−SIMS image (figure 6.8(b)). Wafer 1 shows the same hydrogen distribution as wafer 2, while wafer 3 & 7 are comparable. Hence, it can be estimated that the two differently produced gate oxides (wet & dry) do not lead to a change in the hydrogen formation.

Wafer 3 and 7 showed a lower hydrogen concentration within the oxi−nitride but a higher concentration within the post−oxide, poly and gate oxide than wafer 1 and 2. Hydrogen is pushed from the oxi−nitride towards the gate oxide. This can directly be related to the influence of pure hydrogen annealing. Although pure hydrogen annealing at high temperatures during the BEOL processing pushes hydrogen towards the GOX, the effect

---

[13]sample number corresponding to table 6.4

of additional deposited layers is stronger (comparing the difference of the Metal 1 and BEOL processing (figures 6.6 and 6.7) with the difference of wafers with & without pure hydrogen annealing (figure 6.8)). In order to produce wafers with significant differences in hydrogen concentration within the gate oxide, it is preferable to deposit additional, hydrogen containing layers instead of temperature treatment with molecular hydrogen.

Influence of the variation of the titanium barrier thickness below the routing metallization[14]

Literature shows different possibilities to control hydrogen incorporation and NBTI performance within a semiconductor device:

- via an additional (high) temperature annealing step during BEOL processing [70, 80]

- by introducing thin layers with high hydrogen content [71, 81]

- by introducing barrier layers between the gate oxide and the routing metallization [79, 82].

The influence of the first two options has been discussed above. A new wafer split was manufactured to check the influence of barrier layers on the hydrogen distribtion within the semiconductor device:

Additional PVD titanium liners between the upper SNIT layer and the gate oxide were used to investigate the hydrogen diffusion towards the GOX. In order to control the hydrogen concentration within the gate oxide the thickness of the diffusion barriers was modified (sample preparation in table 6.5).

wafer 1	wafer 2	wafer 3
05/40 nm Ti/TiN	40/40 nm Ti/TiN	80/40 nm Ti/TiN

Table 6.5: Variation of the Titanium barrier thickness within the Ti/TiN sample batch. The rest of the device stack was processed identically for all three kinds of wafers

The samples (for both the CP and ToF−SIMS measurements) were processed identically, except for the Ti−layer thickness. The samples were not exposed to a chemical etching in order to prevent changes in the original hydrogen distribution. Therefore −at the expense

---

[14]results published at the IRPS 2010, article in appendix B.2

of depth resolution− the ablating sputter beam of the ToF−SIMS instrument was set to the highest energy $(2\ keV)$ to remove the thick device stack $(3.5\ \mu m)$ above the gate oxide within a resonable time interval.
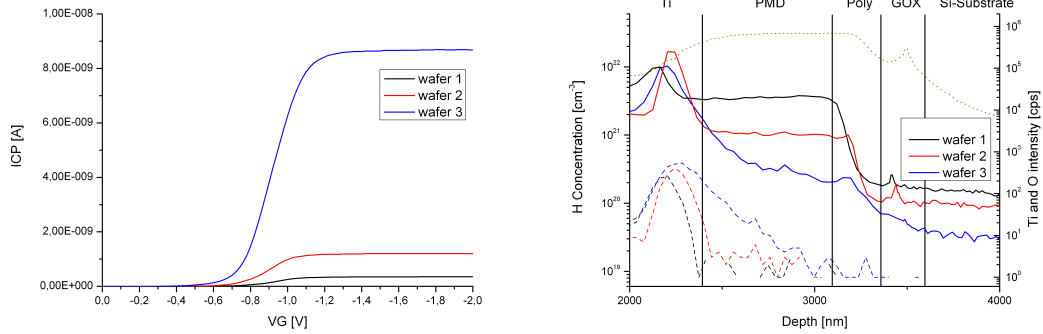
(a) CP measurement of wafer $1-3$ [16]. Wafer 3 shows the highest initial CP current, which indicates the highest hydrogen concentration next to the GOX.

(b) ToF−SIMS depth profile of the Ti barrier split wafers $1-3$[16]. The oxygen, titanium and hydrogen signal of the sub−metal BEOL stack are displayed for better orientation. The variation of the titanium layer thickness changes the hydrogen distribution within the post metal dielectric (PMD), the gate−poly and the gate oxide.

Figure 6.9: CP and ToF−SIMS image of the Ti barrier sample batch. Significant differences in the CP current and the hydrogen distribution were measured. The hydrogen concentration within the GOX is decreasing with the titanium barrier thickness. Hence. the wafer with the thinnest titanium layer has the most efficiently passivated interface, initially less positively charged defects and the lowest CP signal.

The CP measurements show a significant difference in the carrier concentration, the ToF−SIMS measurements in the hydrogen content next to the gate oxide, respectively (figure 6.9). The modification of the hydrogen distribution can directly be related to the titanium layer thickness. It is described in literature that titanium liners can affect the hydrogen distribution within a device stack [79, 82]:

The titanium layer can getter hydrogen from the SNIT layer. The absorbed hydrogen is trapped in the titanium layer, hence the hydrogen diffusion from the silicon nitride layer towards the gate oxide is hindered. With increasing barrier thickness less hydrogen can diffuse towards the gate oxide. This is in perfect agreement with the assumption from the gained CP current results: Less hydrogen within the GOX leads to more positively charged defects and therefore the a higher CP signal. The ToF−SIMS results are consistent with

---

[16]sample number corresponding to table 6.5

the assumption from the CP current measurements. It is possible to vary and control the hydrogen content next to the gate oxide by inserting an additional titanium barrier layer below the routing metallization and by variation of the barrier thickness.

Conclusion

7
Summary and Conclusion

Even at very low levels contaminations may lead to device and product failures. High−tech products − especially in semiconductor industry − need contamination monitoring for optimal product performance and reliability.

ToF−SIMS is a useful tool for various analytical tasks in failure analysis. It can provide a wide range of information to determine failures, if it is used considering its specific capabilities. Combined with additional information from complementary methods (AES, RBS, ERD, EM, AFM, LM) its contribution can be a major step towards clarification of contamination driven failure mechanisms.

In this thesis the advantages of ToF−SIMS were used to characterize contaminations on semiconductor surfaces and within thin layer systems. It is structured into successive work phases.

Within the first phase[1], metal oxide semiconductors were analyzed by means of ToF−SIMS and AES after different process steps in order to allocate present contaminations to their sources and/or manufacturing steps. Results presented in the first phase reveal organic, metallic, halogen and hydrogen contamination. All these contaminations can be investigated by means of ToF−SIMS although each problem needs a specific instrument adjustment and signal optimization. Therefore each problem is examined in a seperate chapter.

---

[1]details in section 3

The second phase deals with volatile organic contaminations originating from environment and/or transportation. ToF−SIMS and GC−MS were used to identify and characterize molecular contaminations. For the identification of unknown molecules in the outermost monolayer, high detection sensitivity, in combination with an analytical setup to reduce fragmentation and second order reactions in the mass analyzer is required. Experiments showed the possibilities and the limits of ToF−SIMS without additional cooling stage for surface chemical analysis.

In the third phase[2], titanium contamination was breeded onto bond pad surfaces of a non−planarized low voltage n−channel MOSFeT device to characterize its influence on bond wire reliability (titanium contamination was found in previous studies (section 3).

In addition to ToF−SIMS measurements the sample system was investigated by means of SEM (fracture areas wrecked devices as well as cross sections) and AFM (devices prior wire bonding). The self−passivating mechanism of the − in the metallization used − aluminium alloys and the influence of an "air−break" on the titanium formation within the device were investigated before mechanical tests (pull−, shear− and vibration− tests) were used to analyze the influence of the breeded titanium layers on wire−bond reliablity. A clear correlation between titanium layer thickness and wire−bond failure was found by complementary methods: While thick layers ($>$ 10 nm) of titanium decrease, thin layers ($<$ 2 nm) seem to enhance the wire−bond reliability, respectively.

Hydrogen can have an severe impact on physical, electrical and chemical properties of semiconductor devices, hence the fourth phase[3] is devoted to the "hydrogen hunt". Variation in the hydrogen content next to the gate oxide strongly influences the charge pumping current and the permanent threshold voltage (VT_H) shift.

In the present thesis the RSF of hydrogen in different semiconductor relevant materials and the effect of several manufacturing steps on the hydrogen concentration next to the GOX were determined.

The impact of the Back End of Line process, of pure hydrogen annealing during the BEOL process and the variation of the titanium barrier thickness below the routing metallization on the hydrogen content within the GOX were investigated and discussed. Revealing a strong dependence of the hydrogen formation within the device on additional deposited layers but only a small on additional pure hydrogen annealing steps, respectively.

---

[2]details in section 5 and publication B.1
[3]details in section 6 and publication B.2

Summarizing, within the scope of this work several contaminations of semiconductor devices have been analyzed, allocated to their sources and their influence has been characterized. The excellent analytical abilities and also the limits of SIMS in semiconductor industry have been demonstrated. The results and findings within this thesis give rise to the conclusion that the use of physical analytical methods for contamination monitoring and failure analysis is necessary for optimal product reliability.

Appendix

A

Additional figures

A.1 SEM images of fracture areas of titanium contaminated bond pads and corresponding wire bond surface
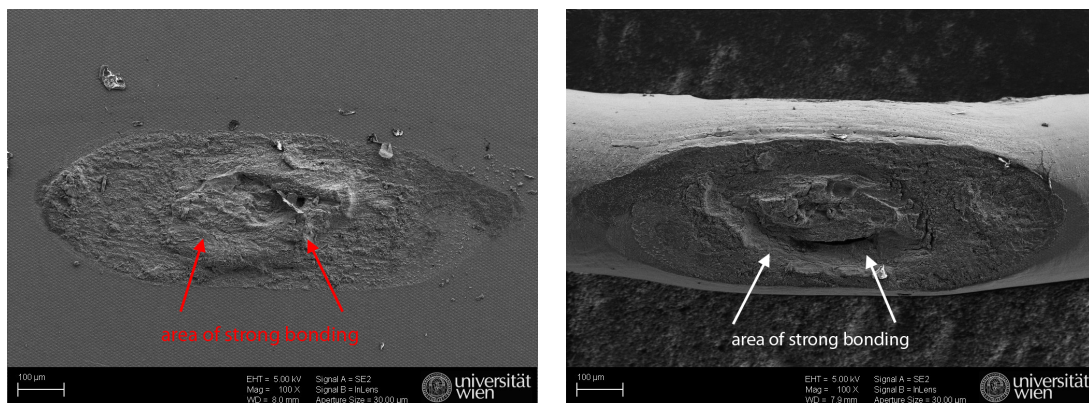
(a) Typical fracture area on the device surface after a vibration text

(b) Typical fracture area on the wire bond after a vibration test

Figure A.1: Fracture areas of sample batch 1[1](without any additional breeded titanium contamination) after a life time test

_____

[1]corresponding to sample description & preparation in table 5.1 in chapter 5 on page 41
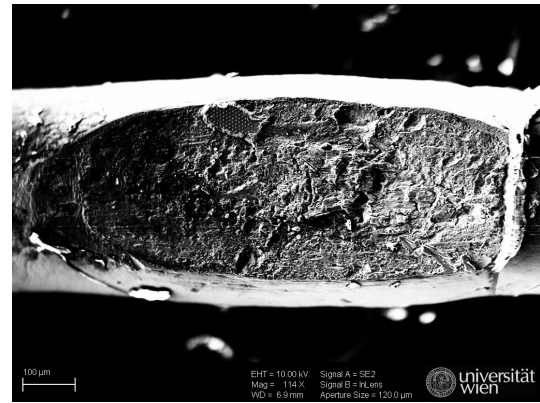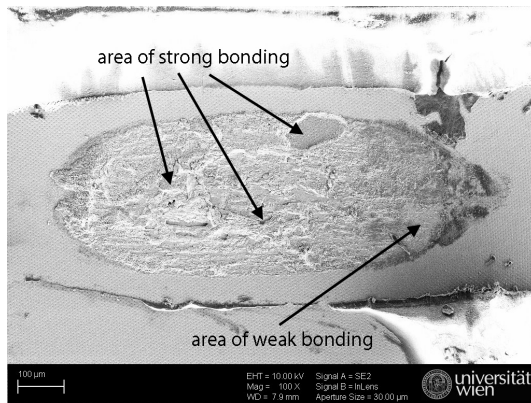
(a) Typical fracture area on the device surface after a vibration text

(b) Typical fracture area on the wire bond after a vibration test
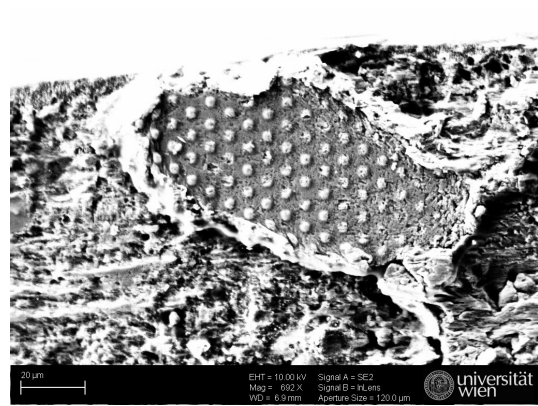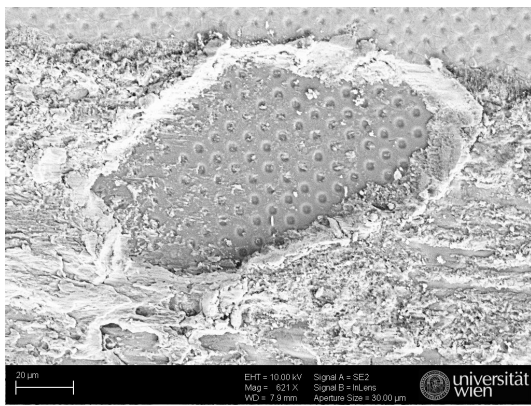
(c) Zoom of figure A.2(a) on a strong bonded area, chip side

(d) Zoom of figure A.2(a) on a strong bonded area, bond side

Figure A.2: Fracture areas of sample batch 1^2(without any additional breeded titanium contamination) after a life time test. The whole metallization stuck to the wire in the area of strong bonding (figures A.2(c) & A.2(d)).

_____

[2]corresponding to sample description & preparation in table 5.1 in chapter 5 on page 41
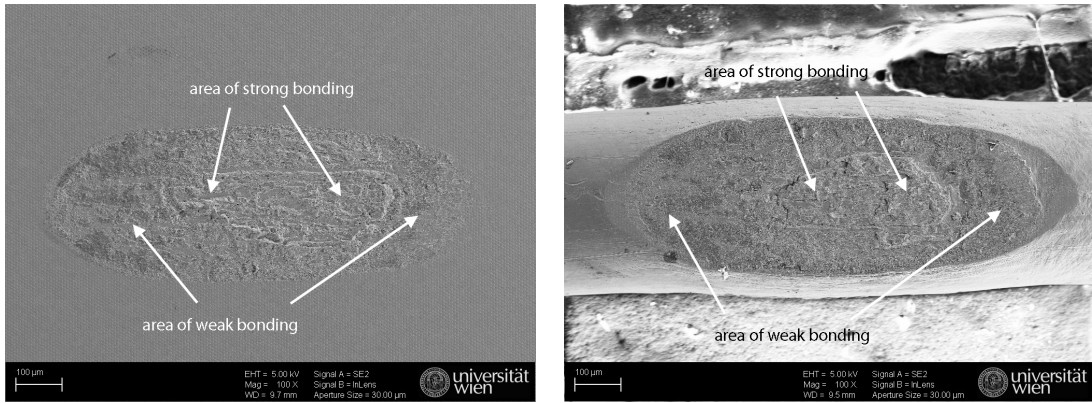
(a) Typical fracture area on the device surface after a vibration text

(b) Typical fracture area on the wire bond after a vibration test

Figure A.3: Fracture areas of sample batch 1^2 after a life time test
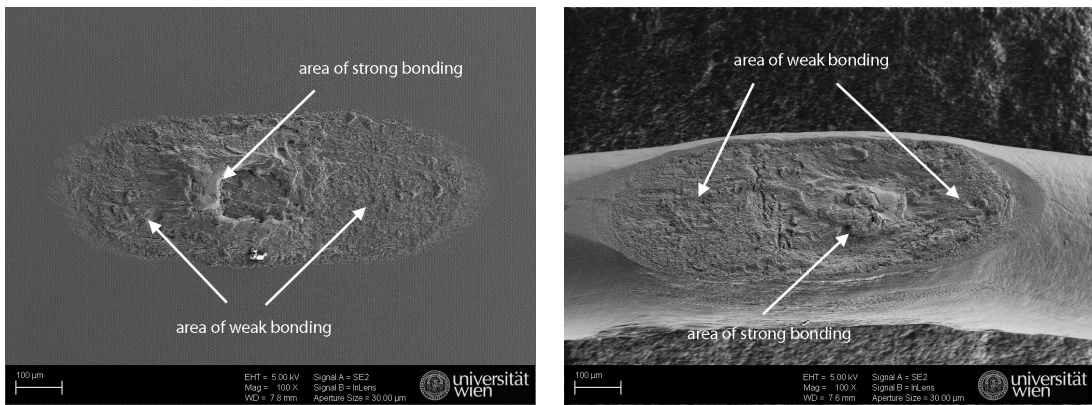
(a) Typical fracture area on the device surface after a vibration text

(b) Typical fracture area on the wire bond after a vibration test
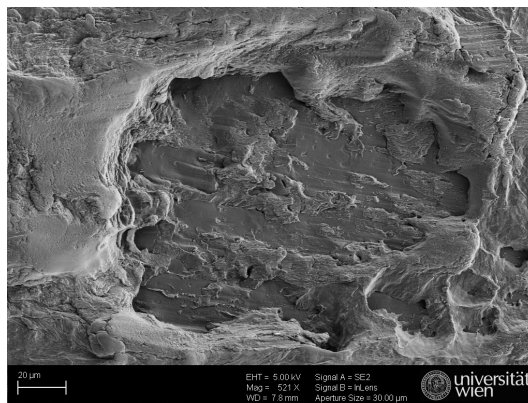
(c) Zoom of figure A.4(a) onto a strong bonded area

Figure A.4: Fracture areas of sample batch 7^2 (10 nm with air−break) after a life time test. In general sample batches with thick titanium layers show bigger weak bonding areas in comparison to sample batches without titanium.
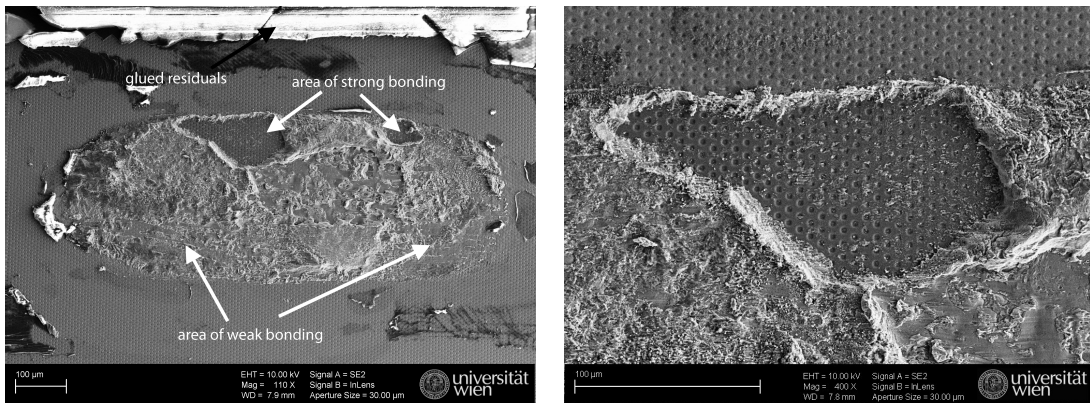
(a) Typical fracture area on the device surface after a vibration text

(b) Zoom of figure A.5(a) onto a strong bonded area
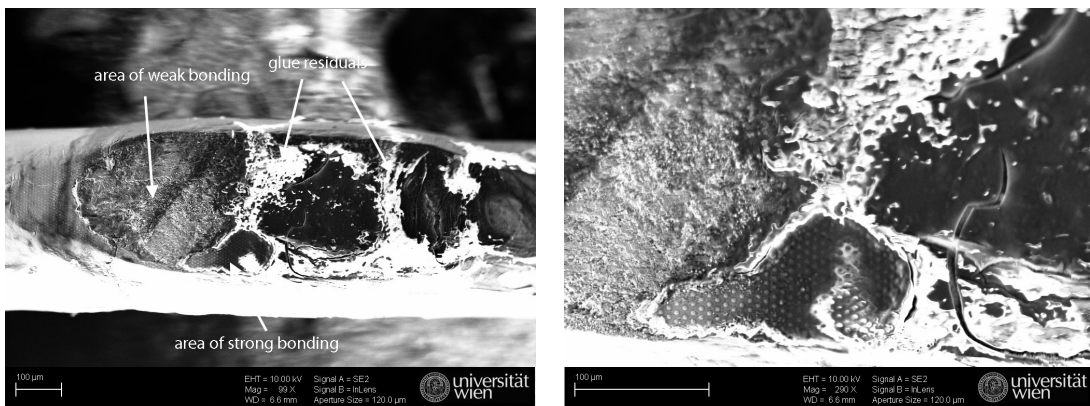
(c) Typical fracture area on the wire bond after a vibration test

(d) Zoom of figure A.5(c) onto a strong bonded area with additional residual glue.

Figure A.5: Fracture areas of sample batch 7^2 (10 nm with air−break) after a life time test. The glued areas can lead to outliers in the vibration test results, due to reduced shear force on the wire bond interface. In other words they can lead to wrong results with higher life−time than expected.
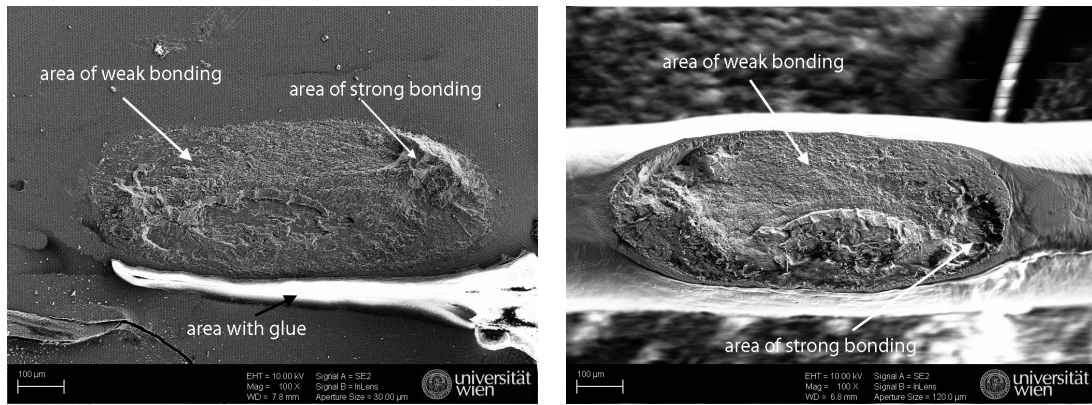
(a) Typical fracture area on the device surface after a vibration text

(b) Typical fracture area on the wire bond after a vibration test

Figure A.6: Fracture areas of sample batch number 7^2 (10 nm with air−break) after a life time test. Arrows show the areas of weak & strong bonding. The glued areas can lead to outliers in the vibration test results, due to reduced shear force on the wire bond interface.

A.2 SEM images of cross sections of wire bonded titanium contaminated devices
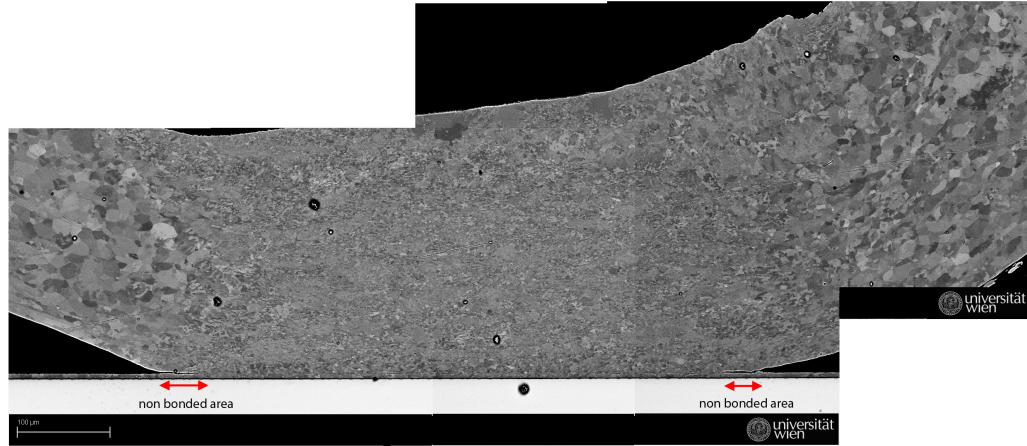
(a) Cross section of reference sample[3] without breeded titanium contamination
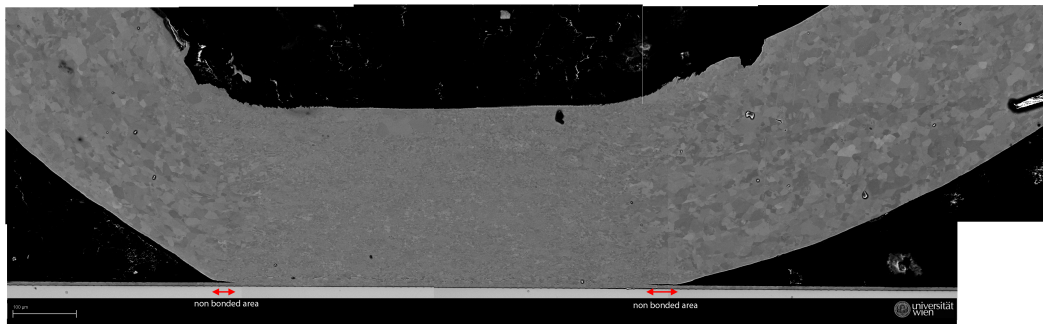
(b) Cross section of sample batch # 5^3 (with 6 nm titanium with air−break)
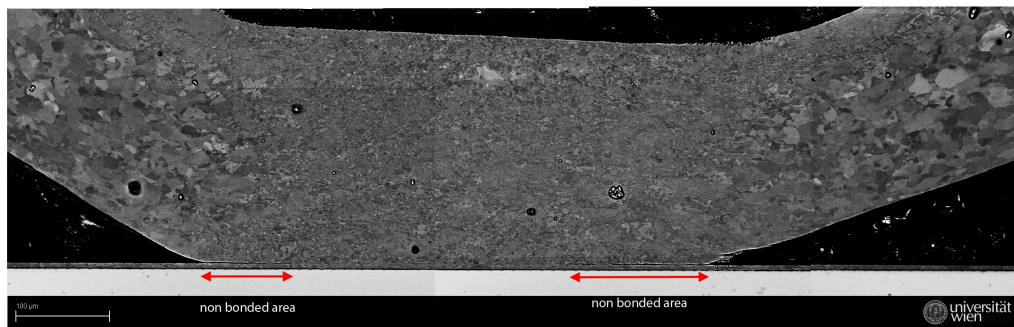
(c) Cross section of sample batch # 7^3 (with 10 nm titanium with air−break)

Figure A.7: Cross sections of unstressed (apart from sample preparation) samples with breeded titanium contamination (0, 6 & 10 nm Ti). Crack initiation starts at every sample at the wirebond−device interface. The reference sample and the sample with 6 nm titanium show nearly identical lengths of the non−bonded areas, only the sample with 10 nm titanium shows a bigger non−bonded area.

---

[3] corresponding to table 5.1 on page 41

B

Published Articles

B.1 Publication 1

S. Puchner, A. Zechmann, Th. Detzel and H. Hutter

Titanium layers on aluminum bond pads: Characterisation of thin layers on rough substrates

Surf. Interface Anal. 2010

Titanium layers on aluminum bond pads: Characterisation of thin layers on rough substrates†

S. Puchner,[a,b] A. Zechmann,[a] Th. Detzel[c] and H. Hutter[b]*

A big challenge in the semiconductor industry is to control surface contamination, especially on bond pads, since they might take influence on bond wire adhesion and reliability behavior. The impact of fluorine and organic contamination on wire bonding is already well documented.[1] Nevertheless, the influence of metal contamination has not yet been investigated in detail.

As titanium contamination has been found on bond pad surfaces, owing to some manufacturing process steps, this presentation concerns preliminary investigations on titanium-contaminated aluminum structures.

Titanium layers of different thicknesses in the nanometer range have been deposited by means of physical vapor deposition, either directly after aluminum deposition, or after an air break, in order to study their influence on wire bond quality in a systematic manner.

Depth profile measurements have been carried out by means of TOF-SIMS. In order to study the oxide and the titanium distribution, those measurements have been performed in positive and negative modes.

To overcome the big challenge to distinguish between the thicknesses of thin layers in the nanometer scale, depth profiling parameters were optimized regarding signal intensities.

This work deals with our analytical results and shows the possibility to clearly identify nanoscale layers and interdiffusion areas between different materials by enhanced depth resolution. In the near future, we will quantitatively investigate the impact of different titanium contaminations on bond pads on the adherence of Al-wedge bonds. Copyright © 2010 John Wiley & Sons, Ltd.

Keywords: TOF SIMS; aluminium bond pads; contamination

Introduction

Even low levels, contaminations on bond pads might influence device reliability and assembly processes of semiconductor devices, therefore, they need to be controlled for optimum product performance.

Krueger *et al*. described the effect of fluorine on the reliability of gate oxides.[2]

Halogen contamination on aluminum bond pads can lead to discoloration and weak wire bonds because of irritation of the intermetallic phase formation, corrosion and increased oxide growth.[1] The influence of organic contamination and different quantitative detection methods are also well described in the literature.[3] Nevertheless, the impact of metal contamination is not well investigated yet.

This work deals with titanium contamination on rough bond pads, as titanium contaminations have been found on bond pad surfaces owing to manufacturing processes. This contamination corresponds to titanocene, which is used as a radical starter in a certain polyimide resin.

Owing to its high sensitivity, quantification accuracy and good depth resolution, TOF-SIMS has the potential to detect contaminations at low levels and is therefore often used for failure analysis in semiconductor industry.[4] The aim of this work reported here was to investigate the oxide formation and titanium distribution on aluminum bond pads, and distinguish between different titanium thicknesses.

Vandervorst described which fundamental SIMS mechanisms contribute to quantification depth-scale errors and depth resolution, and how depth resolution can be enhanced.[5]

On aluminum bond pads, depth resolution of SIMS profiles is decreased due to surface roughness. Therefore, the erosion rate has been reduced by lowering the sputter energy.

Experimental

Sample preparation

All samples are based on the structure of a nonplanarized low voltage n-channel MOSFeT device with a 5 µm AlSi(1)Cu(0.5) metallization. The surface topography, dependent on the pattern

Table 1. Sample descriptions, preparations and surface micro roughness measurements

Sample	Sample preparation	R_q [nm]	R_a [nm]
Sample 1	No titanium deposition	14.4	11.7
Sample 2	2 nm without air break	17.3	14.1
Sample 3	2 nm with air break	13.7	10.0
Sample 4	6 nm without air break	21.8	18.1
Sample 5	6 nm with air break	17.3	13.7
Sample 6	10 nm without air break	25.3	20.3
Sample 7	10 nm with air break	19.5/(18.2)[a]	15.0/(14.1)[a]

[a] measurements in TOF-SIMS crater.

below is about 0.5 μm with an additional Al roughness of some 100 nm. Additional titanium layers of different thicknesses (0, 2, 6 and 10 nm) have been deposited either directly after aluminum sputtering, or after an air break (Table 1). The samples with air break have been kept out of the vacuum chamber for some minutes at ambient atmosphere.

The substrate temperature during aluminum sputtering was not actively controlled. For the duration of 5 μm Al sputtering, the substrate temperature raises from a starting level of 80 °C to approximate 300 °C. Ti deposition happened at constant 200 °C.

TOF-SIMS measurements

TOF-SIMS measurements were performed on a TOF.SIMS[5] (ION-TOF GmbH, Münster, Germany) instrument. This device is equipped with a liquid metal ion gun (LMIG) to analyze the surface of the sample, two sputter guns (O_2^+ and Cs^+) in order to erode the sample surface.

Depth profiling was performed in dual-beam mode[6,7] using a high energy analysis beam (25 keV) for a good lateral resolution and a very low current ($\sim$1 pA) to avoid surface irritation during the measurement. The beam for material abrasion is a low energy beam (0.25–2 keV) in order to increase the depth resolution. The ion beams hit the target with an angle of 45°, which is favorable to minimize sample roughening.

Primary ions–from the Bi_{1-7}^+ ion cluster source (LMIG)–are accelerated onto the sample surface and generate secondary ions, which are analyzed via a time-of-flight mass spectrometer. Alternating with the Bi_n^+ ($n = 1$–7) beam, a second beam, either of O_2^+ particles generated by an electron ionization impact source, or Cs^+ particles generated by a thermal ionization source is applied to ablate the surface.

The O_2^+ gun is used for enhanced positive ion detection, and the Cs^+ gun for enhanced negative ion detection, respectively. In our case, the O_2^+ gun has been used to determine the distribution of aluminum and titanium and the Cs^+ gun, respectively, to characterize the oxides.

All measurements have been performed in the high current bunched mode for enhanced mass resolution (lateral resolution 4 μm, mass resolution at 29 u more than 10 500 full width at half maximum) with a Bi_1^+ beam (25 keV energy, 128 × 128 pixels) focused onto a 99.6 × 99.6 μm^2 area.

The pulse width of the primary ion beam has been reduced to 2 ns for O_2^+ sputtering and 3.9 ns for Cs^+ sputtering, respectively. These parameters have been chosen in order to get a better resolution for the titanium and aluminum signal at the oxide interfaces. Additional measurements at a pulse width of 19.9 ns

have been performed for comparison. The energy of the sputter ions has been set to 500 eV for high depth resolution.[8,9]

In order to avoid crater side effect, the area for the removal of the surface was 300 × 300 μm^2 and all sputter guns were centered at the same point.

For surface roughness measurements, a MultiMode V scanning probe microscope from Veeco was used. Measurements were taken on the undisturbed sample surface and in the middle of one sputter crater on a 3 × 3 μm^2 area each. The root mean squared

formula 1

$$R_q = \sqrt{\frac{1}{n} \cdot \sum_i^n y_i^2} \qquad (1)$$

and the arithmetic average of the absolute values

formula 2

$$R_a = \frac{1}{n} \cdot \sum_{i=1}^n |y_i| \qquad (2)$$

with y_i as the vertical distance from the mean line at the ith data point were calculated.

Contactless crater depth measurements were performed on a digital holography microscope DHM 1000 (Lyncee Tec SA, 1015 Lausanne, Switzerland). The findings of the contactless depth measurements have been compared to simulated, as well as to profilometer depth measurements, performed with a DekTak 6 stylus profilometer (Veeco Instruments Inc.). All investigated methods show comparable results.

Results and Discussion

Characterization of the surface topography and impact of the ambient atmosphere on the sample surface

In order to study the effect of surface roughening during SIMS analysis, the surface roughness on a 3 × 3 μm area has been determined by atomic force microscopy (AFM). Owing to the topography of the polysilicon below the metallization, it was not possible to measure the surface microroughness in a bigger area. The values for R_a and R_q varied between 10 and 25 nm. Roughness values are typical for sputtered AlSiCu layers with that kind of pattern and thicknesses. Surface roughening by angular, low energy beams can be a major problem for high depth resolution SIMS analysis. Initial microroughness measurement on the sample surface and in the TOF-SIMS crater showed nearly identical values (Table 1). In this work, the additional roughening induced by the sputter beam during SIMS analysis is negligible.

Figure 1 shows the TOF-SIMS profiles of samples 3, 5 and 7 measured in positive mode. Native oxidation of the titanium slightly increases the thicknesses of the deposited layers. The effective thickness of samples 3, 5 and 7 are about 3, 8 and 12 nm, respectively. Reduction of the sputter energy to 500 eV enables a clear determination of the different thicknesses.

Figure 2 shows the TOF-SIMS profile of the reference (sample 1), without any titanium deposition measured in negative mode. It demonstrates the typical, self-passivating oxide formation of aluminum alloys after contact with oxygen. The oxide layer has an approximate thickness of 6 nm.
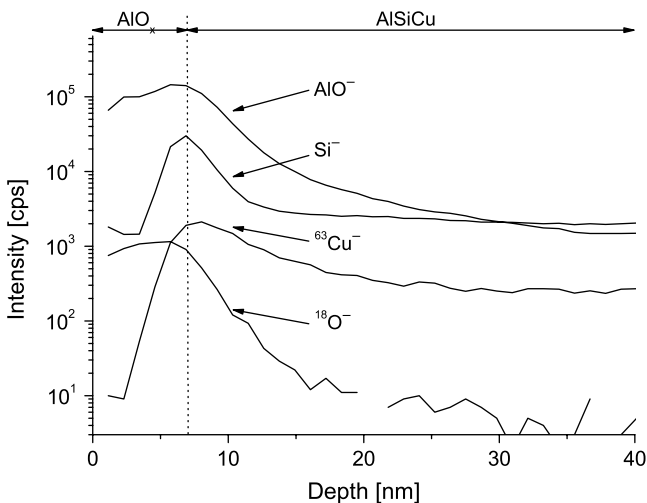
After deposition of the AlSiCu metallization all elements are equally distributed, which is characteristic for PVD sputter deposition processes. This can be seen in Fig. 2 at a depth of 30 nm and deeper. As soon as sample 1 was taken out of the vacuum chamber, aluminum, silicon and copper started to interact with
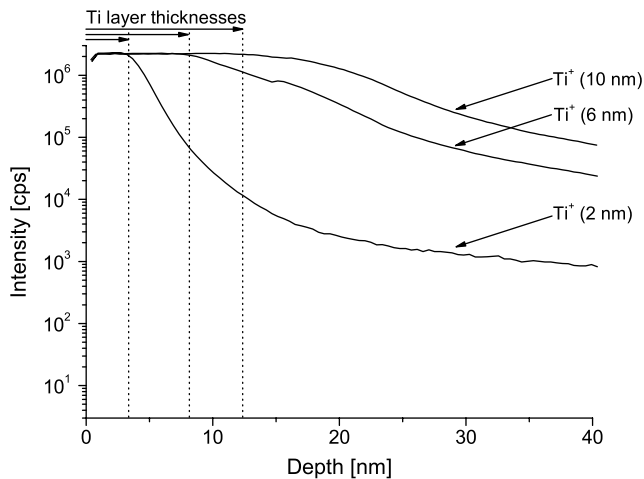
Figure 1. Depth profile of samples with 2, 6 and 10 nm Ti thickness measured in positive mode (500 eV O_2). Oxygen in cooperation leads to thicker Ti layers than deposited.
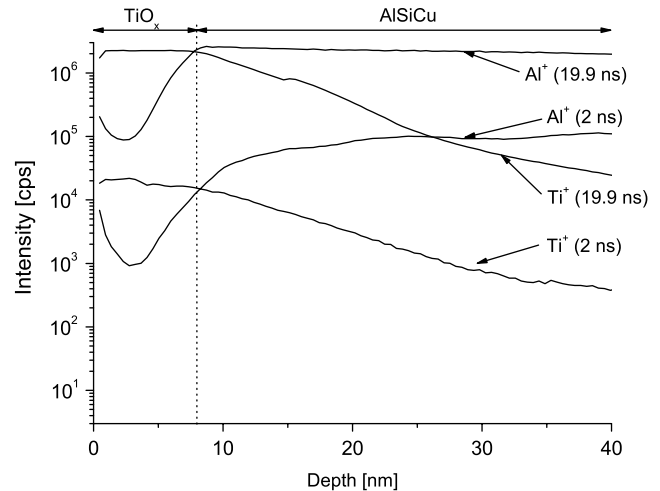
Figure 3. TOF-SIMS profile measured with different pulse widths.

Figure 2. TOF-SIMS depth profile of the AlSiCu metallization measured in negative mode (Cs 500 eV) provides composition information of the oxide and the metallization. It shows the effect of an air break on the sample surface and for Si^- and $^{63}Cu^-$ pile up effect at the oxide/metallization interface.

Table 2.	Chemical reactions and enthalpy at room temperature (RT)
Reaction	Standard enthalpy at RT [kJ/mol]
$Si + O_2 \rightarrow SiO_2$	−910.7
$4Al + 3O_2 \rightarrow 2\,Al_2O_3$	−1675.7
$2Cu + O_2 \rightarrow 2CuO$	−157.3
$Ti + O_2 \rightarrow TiO_2$	−1520.9

the ambient atmosphere, which leads to a change of the Al, Si, Cu distribution near the surface. During the self-passivation process, three different reactions compete with each other and try to build an oxide layer on the metallization (Table 2).

According to the values of the standard enthalpy (Table 2), the topmost layer is an almost pure aluminum oxide.[10] Silicon and copper do not contribute significantly to the surface oxide

formation, but they are concentrating at the metal–oxide interface during oxidation. Si and Cu accumulation at the interface Al_2O_3–AlSiCu can be explained by a pile-up effect owing to reduced solubility of Si and Cu in aluminum oxide. Moreover, the aluminum oxide prevents silicon and copper from diffusing to the surface.

Since aluminum has only one isotope, it is necessary to reduce the primary ion intensity in order to avoid detector overflow. Figure 3 shows the TOF-SIMS profiles of sample 5 in positive mode, and the effect of the reduction of the pulse width from 19.9 to 2 ns. The current of the analysis gun is lowered from 2.9 to 0.034 pA, with the result that less primary ions reach the sample surface per shot, and appropriately less secondary ions are generated. Detector overflow is avoided for the aluminum and titanium signals, therefore, the layer composition of the first few nanometer can be investigated without any information loss about the relative signal intensities. Signals of trace elements will perhaps be below the detection limit, e.g. in this case, the information for Cu^+ secondary ions is suppressed.

The aluminum oxide thickness of samples 2–7 is quasi-identical to the oxide thickness of sample 1. Hence, the air break in the experiment was sufficient to build up a complete aluminum oxide layer on top of the metallization.

Characterization of the effect of the air break on the titanium distribution

In order to investigate the effect of the air break on the titanium interaction with aluminum measurements of all samples have been done in positive and negative modes (Fig. 4(a) and (b)). In case of positive mode Al^+ and Ti^+ and for negative secondary ions AlO^- and TiO^- have been displayed. The maximum peak of the $Si^{+/-}$ signal has been used to valuate the measured crater depth.

As can clearly be seen at the samples without any air contact between Al and Ti deposition, the titanium starts to interact with the AlSiCu metallization and diffuses into layers underneath. Under ambient atmosphere, all four metals try to react with oxygen. According to the Richardson-Ellingham diagram and the standard enthalpy, the topmost layer is still made from aluminum oxide.[11]

The effect of an air break on silicon and copper has already been discussed above. Comparing the Ti^+ signals (Fig. 4(a)), only
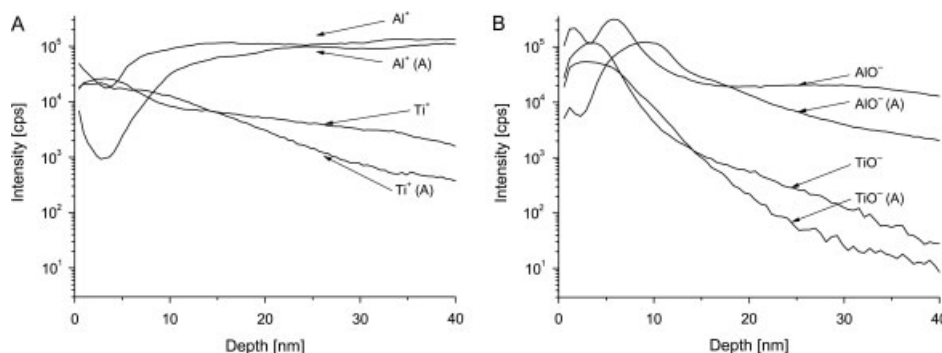
Figure 4. Depth profiles of samples with air break (A) and without air break measured in positive (Fig. 4(a)) and negative (Fig. 4(b)) modes. Aluminum oxide formation suppresses interaction of titanium and AlSiCu metallization.

the sample without air break shows a diffusion profile (shoulder in diagram). The grown aluminum oxide layer, acting as a diffusion barrier, prevents the titanium to interact with the Al metallization.

After sputter deposition, the titanium layer interacts with the oxygen first. Nevertheless, aluminum diffuses to the surface (Fig. 4(a) and (b)), which shows, that Ti has only poor barrier effect for Al.

Conclusion

We have shown the possibility of distinguishing between nanometer-scale titanium layers of different thicknesses on rough substrates by TOF-SIMS depth profiling with optimized parameter setting.

The self-passivation mechanism of aluminum at oxygen contact is shown, as well as the diffusion barrier effect of a native aluminum oxide layer. Breeded titanium contamination can only interact with an aluminum layer if contact to oxygen is strictly avoided. AFM measurements showed that neither an air break prior to titanium deposition nor additional roughening induced by the sputter beam during SIMS analysis have a significant influence on the surface roughness, and therefore, do not affect depth resolution.

References

[1] M. Petzold, L. Berthold, D. Katzer, H. Knoll, D. Memhard, P. Meier, K. D. Lang, *Microelectron. Reliab.* **2000**, *40*, 1515.
[2] P. G. D. Krueger, R. Krups, K. Pomplun, *Microelectron. Reliab.* **2000**, *40*, 6.
[3] C. Trouiller, T. Signamarcheix, M. Juhel, S. Petitdidier, H. Fontaine, M. Veillerot, L. F. T. Kwakman, C. Wyon, in *ToF-SIMS Applications in Microelectronics: Quantification of Organic Surface Contamination*, presented at Characterization and Metrology For Ulsi Technology **2005**, Richardson, Texas (USA), **2005**, 584.
[4] T. Fister, T. Schuerlein, in *ToF-SIMS: Surface Analysis by Mass Spectrometry;* (Eds: J. C. Vickerman, D. Briggs), IM Publications and SurfaceSpectra Limited, Chichester, West Sussex, U.K., **2001**, pp. 673–696.
[5] W. Vandervorst, *Appl. Surf. Sci.* **2008**, *255*, 805.
[6] E. Niehuis, T. Grehl, in Secondary Ion Mass Spectrometry, SIMS XII, Proceedings of the International Conference on Secondary Ion Mass Spectrometry, 12th, 2000, Brussels, Belgium, Sept. 5–10, **1999**, 49.
[7] S. Puchner, H. Hutter, C. Eisenmenger-Sittner, M. Kiniger, *Anal. Bioanal. Chem.* **2008**, *390*, 1537.
[8] T. Grehl, R. Möllers, E. Niehuis, *Appl. Surf. Sci.* **2003**, *203-204*, 277.
[9] E. Niehuis, Th. Grehl, in *ToF-SIMS: Surface Analysis by Mass Spectrometry,* (Eds: J. C. Vickerman, D. Briggs), IM Publications and SurfaceSpectra Limited, Chichester, West Sussex, U.K., **2001**, pp. 753–779.
[10] D.D. Wagman, in *CRC Handbook of Chemistry and Physics,* (75th edn), (Eds: R. L. David, H.P.R. Frederikse), CRC Press Inc., 2000 Corporate Blvd., N.W., Boca Raton, Florida 33431, **1995**, pp. 5–21.
[11] R. Bürgel, *Handbuch Hochtemperatur – Werkstofftechnik*, Vol. 3, Vieweg+Teubner: **2006**, pp. 248–254.

B.2 Publication 2

T. Aichinger, S. Puchner, M. Nelhiebel, T. Grasser, and H. Hutter

Impact of Hydrogen on Recoverable and Permanent Damage
following Negative Bias Temperature Stress

Impact of Hydrogen on Recoverable and Permanent Damage following Negative Bias Temperature Stress

T. Aichinger[1], S. Puchner[1], M. Nelhiebel[2], T. Grasser[3], and H. Hutter[4]

[1]Kompetenzzentrum für Automobil- und Industrieelektronik (KAI), Europastrasse 8, 9524 Villach, Austria
phone: 0043-4242-34890-24, email: thomas.aichinger@k-ai.at
[2]Infineon Technologies Austria, Siemensstrasse 2, 9500 Villach, Austria
[3]Christian Doppler Laboratory for TCAD, Institute for Microelectronics TU Wien, Gusshausstrasse 27-29, 1040 Wien, Austria
[4]Institute for Chemical Technologies and Analytics TU Wien, Getreidemarkt 9/E164, 1060 Wien, Austria

Abstract—**By subjecting selected split wafers to a specifically adapted measure-stress-measure (MSM) procedure, we analyze negative bias temperature stress (NBTS) and recovery characteristics of PMOS devices with respect to the impact of hydrogen. We control the hydrogen incorporation within the gate oxide during Back End of Line (BEOL) fabrication by varying the titanium barrier thickness below the routing metallization. Differences in the initial passivation degree of the gate oxide are verified electrically by Charge Pumping (CP) measurements and physically by time-of-flight secondary ion mass spectrometry (TOFSIMS). Our results indicate that the total V_{TH} shift is the sum of quasi permanent and recoverable damage which are of comparable scale but have completely different physical and electrical characteristics. While the permanent component seems to be strongly linked to hydrogen release from the interface (increase in CP current), the recoverable component is widely independent of hydrogen and its recovery can be controlled via carrier exchange with the silicon substrate. Hence, our results suggest different trap precursors for the individual components which challenge some predictions of the classical reaction-diffusion (RD) model and support the concepts of an alternative model based on permanent interface state creation via hydrogen transfer to recoverable E' centers which have their origin in oxygen vacancies, whose density is roughly independent of the hydrogen concentration.**

NBTI, hydrogen, Pb center, E' center, oxygen vacancy

I. INTRODUCTION

Hydrogen has often been reported to play a crucial role in the negative bias temperature instability (NBTI) of MOS devices [1-4]. This has been linked to its ability to passivate/de-passivate dangling bonds at the gate-oxide silicon-substrate interface [5]. In particular, the performance and defect densities of *virgin* silicon devices improve considerably by incorporating hydrogen into the gate oxide during the Back End of Line (BEOL) process [6]. This can be done either directly by exposing the wafers to pure hydrogen or forming gas anneals [7-8] or indirectly as a consequence of plasma-enhanced

chemical vapor deposition (PECVD) of silicon nitride (SNIT) layers [9]. Such layers are considered to be efficient hydrogen sources since they contain a large concentration of hydrogen [10-11] which may be released immediately after deposition to diffuse toward the gate oxide. Provided there is no diffusing barrier below the SNIT, some hydrogen may reach the gate oxide where it can passivate dangling bonds at the interface, thereby improving the virgin performance of the MOS device. However, once passivated, previously captured hydrogen may be released from the interface during NBTS leaving behind donor-like P_b centers that are reported to cause a negative shift in the threshold voltage of a p-doped metal oxide semiconductor (PMOS) transistor. Thus, one may expect that the initial passivation degree of the interface, namely the total number of Si-H bonds present at the interface before stress, crucially determines the NBTI sensitivity of the technology. This is a generally accepted fact often reported in literature. However, concerning the underlying micro-structural physics behind degradation and recovery, two competing models (namely the reaction diffusion (RD) model [2] and the alternative Grasser model [12]) come to different conclusions and hence make different predictions.

In order to check the fundamental statements of those models with respect to the impact of hydrogen, we have fabricated a wafer split, where we modified the hydrogen budget within the gate oxide (and hence the number of Si-H bonds at the interface). The hydrogen incorporation is measured physically by TOFSIMS analysis (counting secondary H ions) and electrically by CP measurements (counting dangling bonds at the interface). Having fabricated the hardware, we characterize and compare stress and recovery dynamics of two selected split wafers. Finally, we check our results against the predictions of the classical RD model [2] and against the alternative model introduced by Grasser et al. [12].

II. SAMPLE PREPARATION AND HARDWARE

Our basic idea for modifying the hydrogen content within the gate oxide is to control hydrogen diffusion from the upper SNIT layer toward the gate oxide. This is basically achieved by introducing titanium (Ti) liners below the routing metallization. Titanium is known to be an effective hydrogen barrier [13-15] which can absorb a certain amount of diffusing hydrogen.
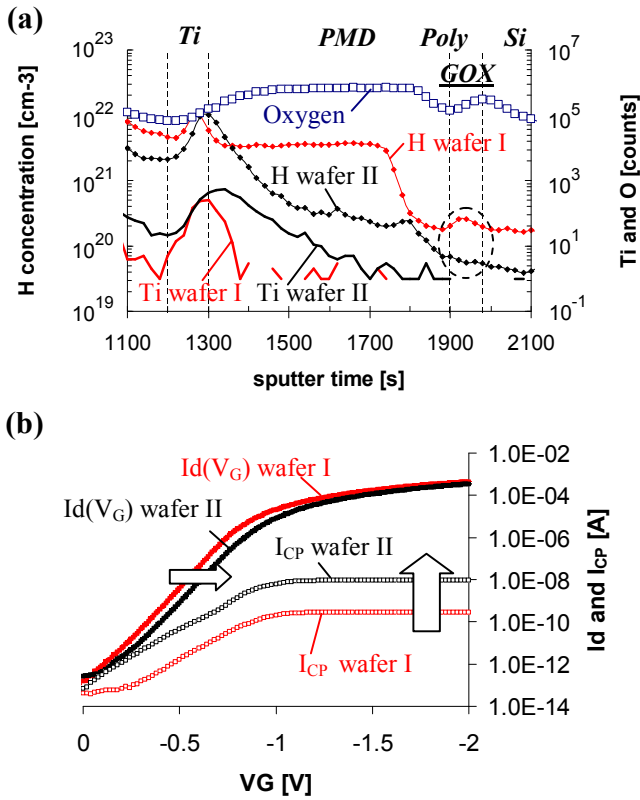
Figure 1. (a) TOFSIMS image of the BEOL process split wafers I and II. By modifying the titanium layer thickness, the hydrogen budget within the post metal dielectric (PMD), the gate-poly and within the gate oxide (GOX) can be controlled. Wafer I has a thinner Ti layer than wafer II and therefore more hydrogen within the GOX. (b) Virgin transfer curves (full squares) and CP currents (open squares) of the split wafers. Due to the higher hydrogen concentration within the GOX, wafer I has a more efficiently passivated interface, a lower CP signal and initially less positively charged defects than wafer II.

To produce split wafers with different hydrogen concentrations within the gate oxide, we simply vary the Ti liner thickness between the SNIT and the gate oxide. The thinner the titanium liner, the higher is its hydrogen permeability and the more hydrogen arrives actually at the gate oxide. In particular, as the titanium layer thickness exceeds several tens of nanometers, the hydrogen concentration within the gate oxide approaches a minimum which is reflected electrically by a maximum initial CP signal (low interface state passivation degree). In fact, the CP signal of such a sample is comparable to the one of a split wafer pulled before SNIT deposition indicating that hardly any hydrogen can pass a titanium barrier provided the barrier is sufficiently thick.

In our measurements discussed in the following, we focus on two representative split wafers (extreme cases), the first (wafer I) having a minimum titanium barrier (high hydrogen concentration in the gate oxide), the second (wafer II) having a very thick titanium barrier (minimum hydrogen concentration in the gate oxide). Except for the Ti-liner thickness, the two wafers were processed identically in the same wafer lot. Our devices under test (DUTs) are isolated PMOS transistors with 30 nm pure SiO_2 gate oxides. The structures are surrounded by

in-situ polyheaters that enable us to perform on-chip fast heating and cooling [16-17]. We use such thick oxide devices in order to improve the hydrogen resolution within the gate oxide during the TOFSIMS measurement and in order to reduce tunneling currents through the gate oxide during stress and during charge pumping. It has recently been shown that the basic mechanisms of NBTI are essentially the same in thin and thick SiO_2 and SiON technologies [18-20]. The use of pure SiO_2 gate oxides guarantees that our general conclusions are not distorted by the strongly process dependent impact of nitridation [21].

III. Hydrogen Detection using TOFSIMS

The hydrogen concentrations of the different split wafers were investigated by a time of flight secondary ion mass spectrometer (TOF.SIMS[5]) equipped with a liquid metal ion gun (LMIG) producing primary ions and a dual source (DSC-S) column eroding the sample surface. TOFSIMS measurements were performed on large reference capacitors (1 mm^2) located in the vicinity of the electrically measured PMOS devices. Depth profiling was carried out in the dual beam mode [22] using common techniques for insulators [23]. Pulsed Bi_1^+ primary ions (25 keV) were used to analyze the target surface. Alternating, a second beam of Cs^+ ions erodes the sample surface and enhances the yield of negatively charged secondary ions (e.g. H^-, O^-). In order to avoid distortion of the hydrogen signal, we abstained from exposing our samples to a chemical back preparation via etching. Hence, at the expense of depth resolution, we were forced to use a 2 keV sputter beam ablating the thick stack of layers (3.5 µm) on the top of the gate oxide within a reasonable time interval. To quantify the hydrogen signal, a relative sensitivity factor (RSF) was used for converting the secondary ion intensity into absolute concentrations. For determining this hydrogen-related RSF, we used reference samples providing a defined standard implantation dose ($\Phi_H = 10^{15}$ cm²). The obtained RSF for hydrogen was 5×10^{21}, which is close to literature values taking into account different matrix signals and SIMS techniques [24].

Fig. 1 (a) shows a TOFSIMS image of the sub-metal BEOL layer stack of the two selected split wafers. Displayed are the oxygen and the titanium signals for the orientation within the BEOL stack. Underneath the Ti liners we measure significantly different hydrogen concentrations in the PMD, the poly and the GOX for wafer I and II. In perfect agreement with the TOFSIMS results we obtain in Fig. 1 (b) that (i) the initial CP signal of wafer I (~ 0.3 nA) is about 30 times lower than the one of wafer II (~ 9 nA). This is consistent with the assumption that the interface of wafer I (Dit ~ 2.3×10^9 $eV^{-1}cm^{-2}$) is more efficiently passivated by hydrogen than the interface of wafer II (Dit ~ 6.9×10^{10} $eV^{-1}cm^{-2}$). The virgin CP currents were recorded at a temperature of 50°C using a pulsing frequency of 500 kHz and rising/falling slopes of 10 V/µs scanning roughly 500 meV of the silicon band gap around mid gap; (ii) wafer II has a more negative threshold voltage (~ -160 mV) than wafer I which can be explained by an initially larger number of positively charged P_b centers and oxide defects which both remain unpassivated in wafer II due to the low hydrogen concentration within the gate oxide.
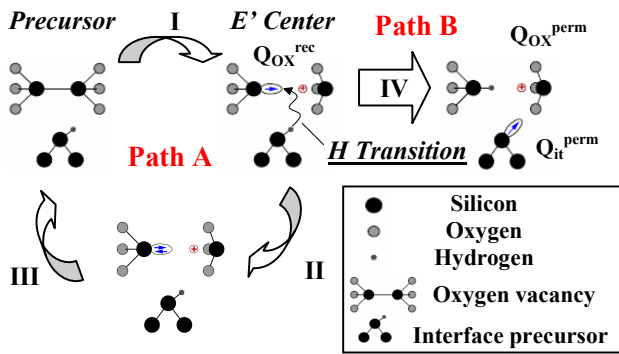
Figure 2. A schematic illustration of the Grasser model transitions. During stress, recoverable oxide traps are created by temperature and field induced bond breakage. In the positive charge state the E' center may become neutralized and anneals permanently (Path A) or gets locked-in by H capture form the interface (Path B).

IV. QUALITATIVE MODEL DISCRIPTIONS

Before starting with the description of the measurement setup and presenting results, we briefly summarize some of the main characteristics of the discussed NBTI models.

A. The RD model:

The classic reaction-diffusion (RD) model as described in [2] explains V_{TH} degradation and recovery by a non-dispersive diffusion process of neutral hydrogen atoms or molecules (H or H_2) which are released during stress from Si-H bonds at the interface via a field-dependent reaction. Once released, the hydrogen species diffuse away from the interface, leaving behind a positively charged interface state (Si^+) that is responsible for the higher threshold voltage and the lower transconductance. Once the stress is removed, previously released hydrogen can diffuse back and recombine with silicon dangling bonds restoring them to their passive Si-H state.

Consequences: (i) the increase in CP current fully explains the total V_{TH} shift; (ii) the recovery rate is proportional to the amount of created interface traps, released hydrogen respectively; (iii) recovery is not influenced by slight variations in gate biasing during read-out.

B. The Grasser model:

The chemical transitions suggested by the reaction controlled model of Grasser et al. [12] are schematically depicted in Fig. 2. **Path A:** During NBTS, oxygen vacancies located close to the interface are assumed to break up and charge positively (transition I) due to the presence of the high electric field and a majority of holes at the gate oxide substrate interface. During recovery, where the field and the carrier situation at the interface is quite different, some of these so-called E' centers (Q_{ox}^{rec}) may become neutralized by hole emission (transition II). Once in the neutral charge state, the E' center can anneal permanently via structural relaxation thereby restoring the initial precursor state again (transition III). **Path B:** Once created during stress, the dangling bond of the E' center can optionally attract a hydrogen atom from the interface which converts the recoverable oxide defect (Q_{ox}^{rec}) and the

passivated interface state (Si-H bonds) into a *locked-in* positive oxide defect (Q_{ox}^{perm}) and an electrically active P_b center (Q_{it}^{perm}) (transition IV). In principle, the reverse reaction of path B, where the H atom is released from the dangling bond of the E' center and travels back to the un-passivated interface state, is feasible as well. However, in a first order approximation, this back transition is neglected assuming that the Si-H bond is stable within the E' center. Consequently, once created, locked-in oxide defects and interface states are considered as permanent.

Consequences: (i) the total V_{TH} degradation consists of permanent interface states and locked-in oxide charges (which emerge in a physical 50:50 relation due to entropy driven hydrogen exchange between Si-H bonds at the interface and positively charged E' centers (cf. **Path B**)) plus a recoverable portion of positively charged E' centers; (ii) recovery (cf. **Path A**) is largely independent of the hydrogen incorporation (at least, when neglecting the loss of recoverable E' centers by transition IV); (iii) recovery (cf. **Path A**) is highly dependent on the gate bias during read-out since the carrier situation at the interface (and hence the Fermi-level position) governs neutralization and relaxation of positively charged E' centers.

V. ELECTRICAL MEASUREMENT SETUP

Our experimental setup for NBTI characterization is illustrated in Fig. 3. The measurement procedure is particularly designed to separate time and bias dependent recoverable damage from apparently permanent degradation. During a basic measure-stress-measure (MSM) cycle we subject PMOS devices to NBTS (200°C; < 7.0 MV/cm) for a defined time t_S. By making use of the in-situ polyheater technique, the following recovery phase can be performed at a much lower temperature of 50°C which decelerates thermo dynamical recovery mechanisms and improves the charge pumping measurement resolution. Right before the end of the stress phase, we quickly (< 10 s) cool down to 50°C while the stress bias is maintained at the gate, thereby quenching the degradation [16-17]. Then we initiate a 1000 s recovery phase (t_{R1}), by switching the gate bias from its stress level to -2.0 V.
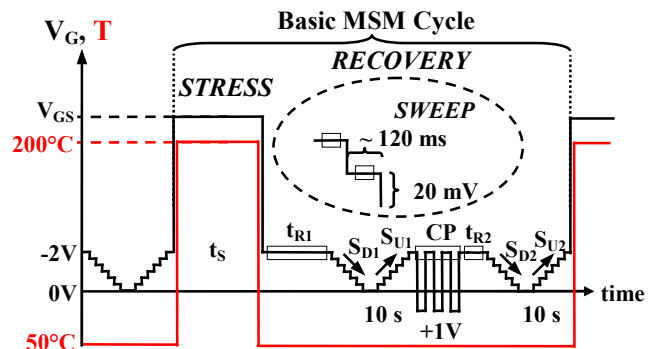
Figure 3. Our basic MSM procedure used for degradation/recovery analysis. During stress, we use the polyheater tool to generate an elevated stress temperature. During recovery, we perform gate bias sweeps and CP measurements in order to monitor V_{TH} recovery and interface state creation.

We denote the relative amount of V_{TH} recovery during t_{R1} between the first measured point after the removal of the stress bias (40 ms post stress) and the last measured point (1000 s post stress) as the *time dependent recovery* contribution (ΔV_{TH}^{time}). Subsequently to t_{R1}, we ramp down (SD1) the gate bias in 20 mV steps from strong inversion (-2.0 V) toward depletion (0.0 V) and monitor in parallel the V_{TH} shift as a function of the current gate bias. One full gate bias ramp takes approximately 10 s. Approaching depletion, the Fermi level moves from the valance band edge toward the conduction band edge thereby gradually changing the ratio of free holes and electrons at the interface. After staying for 10 s at 0.0 V, we ramp the gate bias back (SU1) to -2.0 V. The difference in the V_{TH} shift recorded at -2.0 V at the beginning of SD1 and at the end of SU1 is denoted as the *bias dependent recovery* contribution (ΔV_{TH}^{bias}). After the first ramp down-up cycle, we record the maximum CP current for 10 s by pulsing the gate junction between strong inversion (-2.0 V) and accumulation (+1.0 V) at a frequency of 500 kHz. In the analysis, we convert the maximum CP signal into an interface state dependent threshold voltage shift ($\Delta V_{TH}^{perm,it}$) by assuming an amphoteric nature of interface traps [25] and a flat density of state profile [26]. Subsequent to the CP cycle, we again perform a short 10 s constant gate bias phase at -2.0 V (t_{R2}) followed by a second down-up ramp (SD2; SU2). This basic MSM cycle is repeated six times on both devices of the wafer split with increasing stress times t_S (1/10/100/1,000/10,000/100,000 s).

VI. RESULTS AND DISCUSSION

The V_{TH} shifts measured during the different stages of the experiment (c.f. Fig. 3) are illustrated for wafer I (thin Ti/high H) in Fig. 4 (a) and for wafer II (thick Ti/low H) in Fig. 4 (b). Shown are six curves corresponding to the six subsequent stress-runs. In Fig. 4 (c), we have depicted separately the individual V_{TH} shifts for both devices as a function of the stress time. For both devices of the wafer split we obtain the following characteristics: (i) within the initial 1000 s constant bias phase in strong inversion (-2.0 V), we measure a similar amount of time dependent recovery (ΔV_{TH}^{time}) for both H-levels, cf. Fig. 4 (c1); (ii) the total V_{TH} shift decreases during SD1 and increases during SU1; (iii) a significant bias dependent reduction in the V_{TH} shift is observed after SU1 which is similar for both H-levels, cf. Fig. 4 (c2); (iv) after the intermediate CP cycle, the remaining degradation level is permanent and cannot be reduced further by an additional gate bias ramp toward 0.0 V; (v) The remaining permanent V_{TH} shift and the interface state dependent V_{TH} shift are much larger for wafer I than for wafer II, cf. Fig. 4 (c3); (vi) the interface state dependent V_{TH} shift is smaller than the permanent V_{TH} shift, cf. Fig. 4 (c3); (vii) interface state dependent and permanent V_{TH} shift coincide when multiplying $\Delta V_{TH}^{perm,it}$ by a factor 3, cf. Fig. 4 (c4).
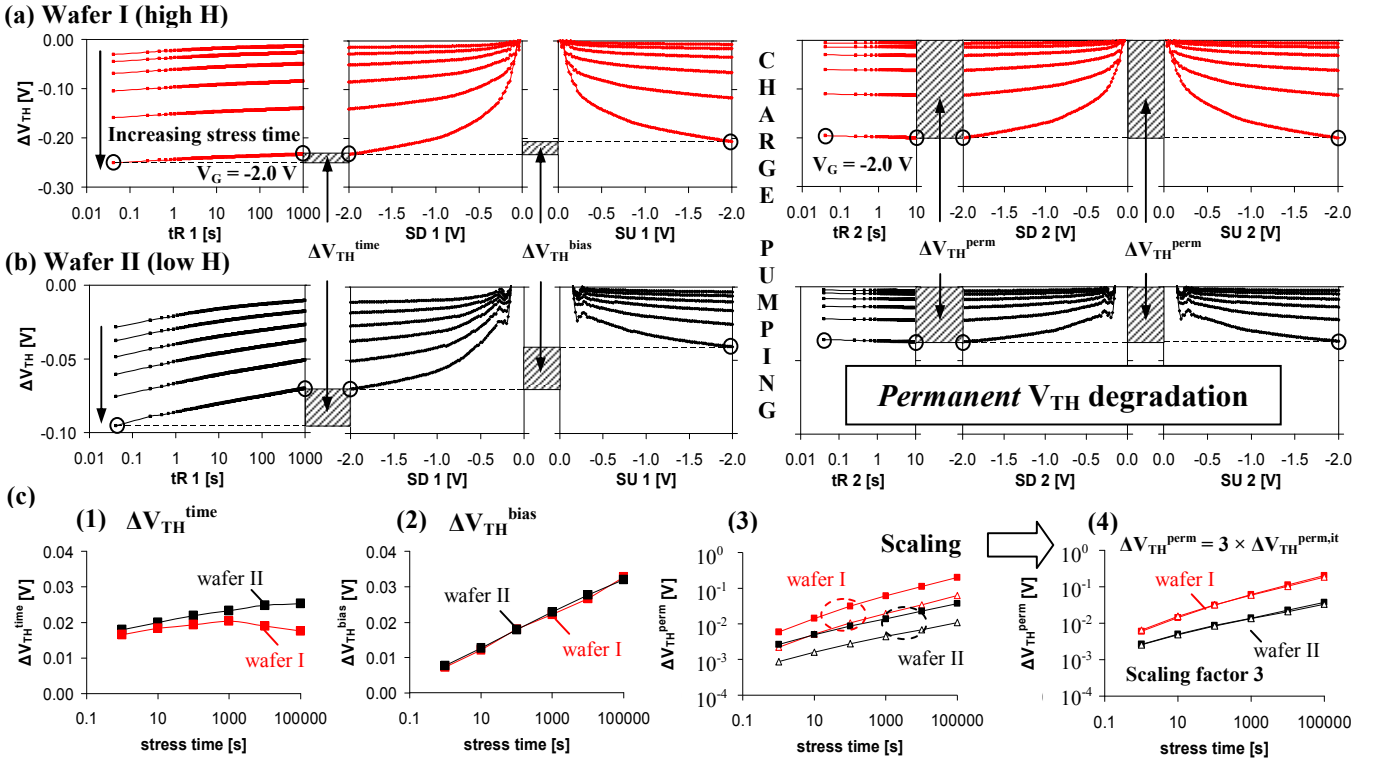
Figure 4. The V_{TH} shifts recorded after six subsequent stress-runs (1/10/100/1,000/10,000/100,000 s) at 50°C at different stages of the experiment (wafer I (a); wafer (II) (b)). The *time dependent V_{TH} recovery* (ΔV_{TH}^{time}) is recored at -2.0 V directly post stress for 1000 s (tR1). The *bias dependent recovery* (ΔV_{TH}^{bias}) is the difference in V_{TH} shift between SD1 and SU1 recorded at -2.0 V. Subsequently to SU1, we measure the maximum CP current and convert changes in I_{CP}^{max} into appropriate *interface state dependent V_{TH} shifts* ($\Delta V_{TH}^{perm,it}$). After gate pulsing, the remaining V_{TH} shift at -2.0 V is *permanent* (ΔV_{TH}^{perm}). In (c) the respective V_{TH} shifts are summarized for both wafers as a function of stress time: (c1) → ΔV_{TH}^{time}; (c2) → ΔV_{TH}^{bias}; (c3) → ΔV_{TH}^{perm} (full symbols) & $\Delta V_{TH}^{perm,it}$ (open symbols). By multiplying $\Delta V_{TH}^{perm,it}$ by a scaling factor 3, ΔV_{TH}^{perm} and $\Delta V_{TH}^{perm,it}$ coincide, cf. (c4).

These seven findings on the bias and time dependence of the recovery, on interface state creation and on permanent damage, as a function of the H content within the gate oxide, represent a significant collection of NBTI characteristics challenging the reliability of suggested models.

Cross check with the proposed NBTI models:

Point (i) – Recovery over time is H independent: Agrees only with the Grasser model which predicts that recovery (path A) is *nearly* independent of the hydrogen budget within the gate oxide except for the small fraction of recoverable damage being converted to locked-in oxide charge by hydrogen capture from the interface (path B), cf. Fig. 4 (c1). The RD model is challenged since it suggests a balance between hydrogen release and re-capture and would therefore predict a much larger amount of recovery for wafer I.

Point (ii) – V_{TH} shift is dependent on the applied gate bias: Agrees with both models which suggest that oxide traps and/or interface states may become neutralized and charge up positively again as the Fermi level crosses the silicon band gap [27-28].

Point (iii) – Ramping the gate toward 0.0 V accelerates V_{TH} recovery, the effect being H independent: Agrees only with the Grasser model which suggests bias dependent neutralization and relaxation of positively charged hydrogen-independent E' centers. The RD model cannot explain bias accelerated trap recovery since it assumes the hydrogen diffusion species to be neutral.

Point (iv) – The degradation level is quasi permanent after the intermediate CP cycle: In the Grasser model, this is explained by the bias-accelerated relaxation of E' centers which is finished after the first gate bias double ramp. The RD model would not expect significant recovery within the following 10-100 s either, since already more than 1000 s elapsed since the actual end of stress.

Point (v) – The remaining permanent V_{TH} shift is larger for the H rich wafer: Agrees with both models considering that the larger permanent damage of the H-rich wafer I is a logical consequence of its initially higher Si-H precursor concentration.

Point (vi): – $\Delta V_{TH}^{perm,it}$ is smaller than ΔV_{TH}^{perm}: Provided that our conversion of the CP signal into an interface state dependent V_{TH} shift ($\Delta V_{TH}^{perm,it}$) is correct, statement (vi) agrees only with the Grasser model which suggests that the permanent V_{TH} shift is the sum of locked-in oxide defects and interface states ($Q_{ox}^{perm} + Q_{it}^{perm}$). The RD model attributes the entire V_{TH} shift solely to interface states.

Point (vii) – $\Delta V_{TH}^{perm,it}$ is proportional to ΔV_{TH}^{perm}: Agrees with the Grasser model which predicts the simultaneous creation of $\Delta V_{TH}^{perm,it}$ and ΔV_{TH}^{perm} via hydrogen exchange between passivated interface states and E' centers and hence suggests a physical 50:50 relation and a strong correlation between $\Delta V_{TH}^{perm,it}$ and ΔV_{TH}^{perm}. The deviation in the measured factor 3 from the proposed factor 2 (50:50) may be due to different energy distributions of interface and oxide charges, leading to a different electrical response of both trap types. It has to be remarked that basically the profiled energy range during CP and the energy range of defects being positively charged during the drain current measurement do not coincide. We have considered this energy mismatch assuming an amphoteric nature of interface traps [25] and a flat density of state profile [26].

Discussion on the absolute degradation potential

Fig. 5 illustrates the development of the absolute CP current (a) and the effective difference in the absolute V_{TH} between wafer I and II (b). Before stress (stress time = 0 s) wafer II has a considerable higher CP signal and also a much lower V_{TH} than wafer I. Note that this initial difference in the CP current (~ 92 nA) accounts only for ~ 53 mV of the difference in the initial V_{TH} (~ 160 mV) which reflects even on the virgin device the factor 3 measured between interface state creation and V_{TH} shift. The mismatch is increasingly compensated with increasing stress time. Indeed, after 100,000 s of stress, both devices have a similar CP signal and almost the same V_{TH}. However, since neither the CP signal nor the V_{TH} development of wafer I tends to saturate, it is likely to assume that wafer I would even have exceeded wafer II in the CP current and in the V_{TH} at longer stress times. Following Ref. [6], this would indicate that the sum of Si-H bonds plus interface traps (Si•) is initially higher in a thoroughly passivated gate oxide, implying an additional latent damage by excessive hydrogen ingress. This may lead eventually to a higher absolute drift potential for the H-rich wafer I at longer stress times. Additional measurements are required in order to verify this suggestion unambiguously.
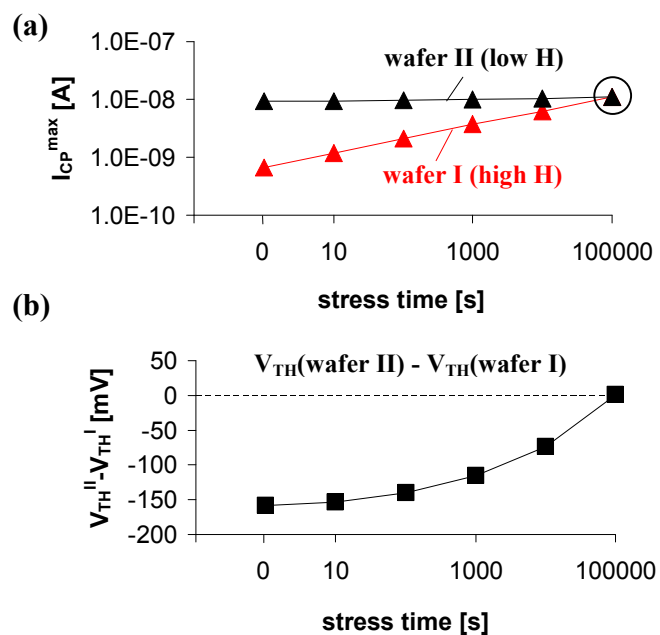
Figure 5. Development of the maximum CP current as a function of the stress time for wafer I and II (a). After 100,000 s of stress, the maximum CP signal of wafer I equals the maximal CP signal of wafer II indicating a similar number of interface traps at the end of the last stress run. Also, the initial difference in V_{TH} between wafer I and II is compensated at the end of the last stress run (b) indicating a similar degradation level of the oxide and the interface.

VII. Conclusions

By varying the Ti thickness during BEOL processing, we have produced two split wafers with vastly different hydrogen contents within the gate oxide and subjected them to NBTS. In agreement with the Grasser model, we have demonstrated that the recoverable part of the NBT degradation is largely independent of hydrogen while the permanent V_{TH} shift component is strongly linked to the total hydrogen budget within the gate oxide. Also, a strong correlation between the increase in the CP signal and the permanent V_{TH} shift component was found which is also consistent with the Grasser model.

References

[1] K. O. Jeppson, and C. M. Svensson, "Negative bias stress of MOS devices at high electric fields and degradation of MNOS devices," J. Appl. Phys.,Vol. 48, Issue 5, pp. 2004-2014, 1977.

[2] M. A. Alam , and S. Mahapatra, "A comprehensive model of PMOS NBTI degradation," Microelectron. Reliab., Vol. 45, Issue 1, pp. 71-81, 2005.

[3] A. T. Krishnan, S. Chakravarthi, P. Nicollian, V. Reddy, and S. Krishnan, "Negative bias temperature instability mechanism: The role of molecular hydrogen," Appl. Phys. Lett., Vol. 88, Issue 15, pp. 153518 1-3, 2006.

[4] T. Grasser, B. Kaczer, and W. Goes, "An energy-level perspective of negative bias temperature instability," In Proc. 46th Annual International International Reliability Physics Symposium (IRPS), pp. 28-38, 2008.

[5] E. Cartier, J. H. Stathis, and D. A. Buchanan, "Passivation and depassivation of silicon dangling bonds at the Si/SiO_2 interface by atomic hydrogen," Appl. Phys. Lett., Vol. 63, Issue 11, pp. 1510-1512, 1993.

[6] M. Nelhiebel, J. Wissenwasser, Th. Detzel, A. Timmerer, and E. Bertagnolli, "Hydrogen-related influence of the metallization stack on characteristics and reliability of a trench gate oxide," Microelectron. Reliab., Vol. 45, Issue 9-11, pp. 1355-1359, 2005.

[7] Y. Nissan-Cohen, "The effect of hydrogen on hot carrier and radiation immuity of MOS devices," Appl. Surf. Sci., Vol. 39, Issue 1-4, pp.511-522, 1989.

[8] L. J. Jin, H. P. Kuan, D. Sim, and M. Mukhopadhyay, "Influence of hydrogen annealing on NBTI performance," In Proc. 15th IEEE International Symposium on the Physical and Failure Analysis of Integrated Cicuits (IPFA), pp. 1-4, 2008.

[9] J. Z. Xie, and S. P. Murarka, "Stability of hydrogen in silicon nitride films deposited by low-pressure and plasma enhanced chemical vapor deposition techniques," J. Vac. Sci. Technol. B, Vol. 7, Issue 2, pp. 150-152, 1989.

[10] C. Y. Chang, and S. M. Sze, "ULSI Technology," McGraw-Hill, Chapt. 5.6.3, Table 5, 1996.

[11] I. Jonak-Auer, R. Meisels, and F. Kuchar, "Determination of the hydrogen concentration of silicon nitride layers by Fourier transform infrared spectroscopy," Infrared Phys. Technol., Vol. 38, Issue 4, pp. 223-226, 1997.

[12] T. Grasser, B. Kaczer, W. Goes, Th. Aichinger, Ph. Hehenberger, and M. Nelhiebel, "A two-stage model for negative bias temperature instability," In Proc. 47th Annual International International Reliability Physics Symposium (IRPS), pp. 33-44, 2009.

[13] T. Pompl, K.-H. Allers, R. Schwab, K. Hofmann, and M. Roehner, "Change of acceleration behavior of time-dependent dielectric breakdown by the BEOL process: indicators for hydrogen induced transition in dominat degradation mechanism," In Proc. 43th Annual International International Reliability Physics Symposium (IRPS), pp. 388-397, 2005.

[14] A. D. Marwick, J. C. Liu, and K. P. Rodbell, "Hydrogen redistribution and gettering in AICu/Ti thin films," J. Appl. Phys.,Vol. 69, Issue 11, pp. 7921-7923, 1991.

[15] D. E. Woon, and D. S. Marynick, "Titanium and Copper in Si: barriers for diffusion and interactions with hydrogen," Phys. Rev. B: Condens. Matter, Vol. 45, Issue 23, pp. 13383-13389, 1992.

[16] T. Aichinger, M. Nelhiebel, S. Einspieler, and T. Grasser, "In-Situ Polyheater – A reliable tool for performing fast and defined temperature switches on chip," IEEE Trans. Device Mater. Reliab., 2009, in press.

[17] T. Aichinger, M. Nelhiebel, and T. Grasser, "On the temperature dependence of NBTI recovery," Microelectron. Reliab., Vol. 48, Issue 8-9, pp. 1178-1184, 2008.

[18] G. Pobegen, T. Aichinger, M. Nelhiebel, T. Grasser, "The Influence of the gate oxide thickness on negative bias temperature instability", In Proc. 48th Annual International International Reliability Physics Symposium (IRPS), 2010, in press.

[19] T. Grasser, B. Kaczer, T. Aichinger, W. Gös, and M. Nelhiebel, "Defect Creation Stimulated by Thermally Activated Hole Trapping as the Driving Force Behind Negative Bias Temperature Instability in SiO_2, SiON, and High-k Gate Stacks," In Proc. IEEE International Integrated Reliablity Workshop (IIRW), pp. 91-95, 2008.

[20] H. Reisinger, R. Vollertsen, P.-J. Wagner, T. Huttner, A. Martin, S. Aresu, W. Gustin, T. Grasser, and C. Schlünder, "The Effect of Recovery on NBTI Characterization of Thick Non-Nitrided Oxides," In Proc. IEEE International Integrated Reliablity Workshop (IIRW), pp. 1-6, 2008.

[21] S. Mahapatra, K. Ahmed, D. Varghese, A. E. Islam, G. Gupta, L. Madhav, D. Saha, and M. A. Alam, "On the Physical Mechanism of NBTI in Silicon Oxynitride p-MOSFETs: Can Differences in Insulator Processing Conditions Resolve the Interface Trap Generation versus Hole Trapping Controversy?," In Proc. 45th Annual International International Reliability Physics Symposium (IRPS), pp. 1-9, 2007.

[22] E. Niehuis, and T. Grehl, "Secondary Ion Mass Spectrometry," In Proc. 12th International Conference on Secondary Ion Mass Spectrometry (SIMS XII), pp. 49-54, 2000.

[23] B. Hagenhoff, D. Van Leyen, E. Niehuis, and A. Benninghoven, "Time-of-flight secondary ion mass spectrometry of insulators with pulsed charge compensation by low-energy electrons," J. Vac. Sci. Technol., A: Vacuum, Surfaces, and Films, Vol. 7, Issue 5, pp. 3056-3064, 1989.

[24] R.G. Wilson, "SIMS quantification in Si, GaAs, and diamond - an update," Int. J. Mass Spectrom. Ion Processes, Vol. 143, pp. 43-49, 1995

[25] P. V. Gray, and D. M. Brown, "Density of $Si-SiO_2$ interface states," Appl. Phys. Lett., Vol. 8, Issue 2, pp. 31-33, 1966.

[26] G. Groeseneken, H. E. Maes, N. Beltran, and R. F. De Keersmaecker, "A reliable approach to charge-pumping measurements in MOS transistors," IEEE Trans. Electron Devices, Vol. 31, No. 1, pp. 42-53, 1984.

[27] V. Huard, M. Denais, and C. Parthasarathy, "NBTI degradation: From physical mechanisms to modelling," Microelectron. Reliab., Vol. 46, Issue 1, pp. 1-23, 2006.

[28] D. S. Ang, S. Wang, G. A. Du, and Y. Z. Hu, "A consistent deep-level hole trapping model for negative bias temperature instability," IEEE Trans. Device Mater. Reliab., Vol. 8, No. 1, pp. 22-34, 2008.

C

Acronyms

RBS	Rutherford Backscattering
ERD	Elastic Recoil Detection
SEM	Scanning Electron Microscope / Electron microscopy
AES	Auger − Electron − Spectrometry
AFM	Atomic Force Microscopy
ToF−SIMS	Time−of−Flight Secondary−Ion−Mass−Spectrometry
BEOL	Back End Of Line
GOX	gate oxide
MOS	Metal−Oxide−Semiconductor
MOS−FeT	MetalOxideSemiconductor Field−effect Transistor
c.w.	compare with
SIMS	Secondary−Ion−Mass−Spectrometry
ToF	Time−of−Flight
PID	primary ion dose

PIDD   primary ion dose density

LMIG   Liquid Metal Ion Gun

DHM   digital holography microscope

RSF   Relative sensitivity factors

VLSI   Very$-$large$-$scale integration

SNIT   silicon nitride layer

GC$-$MS   Gas chromatography$-$ mass spectrometry

UHV   ultra$-$high vacuum

PVD   physical vapor deposition

HCBU   high current bunched mode

CAD   computer$-$aided design

LDV   laser doppler vibrometer

NBTI   negative bias temperature instability

CP   charge pumping

VT_H permanent treshold voltage shift

PECVD   plasma$-$enhanced chemical vapor deposition

ERDA   Elastic Recoil Detection Analysis

FZ   foat$-$zone

SRP   Spreading Resistance Profiling

SRIM   Stopping and Range of Ions in Matter

EM   Electron Microscopy

LM   Light Microscopy

D
Symbols

L_d	drift section length
E_{kin}	kinetic energy
m	mass
v	velocity
e	elementary charge, electric charge carried by a single proton
U_a	potential energy of a given electrostatic field
T	travel time
Δm	mass difference
$\frac{m}{\Delta m}$	mass resolution
$\frac{t}{\Delta t}$	time resolution
ΔE	energy error
σ	surface area which is on average affected by a primary ion
A	totally bombarded area (area of interest of an primary ion beam)
$I_{S(A)}$	Secondary ion intensity of the measured isotope of the element A [ions / s]

I_P	Primary ion intensity [ions / s]
S	Sputter yield [atoms / primary ion]
$\alpha_A^\pm$	Positive respectively negative ionization probability of the sputtered atoms
$i_{S(A)}$	Isotope frequency of the measured isotope of the element A
η_A	Efficiency of the secondary ion measurement (output of the ion extraction, transmission of the mass spectrometer, efficiency of the detector)
c_A	atom concentration of the element A in the sample
$\rho_{A/B}$	Relative sensitivity factor
S	Sputter yield [atoms / primary ion]
$\alpha_A^\pm, \alpha_B^\pm$	Positive respectively negative ionization probability of the sputtered atoms of the element A respectively B
$i_{S(A)}, i_{S(B)}$	Isotope frequency of the measured isotope of the element A respectively elements B
η_A, η_B	Efficiency of the secondary ion measurement (output of the ion extraction, transmission of the mass spectrometer, efficiency of the detector) for the element A respectively B.
$I_{S(A)}, I_{S(B)}$	Secondary ion intensity of the measured isotope of the element A respectively B [ions / s]
c_A, c_B	Atom concentration of the element A respectively B in the sample
z	Number of cycles
$I_{S(A)(i)}, I_{S(B)(i)}$	Secondary ion intensity of the measured isotope of the element A respectively B at cycle i [ions / s]
d	Depth [cm]
Q_d	Implantation doses [$atoms/cm^2$]
R_q	root mean squared
R_a	arithmetic average of the absolute values
y_i	vertical distance from the mean line at the ith data point

F	shear force
a	acceleration of the device // displacement
a_{max}	peak acceleration
f	frequency
ϑ_{max}	vibration velocity
ε	strain distribution
U_0	displacement amplitude
λ	wave length
ω	angular frequency
ϑ	peak velocity at the end of the holder
$RSF_{H,M}$	Relative sensitivity factor for an element H in a matrix M
J_H	atom concentration of the element H in the sample
d	Depth [cm]
I_M	Secondary ion intensity of the measured isotope of the matrix M [ions / s]
I_H	Secondary ion intensity of the measured isotope of the element H [ions / s]
I_{bg}	background noise level of the element H in the matrix M [ions / s]

References

[1] Wikipedia moore's law.

[2] W. H. BRATTAIN G. L. PEARSON. History of semiconductor research. *Proc. of the IRE*, 1955.

[3] Krames M.R. Dupuis, R.D. History, development, and applications of high-brightness visible light-emitting diodes. *Journal of Lightwave Technology*, 26(9):1154–1171, 2008. cited By (since 1996) 33.

[4] Xie W.-P.b Zhou L.-J.b Chen L.b Wang X.-X.a Yuan, J.-Q.a b. Developments and applications of photoconductive semiconductor switches in pulsed power technology. *Qiangjiguang Yu Lizishu/High Power Laser and Particle Beams*, 20(1):171–176, 2008. cited By (since 1996) 10.

[5] Wikipedia http://en.wikipedia.org/wiki/transistor.

[6] Stuart Macdonald Ernest Braun. *Revolution in miniature: the history and impact of semiconductor electronics.* Cambridge University Press, 1982.

[7] Robert W. Price. *Roadmap to entrepreneurial success: powerful strategies for building a high-profit business.* AMACOM, American Management Association, 2004.

[8] Gordon E. Moore. Cramming more components onto integrated circuits. *Electronics*, 38(8), 1965.

[9] W.F. Brinkman, D.E. Haggan, and W.W. Troutman. A history of the invention of the transistor and where it will lead us. *Solid-State Circuits, IEEE Journal of*, 32(12):1858 –1865, December 1997.

[10] Roland Mller-Fiedler and Volker Knoblauch. Reliability aspects of microsensors and micromechatronic actuators for automotive applications. *Microelectronics Reliability*, 43(7):1085 – 1097, 2003.

[11] L. Kotz-G. Tlg L. Fabry, S. Pahlke. Trace-analytical methods for monitoring contaminations in semiconductor-grade si manufacturing. *FRESENIUS' JOURNAL OF ANALYTICAL CHEMISTRY*, 349(4):260–271, 1994.

[12] Jae Cheol Lee, Jeongyeon Won, Youngsu Chung, Hyungik Lee, Eunha Lee, Donghun Kang, Changjung Kim, Jinhak Choi, and Jeomsik Kim. Investigations of semiconductor devices using sims; diffusion, contamination, process control. *Applied Surface Science*, 255(4):1395 – 1399, 2008. Proceedings of the Sixteenth International Conference on Secondary Ion Mass Spectrometry, SIMS XVI.

[13] R. F. K. Herzog and F. P. Viehböck. Ion source for mass spectrography. *Phys. Rev.*, 76(6):855–856, Sep 1949.

[14] H.W. Werner A. Benninghoven, F. G. Rdenauer. *Secondary Ion Mass Spectrometry: Basic Concepts, Instrumental Aspects, Applications and Trends*, volume 86. A Wiley-Interscience Publication by John Wiley & Sons, Inc., 1987.

[15] Bruno W. Schueler. *Time-of-Flight Mass Analysers*. IM Publications and Surface-Spectra Limited, 2001.

[16] ION-TOF GmbH, Mnster, Germany. *TOF SIMS HTML Help*, 4.1.0.1 edition, 1996-2004.

[17] http://mass-spec.lsu.edu/msterms/index.php/resolution_(mass_spectrometry).

[18] B. Hagenhoff, D. van Leyen, E. Niehuis, and A. Benninghoven. Time-of-flight secondary ion mass spectrometry of insulators with pulsed charge compensation by low-energy electrons. *Journal of Vacuum Science & Technology A: Vacuum, Surfaces, and Films*, 7(5):3056–3064, 1989.

[19] Birgit Hagenhoff. High resolution surface analysis by tof-sims. *Microchimica Acta*, 132(2):259–271, April 2000.

[20] Roman Markus Hefele. Spectral characterisation of different glycerophospholipids using time-of-flight secondary ion mass spectrometry and matrix-assisted laser desorption/ ionisation time-of-flight mass spectrometry. Master's thesis, University of Technology Vienna, 2010.

[21] Herbert Hutter Markus Holzweber, Ernst Pittenauer. Investigation of ionic liquids under bi-ion and bi-cluster ions bombardment by tof-sims. *Journal of Mass Spectrometry*, in press.

[22] Herbert Hutter Markus Holzweber. Investigation of 1-butyl-3-methylimidazolium bis(trifluoromethylsulfonyl)imide under binx+ cluster ion bombardment. *Surface and Interface Analysis*, 42:1025–1029, 2010.

[23] Farida Benabdellah & Alexandre Seyer & Loc Quinton & David Touboul & Alain Brunelle & Olivier Laprvote. Mass spectrometry imaging of rat brain sections: nanomolar sensitivity with maldi versus nanometer resolution by tofsims. *Anal Bioanal Chem*, 396:151162, 2010.

[24] H.-N. Migeon A. Benninghoven, P. Bertrand and H.W. Werner, editors. *Dual Beam SIMS Depth Profiling*, volume 12 of *International Conference on Secondary Ion Mass Spectrometry*. Elsevier Science B.V., 2000.

[25] Rowland Hill. *Primary Ion Beam Systems*. IM Publications and SurfaceSpectra Limited, 2001.

[26] Herbert Hutter Christoph J. Straif. Investigation of polymer thin films by use of bi-cluster-ion-supported time of flight secondary ion mass spectrometry. *Anal Bioanal Chem*, 393:18891898, 2009.

[27] Dragan Krecar. *Applications of High Performance Physical Analytics in Materials Science*. PhD thesis, TU Vienna, 2005.

[28] D. Gui, Z.X. Xing, Y.H. Huang, Z.Q. Mo, Y.N. Hua, S.P. Zhao, and L.Z. Cha. Long-term reproducibility of relative sensitivity factors obtained with cameca wf. *Applied Surface Science*, 255(4):1427 – 1429, 2008. Proceedings of the Sixteenth International Conference on Secondary Ion Mass Spectrometry, SIMS XVI.

[29] Milton Ohring. *Reliability and Failure of Electronic Materials and Devices*. ACADEMIC PRESS LIMITED, 1998. chapter: Defects, Contaminants and Yield.

[30] S. Puchner, A. Zechmann, Th. Detzel, and Hutter H. Titanium layers on aluminium bond pads: Characterisation of thin layers on rough substrates. *Surface and Interface Analysis*, 2010.

[31] T. Francis. *Semiconductor International*. 1993.

[32] Thomas Schuerlein Thomas Fister and Patricia Lindley. *Contamination Monitoring and Failure Analysis*. IM Publications and SurfaceSpectra Limited, 2001.

[33] N. Tuccitto, V. Torrisi, I. Delfanti, and A. Licciardello. Monoatomic and cluster beam effect on tof-sims spectra of self-assembled monolayers on gold. *Applied Surface Science*, 255(4):874 – 876, 2008. Proceedings of the Sixteenth International Conference on Secondary Ion Mass Spectrometry, SIMS XVI.

[34] http://de.wikipedia.org/wiki/titanocen.

[35] D. Katzer H. Knoll D. Memhard P. Meier K. D. Lang M. Petzold, L. Berthold. Surface oxide films on aluminum bondpads: Influence on thermosonic wire bonding behavior and hardness. *Microelectronics Reliability*, 40:1515–1520, 2000.

[36] D. Kruger, J. Dabrowski, P. Gaworzewski, R. Kurps, and K. Pomplun. Fluorine incorporation into gate stacks of advanced silicon memory technologies: Simulation, depth distribution, and reliability. *Journal of Applied Physics*, 90(7):3578–3584, 2001.

[37] T. P. Ma. Metal–oxide–semiconductor gate oxide reliability and the role of fluorine. volume 10, pages 705–712. AVS, 1992.

[38] R. Williams and M. H. Woods. Mobile fluoride ions in sio[sub 2]. *Journal of Applied Physics*, 46(2):695–698, 1975.

[39] David Briggs. *Surface Characterisation of Polymers*. IM Publications and Surface-Spectra Limited, 2001.

[40] David Briggs. *Interpretation of Spectra*. IM Publications and SurfaceSpectra Limited, 2001.

[41] Christoph Josef Straif. *The interaction of Bi cluster ions with molecular compounds Towards a new generation of organic time of fight secondary ion mass spectrometry*. PhD thesis, TU Wien, 2009.

[42] K. Thomas E. Herr A. Hamidi, N. Beck. Reliability and lifetime evaluation of different wire bonding technologies for high power igbt modules. *Microelectronics Reliability*, 39:1153–1158, 1999.

[43] Kiat Choon Teo Sung Yi, Sang Kyoo Park. A study of aluminium wire failure in automotive under-hood applications. *Microelectronics International*, 23:11 – 20, 2006.

[44] Cemal Basaran Hua Ye, Minghui Lin. Failure modes and fem analysis of power electronic packaging. *Finite Elements in Analysis and Design*, 38:601–612, 2002.

[45] M. Legros Ph. Dupuy C. Levade D. Martineau, T. Mazeaud. Characterization of alterations on power mosfet devices under extreme electro-thermal fatigue. *Microelectronics Reliability*, 2010.

[46] A. Zegadi Ly. Benbahouche, A. Merabet. An improved understanding of igbt behavior under thermal stress. *Proc. 26th International Conference of Microelectronics Miel*, 2008.

[47] S. Lefebvre Z. Khatir. Boundary element analysis of thermal fatigue effects on high power igbt modules. *Microelectronics Reliability*, 44:929938, 2004.

[48] Wuchen Wu, M. Held, P. Jacob, P. Scacco, and A. Birolini. Investigation on the long term reliability of power igbt modules. pages 443 –448, may. 1995.

[49] M. Petzold, L. Berthold, D. Katzer, H. Knoll, D. Memhard, P. Meier, and K. D. Lang. Surface oxide films on aluminum bondpads: Influence on thermosonic wire bonding behavior and hardness. *Microelectronics Reliability*, 40(8-10):1515 – 1520, 2000. Reliability of Electron Devices, Failure Physics and Analysis.

[50] A. Cartwright T. Dishongh Y. Zhao, C. Basaran. Thermomechanical behavior of micron scale solder joints under dynamic loads. *Mechanics of Materials*, 32:161–173, 2000.

[51] Douglas C. Hopkins Hua Ye, Cemal Basaran. Damage mechanics of microelectronics solder joints under high current densities. *International Journal of Solids and Structures*, 40:40214032, 2003.

[52] P. COVA1 M. PASQUALETTI M. PORTESINE P. E. ZANI A. PIRONDI, G. NICO-LETTO. Thermo-mechanical simulation of a multichip press-packed igbt. *Solid-State Electronics*, 42:2303–2307, 1998.

[53] G. Khatibi, W. Wroczewski, B. Weiss, and H. Ipser. A novel accelerated test technique for assessment of mechanical reliability of solder interconnects. *Microelectronics Reliability*, 49(9-11):1283 – 1287, 2009. 20th European Symposium on the Reliability of Electron Devices, Failure Physics and Analysis, 20th European Symposium on the Reliability of Electron Devices, Failure Physics and Analysis.

[54] G. Khatibi, W. Wroczewski, B. Weiss, and T. Licht. A fast mechanical test technique for life time estimation of micro-joints. *Microelectronics Reliability*, 48(11-12):1822 – 1830, 2008.

[55] T. Grehl, R. Mllers, and E. Niehuis. Low energy dual beam depth profiling: influence of sputter and analysis beam parameters on profile performance using tof-sims. *Applied Surface Science*, 203-204:277 – 280, 2003.

[56] Stefan Puchner, Herbert Hutter, Christoph Eisenmenger-Sittner, and M. Kiniger. Tof-sims investigations on thermally treated coppermolybdenum films on a carbon substrate. *Analytical and Bioanalytical Chemistry*, 390(6):1537–1541, March 2008.

[57] D.D. Wagman. *CRC Handbook of Chemistry and Physics*. CRC Press Inc., 2000 Corporate Blvd., N.W., Boca Raton, Florida 33431, 75 edition, 1995.

[58] R. Buergel. *Handbuch Hochtemperatur-Werkstofftechnik*, volume 3. Vieweg+Teubner, 2006.

[59] E. Napolitani, D. De Salvador, M. Pesce, A. Carnera, S. Mirabella, and F. Priolo. Room temperature migration of boron in crystalline silicon during secondary ion mass spectrometry profiling. volume 24, pages 394–398. AVS, 2006.

[60] T. Detzel M. Nelhiebel H. Hutter S. Krivec, M. Buchmayr. Voltage assisted sodium ion incorporation and transport in thin silicon dioxide films. *Surface and Interface Analysis*, 2010.

[61] Michael Buchmayr Herbert Hutter Stefan Krivec, Thomas Detzel. On the temperature dependence of na migration in thin sio2 films during tof-sims o2+ depth profiling. *Applied Surface Science*, 257:25–32, 2010.

[62] Leiliang Zheng, Andreas Wucher, and Nicholas Winograd. Fundamental studies of molecular depth profiling and 3d imaging using langmuir-blodgett films as a model.

Applied Surface Science, 255(4):816 – 818, 2008. Proceedings of the Sixteenth International Conference on Secondary Ion Mass Spectrometry, SIMS XVI.

[63] K-H. Klsener J. Hartung, B. Elpelt. *Statistik Lehr- und Handbuch der angewandten Statistik*. R. Oldenbourg Verlag Muenchen Wien, 1991.

[64] Zdravko Siketic, Iva Bogdanovic Radovic, and Milko Jaksic. Quantitative analysis of hydrogen in thin films using time-of-flight elastic recoil detection analysis. *Thin Solid Films*, 518(10):2617 – 2622, 2010.

[65] Uwe Reinholz, Wolfram Bremser, Klaus-Werner Brzezinka, Erik Strub, Hans-Peter Weise, and Silke Merchel. A thin-layer reference material for hydrogen analysis. *Nuclear Instruments and Methods in Physics Research Section B: Beam Interactions with Materials and Atoms*, 266(10):2418 – 2423, 2008. Accelerators in Applied Research and Technology - Proceedings of the 9th European Conference on Accelerators in Applied Research and Technology, 9th European Conference on Accelerators in Applied Research and Technology.

[66] Anand T. Krishnan, Srinivasan Chakravarthi, Paul Nicollian, Vijay Reddy, and Srikanth Krishnan. Negative bias temperature instability mechanism: The role of molecular hydrogen. *Applied Physics Letters*, 88(15):153518, 2006.

[67] Kjell O. Jeppson and Christer M. Svensson. Negative bias stress of mos devices at high electric fields and degradation of mnos devices. *Journal of Applied Physics*, 48(5):2004–2014, 1977.

[68] Thomas Aichinger, Michael Nelhiebel, Stefan Decker, and Tibor Grasser. Energetic distribution of oxide traps created under negative bias temperature stress and their relation to hydrogen. *Applied Physics Letters*, 96(13):133511, 2010.

[69] T. Aichinger, S. Puchner, M. Nelhiebel, T. Grasser, and H. Hutter. Impact of hydrogen on recoverable and permanent damage following negative bias temperature stress. *in press*, 2010.

[70] Yoav Nissan-Cohen. The effect of hydrogen on hot carrier radiation immunity of mos devices. *Applied Surface Science*, 39(1-4):511 – 522, 1989.

[71] I. Jonak-Auer, R. Meisels, and F. Kuchar. Determination of the hydrogen concentration of silicon nitride layers by fourier transform infrared spectroscopy. *Infrared Physics & Technology*, 38(4):223 – 226, 1997.

[72] M. Riedel and H. Dsterhft. Hydrogen outgassing of zrnicu(h) amorphous alloy studied by secondary ion mass spectrometry. *Rapid Commun. Mass Spectrom.*, 12(20):1510–1514, 1998.

[73] H. Kauppinen, C. Corbel, K. Skog, K. Saarinen, T. Laine, P. Hautojärvi, P. Desgardin, and E. Ntsoenzok. Divacancy and resistivity profiles in n-type si implanted with 1.15-mev protons. *Phys. Rev. B*, 55(15):9598–9608, Apr 1997.

[74] J. F. Ziegler. www.srim.org, 2010.

[75] R. G. Wilson and S. W. Novak. Systematics of secondary-ion-mass spectrometry relative sensitivity factors versus electron affinity and ionization potential for a variety of matrices determined from implanted standards of more than 70 elements. *Journal of Applied Physics*, 69(1):466–474, 1991.

[76] R. G. Wilson, G. E. Lux, and C. L. Kirschbaum. Depth profiling and secondary ion mass spectrometry relative sensitivity factors and systematics for polymers/organics. *Journal of Applied Physics*, 73(5):2524–2529, 1993.

[77] R. G. Wilson. Sims quantification in si, gaas, and diamond - an update. *International Journal of Mass Spectrometry and Ion Processes*, 143:43 – 49, 1995.

[78] Th. Aichinger. *On the role of Hydrogen in Silicon device degradation and metalization processing*. PhD thesis, TU Vienna, 2010.

[79] D. E. Woon and D. S. Marynick. Titanium and copper in si: barriers for diffusion and interactions with hydrogen. *Phys. Rev. B: Condens. Matter*, 45(23):13383–13389, 1992.

[80] L.J. Jin, H.P. Kuan, D. Sim, and M. Mukhopadhyay. Influence of hydrogen annealing on nbti performance. In *Physical and Failure Analysis of Integrated Circuits, 2008. IPFA 2008. 15th International Symposium on the*, pages 1 –4, 2008.

[81] Joseph Z. Xie, Shyam P. Murarka, Xin S. Guo, and William A. Lanford. Stability of hydrogen in silicon nitride films deposited by low-pressure and plasma enhanced chemical vapor deposition techniques. *Journal of Vacuum Science Technology B: Microelectronics and Nanometer Structures*, 7(2):150 –152, March 1989.

[82] A. D. Marwick, Joyce C. Liu, and K. P. Rodbell. Hydrogen redistribution and gettering in alcu/ti thin films. *Journal of Applied Physics*, 69(11):7921–7923, 1991.

List of Figures

List of Tables

CV - DI Stefan Puchner

Personal Data

Date of Birth	17.08.1982
Place of Birth	St. Poelten
Nationality	Austria
Family Status	Unmarried, no children
Address	Vorgartenstraße 221/6/35, 1020 Wien, Austria
e-mail	stefan.puchner @gmail.com

Job History

Mai 2007 – Sept. 2010	KAI - Kompetenzzentrum für Automobil- und Industrieelektronik GmbH

Academic Career

Mai 2007 – now	Doctoral Studies at the Institute for Chemical Technologies and Analytics, Vienna University of Technology
Oct. 2000 – June 2007	Studies Technical Physics at Vienna University of Technology. Topic of the Master Thesis: „Thin layer surface analysis with ToF-SIMS" under the guidance of Univ.-Prof. Dr. Herbert Hutter at the Institute for Chemical Technologies and Analytics
Wintersemester 2004/05	ETH Zuerich (project: "chemical shift imaging" on the institute for biomedical research)

Education

June 2000	School Leaving Examination
1993 – 2000	High School: BG/BRG St. Pölten
	(1995-2000: focus on Natural Science) Josefstrasse 84, A-3100 St. Pölten
1988 - 1992	Elementary School Neulengbach

Further Activities

Summer 2003	Siemens (traineeship: compartment for quality assurance)
Summer 2002	Hoerbiger Ventilwerke GmbH, Vienna (traineeship: technical support)
2001 – 2007	Tennis instructor
	Associate Lecturer Pädagogische Akademie des Bundes Wien (College of Education, Vienna)
	Organization und Supervision of several Tennis camps for children
2004 – 2007	Associate Skiing – Instructor Secondary School Neulengbach

Special Knowledge and Interests

Hobbies	Travelling, Reading
Sport	Tennis (certified instructor), Skiing, Beachvolleyball,
Foreign Languages	English (fluent)
Drivers License	A, B,
Software	MS Office-Package, Adobe Creative Suite, Corel Draw, Sigma Plot, OriginPro, SciFinder, LaTeX, LINUX, Basics in Programming

List of Publications

Papers

T. Aichinger, S. Puchner, M. Nelhiebel, T. Grasser, and H. Hutter
"Impact of Hydrogen on Recoverable and Permanent Damage following
Negative Bias Temperature Stress" Reliability Physics Symposium (IRPS),
2010 IEEE International, pp. 1063 – 1068

**Christoph Henkel, Ole Bethge, Stephan Abermann, Stefan Puchner,
Herbert Hutter and Emmerich Bertagnolli**
"Pt-assisted oxidation of (100)-Ge/high-k interfaces and improvement of their
electrical quality", Appl. Phys. Lett. 97, 152904 (2010)

**Christoph Henkel, Stephan Abermann, Ole Bethge, Gianmauro Pozzovivo,
Stefan Puchner, Herbert Hutter and Emmerich Bertagnolli**
"Reduction of the PtGe/Ge Electron Schottky-Barrier Height by Rapid Thermal
Diffusion of Phosphorous Dopants"
J. of the Electrochem. Soc., 157 2010, accepted

S. Puchner, A. Zechmann, Th. Detzel and H. Hutter
"Titanium layers on aluminum bond pads:
Characterisation of thin layers on rough substrates"
Surf. Interface Anal. (2010)

**Stefan Puchner & Herbert Hutter, Christoph Eisenmenger-Sittner, M.
Kiniger**
"TOF-SIMS investigations on thermally treated copper–molybdenum films
on a carbon substrate"
Anal. Bioanal. Chem. (2008) 390: 1537–1541

**M. Kiniger, C. Eisenmenger-Sittner, J. Hell, B. Schwarz, H. Hutter and S.
Puchner**
"Carbide formation upon heat treatment of molybdenum layers deposited on
carbon substrates: comparison of experimental data with a cellular automaton
model"
Surf. Interface Anal. 2008; 40: 786–789

Oral Presentations & Posters

<u>Stefan Puchner</u>, Arno Zechmann, Thomas Detzel, Herbert Hutter
"Titanium layers on aluminium bond pads: Characterisation of thin layers on rough substrates"
European Conference for Applied Surface and Interface Analysis (ECASIA) – 2009, Antalya